ABSTRACT

Linking Onshore and Offshore Data to Find Seismogenic Faults
Along the Eastern Malibu Coastline

Mark A. Millard, M.S.

Committee Chairperson: Vincent S. Cronin, Ph.D.

The Santa Monica Mountains form part of the structurally active southern edge of the Transverse Ranges Province. The purpose of this research is to identify and characterize potentially seismogenic faults in onshore and offshore portions of the Topanga 7.5' Quadrangle using near-shore geophysical data, multibeam data, digital elevation models, earthquake focal mechanism solutions, and field work.

Several faults, many of which are previously-unmapped, have been identified in the study area, and determined to be potentially seismogenic. Results show that active seismogenic faulting in the Santa Monica Mountains is not restricted to the Malibu Coast Fault Zone as previously hypothesized. The sub-bottom acoustic survey provides evidence for the continuity of the Potrero Canyon and Santa Monica Faults in the near-shore portion of the Santa Monica Bay. Seismo-lineaments projected into the Santa Monica Bay indicate that one or more faults identified in the offshore portion of the study area may be seismogenic.

Linking Onshore and Offshore Data to Find Seismogenic Faults
Along the Eastern Malibu Coastline

by

Mark A. Millard, B.S.

A Thesis

Approved by the Department of Geology

____
Steven G. Driese, Ph.D., Chairperson

Submitted to the Graduate Faculty of
Baylor University in Partial Fulfillment of the
Requirements for the Degree
of
Master of Science

Approved by the Thesis Committee

____
Vincent S. Cronin, Ph.D., Chairperson

____
Steve I. Dworkin, Ph.D.

____
Phillip Johnson, Ph.D.

Accepted by the Graduate School
August 2007

____
J. Larry Lyon, Ph.D., Dean

Page bearing signatures is kept on file in the Graduate School.

TABLE OF CONTENTS

LIST OF FIGURES

LIST OF TABLES

ACKNOWLEDGMENTS

This study was sponsored by the American Association of Petroleum Geologists, Sigma Xi, and the Baylor University Department of Geology. I want to thank Dr. Vincent S. Cronin for guiding me through this research, and sharing his extensive knowledge of science and life in general. I appreciate the help of Dr. Johnson and Dr. Dworkin for volunteering their time to review the results of this thesis. I would also like to acknowledge Dr. Mark Swanson and Dr. Matthew Bampton at the University of Southern Maine and Mark Lovell, Dr. Dan Moore, Dr. Bill Little, Dr. Roger Hoggan, and Dr. Rob Clayton at Brigham Young University-Idaho for initially sparking my interest in Geology. I would also like to thank my parents for always teaching me through the years the importance of higher education. Finally, I want to thank my wife, Erica Millard, for not only enduring field work while pregnant with our first child, but also giving me support and encouragement on a daily basis that I hold so dear.

CHAPTER ONE

Introduction

Earthquakes and landslides are common natural occurrences in southern California. Protection from such disasters requires special regulations regarding zoning and building codes. The primary statutory mechanism through which Californians are protected from earthquake fault-rupture hazards is the Alquist Priolo Act (Hart, 1994). In order for a fault to be considered “active” under the Alquist-Priolo act, it must be demonstrated, through a trench study, that it cuts Holocene sediment (Hart, 1994). However, trench studies are expensive, require special permits, must be conducted by geologists who are licensed by the State of California, and require undeveloped land.

The Malibu Coast Fault Zone (MCFZ), which extends along the southern margin of the Santa Monica Mountains, defines the southern edge of the western Transverse Ranges Province (Cronin and Sverdrup, 1998; figure 1). Two small strands of the MCFZ, termed the Solstice and Winter Mesa Strands, are considered the only active faults in the Santa Monica Mountains (Bayliss and Cronin, 2005; figure 2). However, focal mechanism solutions from recent earthquakes that have occurred in the area suggest these are not the only strands that generate earthquakes. The identification of active faults is difficult in areas such as the Santa Monica Mountains because of extensive vegetation, urbanization, high-relief, and limited or restricted access. Many of the faults in the Santa Monica Mountains are located in areas where Holocene sediment is not present, making the criteria for determination of an “active” fault inapplicable.

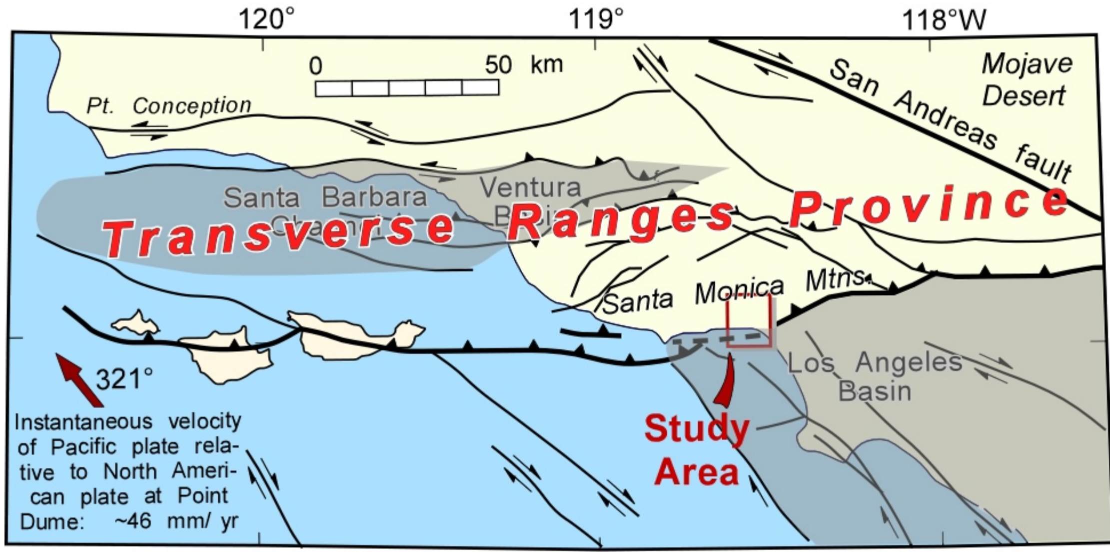

FIGURE 1.—The study area is located along the southern edge of the Santa Monica Mountains which marks the southern boundary of the Transverse Ranges Province. Modified from Bayliss (2006).

FIGURE 2.—The Malibu Coast Fault Zone extends along the southern edge of the central Santa Monica Mountains. Faults in the figure include the the Solstice strand (S) and the Winter Mesa strand (WM) of the Malibu Coast Fault Zone (outlined in red), and the Potrero Canyon Fault (P). Figure from Bayliss (2006).

Aerial photo interpretation has been widely used by geologists to identify and characterize surface traces of faults and landslides (Hobbs, 1904; Miller, 1961; Ray, 1960). Satellite imagery is useful in fault studies due to the possibility of visualization of certain phenomena related to tectonic activity such as gas seeps and lineation of vegetation (Cronin and others, 1993; Lillesand and Kiefer, 1987). Digital Elevation Models (DEMs) are also useful for fault studies because they depict a bare image of the Earth's surface, without the distractions typical of aerial photography. DEMs can be artificially illuminated any direction selected by the user, which facilitates the identification of geomorphic lineaments related to faults (Cronin and others, 2003; Haugerud and others, 2003). Lineaments detected in aerial photography, satellite imagery, and DEMs may be related to a variety of natural and anthropogenic causes. The genetic origin of a given lineament must be evaluated through field work.

Cronin developed a code in *Mathematica* (2004) that projects a fault-plane solution from a published focal mechanism solution to a surface represented by a DEM. The intersection of the fault-plane solution and the ground surface is referred to as a *seismo-lineament*. Through this method specific earthquake events can be spatially (and perhaps genetically) linked to faults on the surface, suggesting that the fault may be potentially *seismogenic* (i.e., capable of producing earthquakes).

The objective of this study is to locate and characterize potentially seismogenic faults in the onshore and offshore portions of the Topanga 7.5' Quadrangle using DEMs, seismo-lineaments from earthquake focal mechanism solutions, near-shore geophysical data, and field work.

The study area is located in the Topanga 7.5 Minute Quadrangle of southern California, which includes part of the central Santa Monica Mountains, northeastern Santa Monica Bay, and a small portion of northwestern Los Angeles Basin. The study was conducted in both the onshore and offshore portions of the quadrangle.

CHAPTER TWO

Background

Tectonic and Stratigraphic Setting

The Santa Monica Mountains and adjacent Los Angeles Basin are located on the Pacific Plate west of the San Andreas Transform Zone, which forms an important part of the present boundary between the North American and Pacific plates. The Pacific plate is currently moving ~47 mm/yr relative to the North American plate toward an azimuth of ~321° as computed for Point Dume, just west of the study area (Cronin and Sverdrup, 1998). Tsutsumi and others (2001) suggest that transpressional crustal deformation across the Transverse Ranges is likely related to the movement of the range along the southern restraining bend of the San Andreas Fault.

Paleomagnetic data show that the Transverse Ranges are rotating clockwise at a rate of ~6° per million years. The present orientation of the range is the result of ~16-18 million years of rotation for a total of ~96° rotation (Lajoie and others, 1979; Kamerling and Luyendyk, 1979; Luyendyk and others, 1985; Luyendyk, 1991; Hornafius and others, 1986). Legg and and others (2004) suggest that rotation is the result of basal traction as the Transverse Ranges are thrust over the California Continental Borderland. This model is supported by results from the Los Angeles Area Seismic Experiment II (LARSE II) which showed that the Santa Monica Mountains thrust over the Continental Borderland (Fuis and others, 2001).

During a Middle Miocene episode of block faulting and rotation, the southern edge of the Santa Monica Mountains was subjected to major faulting. Movement associated with this episode was primarily left-lateral (Yeats, 1968). However, in the Late Miocene, the Santa Monica Mountains also underwent significant uplift during opening of the Los Angeles basin, evidenced by folds in the footwall of the Santa Monica Fault that formed during faulting (Wright, 1991). Current shortening beneath the northern Los Angeles Basin is occurring at a rate of ~4-10 mm per year, expressed as compression of the Transverse Ranges along the Santa Monica, Dume, and Malibu Coast faults, and along a north-dipping blind thrust beneath the Los Angeles basin (Davis and others, 1989; Lajoie and others, 1979; Kamerling and Luyendyk, 1979; Luyendyk and others, 1985; Luyendyk, 1991).

The Stratigraphy of the Santa Monica Mountains and adjacent Los Angeles Basin has been described in detail by Durham and Yerkes (1963), Hoots (1931), Schoellhamer and others (1981), Woodring and others (1946), Yerkes and others (1965), Yerkes (1972), and Yerkes and Campbell (1979). Sedimentary rocks present in the Santa Monica Mountains are Jurassic to Pleistocene in age (Blake, 1991). A majority of the faults identified in this study are in marine and nonmarine sandstones and conglomerates of the upper Cretaceous Tuna Canyon, lower Paleocene and Eocene Coal Canyon, upper Eocene, Oligocene, and lower Miocene Sespe, and middle Miocene Topanga Canyon Formations (Yerkes and others, 1994).

Previously Mapped Faults in the Study Area

Faults in the study area are part of a regional fault system that marks the tectonic boundary between the California Continental Borderland to the southwest, the Peninsular

Ranges Province to the southeast, and the western Transverse Ranges to the north (Wright, 1991). Published geological maps of the study area have been produced by Hoots (1931), Yerkes and Wentworth (1965), Campbell and others (1966), Yerkes and others (1971), McGill (1981, 1982, 1989), Crook and Proctor (1992), Dibblee (1992) and Yerkes and Campbell (1980, 1997). The geology of the Santa Monica Bay has been mapped by Dartnell and others (2004), Greene & Kennedy (1986), Junger and Wagner (1997), and Lee and others (1979).

Major faults in the study area include the main strand and Las Flores strand of the Malibu Coast Fault, the Potrero Canyon Fault, the offshore Santa Monica Fault, and several unnamed offshore faults interpreted from marine geophysical data; all of which are part of a system of north-dipping, left-oblique faults referred to as the Malibu Coast Fault Zone (MCFZ) (Cronin and Sverdrup, 1998; figures 3 and 4). West of the study area, the Solstice and Winter Mesa Strands of the Malibu Coast Fault are the only faults along the western Santa Monica Mountains classified as "active" under California's Alquist-Priolo Act (Cronin and Sverdrup, 1998).

East of the study area, the Malibu Coast Fault Zone merges with the Potrero Canyon, Santa Monica, Cucamonga, Hollywood, and Raymond Faults. West of the study area the Malibu Coast Fault Zone merges with the active offshore Santa Cruz Island and Santa Rosa Island faults (Cronin and Sverdrup, 1998). Evidence of Holocene activity along the MCFZ has been compiled by Treiman (1994, 2000). Although only two segments of the MCFZ are officially recognized as being active, Dolan and others (1995) suggest that the MCFZ is capable of producing earthquakes as large as M 7.0.

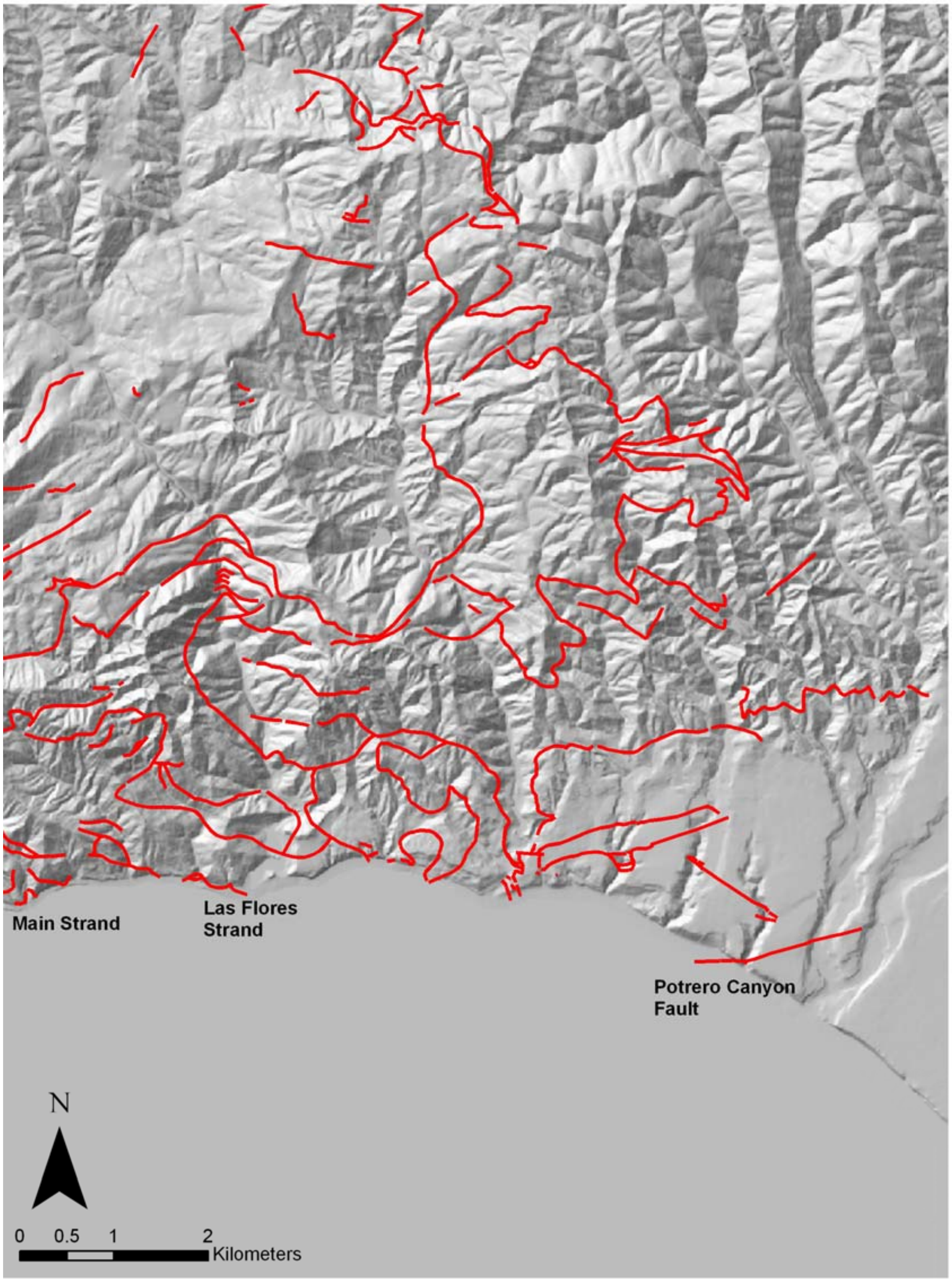

FIGURE 3.—Previously published faults in the Topanga 7.5’ Quadrangle by Yerkes and Campbell (1997). Labeled faults in the map are the major faults of the MCFZ in the Topanga 7.5’ Quadrangle.

The Potrero Canyon Fault is exposed at the mouth of Potrero Canyon, approximately 0.7 miles northeast of Santa Monica along the Pacific Coast Highway (McGill, 1989). The fault originally appeared as an unnamed fault on the geologic map of H.W. Hoots (1930). It was later called the Potrero Fault by H.R. Johnson (1932) and the Potrero Canyon Fault by Moran and others (1959). It has been described as active/potentially active by Cronin and Sverdrup (1998). The original outcrop of the fault was studied by Johnson (1932) before being destroyed by urban development. The fault has indirectly been studied using other methods by Dibblee (1992), Hill (1979), Mcgill, (1981), (1982), (1989), McGill and others (1987), and Wright (1991).

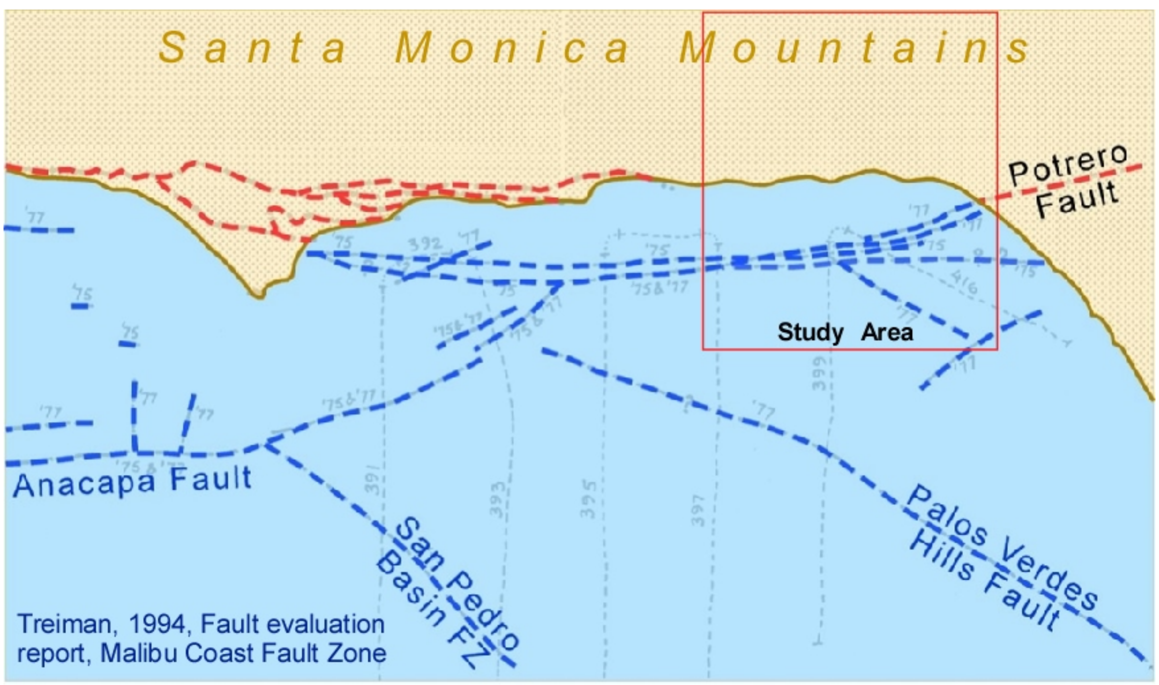

FIGURE 4 .—Map showing interpreted faults along the shoreline and in the Santa Monica Bay. Modified from Treiman (1994).

McGill (1980) and Campbell (1990) suggest that the Potrero Canyon fault is likely an onshore extension of the Malibu Coast Fault Zone. However, Treiman (1994) suggests that offshore data to prove this connection are lacking. According to Dolan and Sieh (1992) the Potrero Canyon Fault is probably a north branch of the Santa Monica Fault Zone as originally inferred by Junger and Wagner (1977).

Multiple sources, such as the National Geophysical Center, maintain catalogs with an excess of 1000 historic earthquakes in the Santa Monica Mountains, suggesting that the area is seismically active (figure 5). Focal mechanism solutions derived from numerous earthquakes show that seismic activity is not entirely concentrated along the MCFZ.

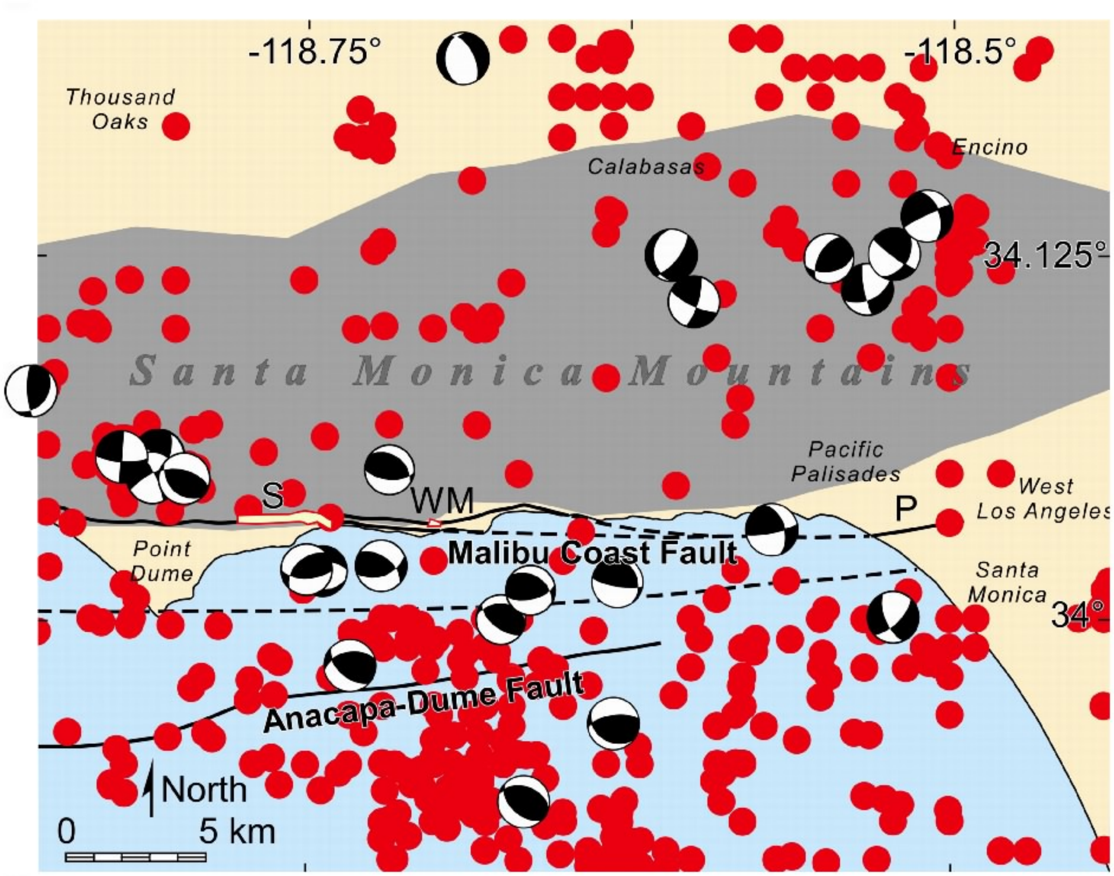

FIGURE 5.—Map showing earthquakes that have occurred in the Santa Monica Mountains. The epicenters (red dots) and focal mechanism solutions depicted in this map are from Cronin and Sverdrup (1998), Hauksson (2000, 2004), and Hardebeck (2005). The yellow-filled red polygons are the Solstice Strand (S) and the Winter Mesa Strand (WM), and the fault is the fault P is the Potrero Canyon Fault.

Legal Definition of an Active Fault

Following the 1971 magnitude 6.6 San Fernando Earthquake, the Alquist-Priolo Earthquake Fault Zoning Act was developed as part of California's Public Resources Code, sections 2621-2630 (Hart, 1994). The purpose of the act was to limit possible property damage and loss of life due to earthquakes by prohibiting "the location of most structures for human occupancy across the traces of active faults" (Hart, 1994). According to the Alquist-Priolo Act, a fault is defined as "a fracture or zone of closely associated fractures along which rocks on one side have been displaced with respect to those on the other side…A fault is distinguished from those fractures or shears caused by landsliding or other gravity-induced surficial features" (Hart, 1994). According to the Alquist-Priolo Act, it is prohibited to place a structure within 50 ft (~15 m) of the trace of an active fault (Hart, 1994).

In order to define a fault as "active" and establish an earthquake fault zone, a certified geologist must demonstrate that the fault fulfills two criteria. The criteria as described by Hart (1994) are:

1. A fault must be "sufficiently active." A fault is deemed sufficiently active if there is evidence of Holocene surface displacement along one or more of its segments or branches. Holocene displacement may be directly observable or inferred; it need not be present everywhere along a fault to qualify that fault for zoning.

2. A fault must be "well-defined." A fault is considered well-defined if its trace is clearly detectable by a trained geologist as a physical feature at or just below the ground surface. The fault may be identified by direct observation or by indirect methods. The critical consideration is that the fault, or some of it, can be located in the field with sufficient precision and confidence to indicate that the required site-specific investigations would meet with some success.

Previous Studies on Lineament Detection

Extensive research in recent years has been conducted using lineament detection in DEMs and other remotely sensed images. Jordan and others (2005) derived algorithms and filters that can be applied to DEMs to automatically extract drainage patterns, lineaments, and other useful information. Madani (2001) analyzed the selection of optimum Landsat Thematic Mapper bands for automatic lineament extraction in Egypt. Won-In and Charusiri (2003) investigated the enhancement of thematic mapper images for lineament detection and geologic mapping in Vietnam.

Lineament analysis of remotely sensed images has been used extensively to characterize faults and fractures. Fu and others (2004) used ASTER 3D images to map an active fault associated with the 2004 Mw 6.6 Bam earthquake in southeast Iran. Akman and Tufekci (2004) explored the used of hillshades coupled with other remotely sensed data to characterize faults and geomorphologic features in Turkey. McMahon and North (1993) described a technique for making measurements on faults by combining DEMs and subsurface data. Another method by Beaver and others (1987) involved analysis of structural features in DEMs in order to determine the regional stress domain of a given area. This method is useful in areas that have experienced few tectonic events; however, it is not useful in areas with complex tectonic histories.

Recently, artificially illuminated hillshades derived from DEMs have been used to identify and characterize lineaments. Cronin and others (1993, 2003) conducted geomorphic analyses using hillshades to identify lineaments that may be associated with active or previously unmapped structures in the northern Himalaya and Santa Monica Mountains. Bayliss and Cronin (2005) tested a method which involves the use of DEMs coupled with focal mechanism solutions to identify potentially active faults. Lidmar-Bergstrom and others (1991) suggest that shading from certain azimuths results in a biased analysis because some lineaments become more or less visible based on the azimuth. Smith and Clark (2005) refer to this as "azimuth-biasing." Onorati and others (1992) found through comparison of lineaments depicted on hillshades to geologic maps that illumination from multiple azimuths results in improved identification of lineaments. Wise and others (1985) suggest that lineaments are most visible when illuminated at a right angle to the trend.

CHAPTER THREE

Methods

Overview

Traditional geomorphic analysis of remotely sensed data coupled with seismo-lineament analysis was used to identify potentially seismogenic faults in the Topanga 7.5' Quadrangle of the Santa Monica Mountains. Published focal mechanism solutions from earthquakes that occurred in the region were projected to the surface of a DEM with a grid spacing (i.e., horizontal resolution) of 10 m, creating a seismo-lineament swath. A geomorphic lineament analysis was performed using artificial illumination of DEMs to accentuate geomorphic lineaments in the seismo-lineament regions that could likely be related to faulting. The seismo-lineament and geomorphic lineament analysis produced maps of possible seismogenic fault trends that represent hypotheses that were subsequently investigated through field work for evidence of faulting.

In the near-shore area of the Santa Monica Bay, a unique sub-bottom acoustic survey collected by Dill (1993) was reinterpreted to correlate onshore faults with previously unmapped offshore faults. The seismo-lineament and geomorphic analyses used in the onshore portion of the study area were also implemented to identify potentially seismogenic faults in near-shore portion of the Santa Monica Bay.

GIS Database

A GIS database was compiled from various sources for geomorphic and seismo-lineament analysis. A digital topographic map and shapefile depicting roads in the study area were downloaded from the California Spatial Information Library (http://gis.ca.gov/data.epl). A DEM created by the U.S. Geological Survey at 10 m resolution was obtained from the USGS website (http://earthquake.usgs.gov/regional/states/california/northridge10m_DEMs.php). Aerial photos (DOQQs) were downloaded from the Alexandria Digital Library (http://clients.alexandria.ucsb.edu/webclient/index.jsp). A digital geologic map of the Topanga Quadrangle by Yerkes and Campbell (1997) was downloaded from the USGS website (http://wrgis.wr.usgs.gov/open-file/of95-91/).

Seismo-Lineament Analysis

A database of all available earthquake data within the region was compiled, and multiple focal mechanism solutions were analyzed for seismo-lineaments in the Topanga Quadrangle. A *Mathematica* application developed by Cronin (2004) was used to project a fault-plane solution from the earthquake focus to the DEM-defined surface (appendix a). The outer boundaries of the uncertainty region around the reported focus, depicted in the grey cylinder in figure 6, are defined by the vertical and horizontal uncertainty. Planes that are parallel to the fault-plane solution are translated to the outer edges of the focal uncertainty region; the uncertainty region within which the fault plane is likely to be located is bounded by these planes. (This fault-location uncertainty region is specified using only the focal-location uncertainty. A modified version recently developed by Cronin, but not available for use in this thesis, incorporates the reported uncertainty in the orientation of the fault plane.) The intersection of the fault-location uncertainty region and the DEM-defined surface is an area called a *seismo-lineament swath*. The surface trace of the fault that generated the earthquake will be located within the seismo-

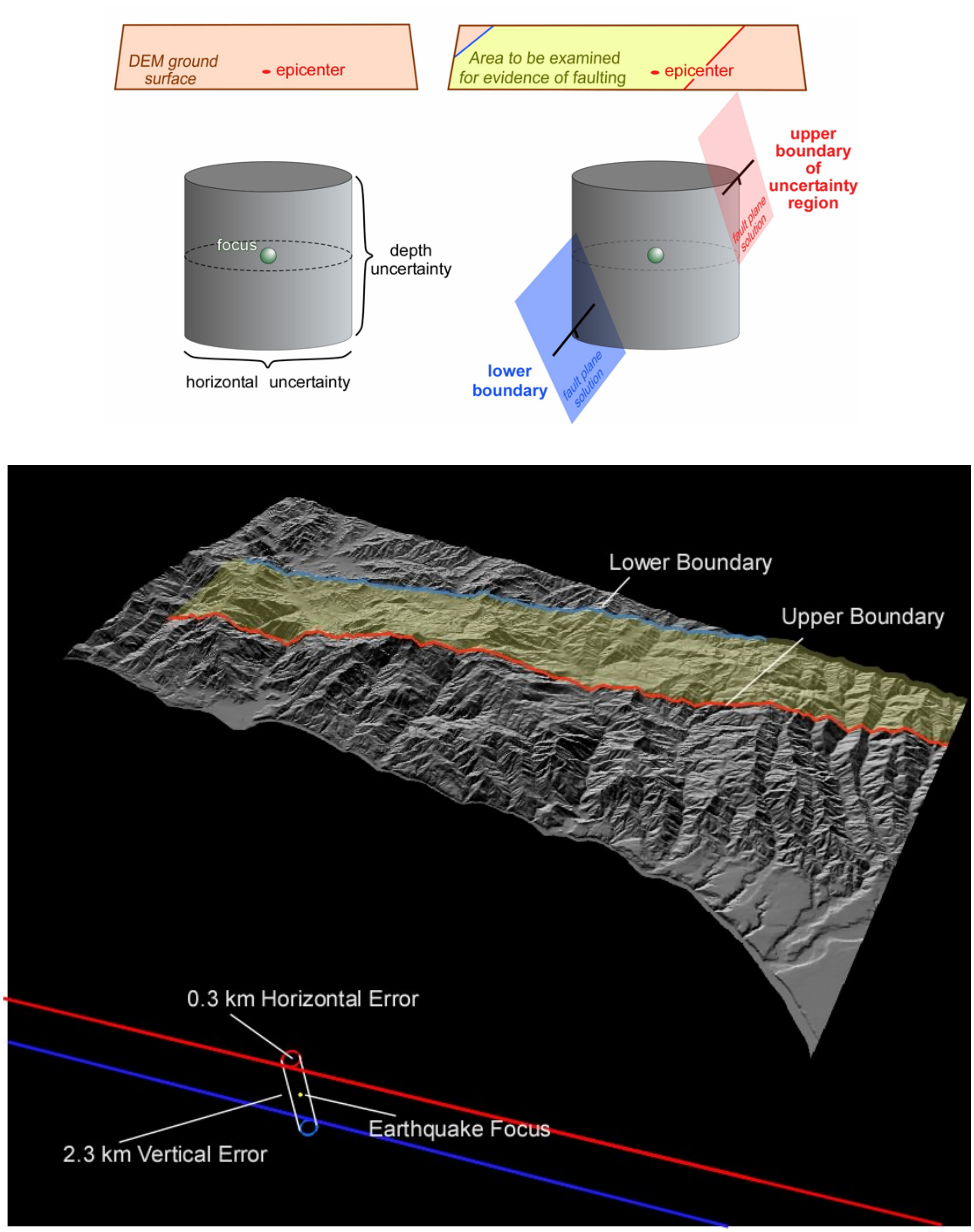

FIGURE 6.—(Upper Image) 3D visualization of the definition of a seismo-lineament swath. Figure from Bayliss and Cronin (2005). (Lower Image) 3D representation of a seismo-lineament swath of an earthquake at a depth of 14 km.

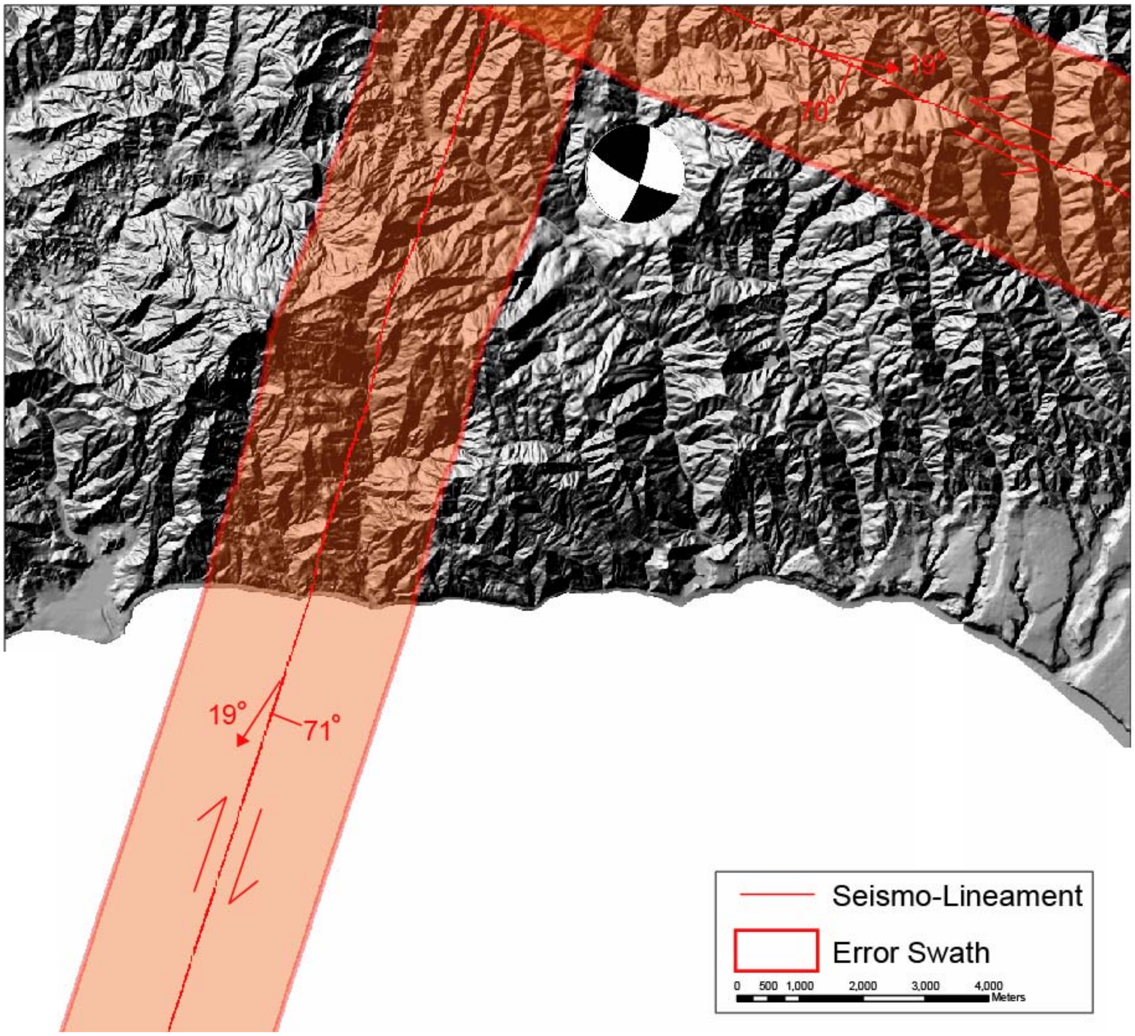

FIGURE 7.—Two seismo-lineament swaths from a focal mechanism solution in the study area.

lineament swath if the fault is planar, the focal-mechanism solution is accurate, and the focus is well located. Each focal mechanism solution provides two nodal planes along which the earthquake could have formed, resulting in two seismo-lineament swaths for each seismic event (figure 7).

In order to test the effectiveness of the seismo-lineament method, it was applied to earthquakes associated with known surface rupture. Events analyzed in the study include the Parkfield (2004, M6), Denali (2002, M7.9), Hector Mine (1999, M7.1), Superstition

Hills (1987, M6.2 and M6.6), Chi Chi (1999; M7.3) and Borah Peak (1983, M7.3) Earthquakes (table 1). The procedure used to test the method involved the projection of published focal mechanism solutions to map layers containing known surface rupture of each earthquake event. After seismo-lineaments were found to intersect known surface rupture, the surface orientation and slip characteristics of the reported surface rupture were compared with the focal mechanism solutions

In this study, twelve focal mechanism solutions from documented earthquakes dating from 1973 to 2003 were evaluated for correlation with faults in the Topanga 7.5' Quadrangle (table 2 and figure 8). After the seismo-lineament files were created in *Mathematica*, they were saved as "dat" files and imported into ArcGIS as raster images using the ArcToolbox "Text to Raster" command. They were then converted to vector shapefiles using the "Spatial Analyst" toolbar.

Geomorphic Lineament Analysis

Faults and joints commonly produce geomorphic lineaments that are visible from aerial photos and other remotely sensed data. In this study, a geomorphic lineament analysis was conducted using artificially illuminated hillshades, and drainage and ridgeline shapefiles derived from a DEM. The purpose of the geomorphic lineament analysis was to identify locations within the seismo-lineament swaths where faults might be located. Cronin and others (1993) defined a geomorphic lineament as "a long (generally ≥ 5 km) colinear or slightly curving array of stream drainage segments or tonal boundaries within the image that does not appear to be related to human construction or other [human] activities." A previous study in Malibu has shown that there are at least two natural scales at which lineaments may be defined; "local" and "composite"

TABLE 1.—Source parameters and surface traces for 7 earthquakes associated with known surface rupture

Event	Source Parameters	Surface Rupture
1983, M 7.3 Borah Peak, ID	Nabelek and others (1985) and Richins and others (1987)	Crone and others (1987)
1983, M 7.3 Borah Peak, ID	Stein and Barrientos (1985) and Richins and others (1987)	Crone and others (1987)
1983, M 7.3 Borah Peak, ID	Ward and Barrientos (1986) and Richins and others (1987)	Crone and others (1987)
1983, M 7.3 Borah Peak, ID	Doser and Smith (1985) and Richins and others (1987)	Crone and others (1987)
2002, M 7.9 Denali, AK	Eberhart-Phillips and others (2003)	Crone and others (2004)
1999, M 7.3 Chi Chi, Taiwan	Chang (2000; 2007)	Chen and others (2001)
1999, M 7.1 Hector Mine, CA	Hauksson and others (2002)	Treiman and others (2002)
1987, M 6.2 Elmore Ranch, CA	NEIC Online Catalog	Sharp and others (1989)
1987, M. 6.6 Superstition Hills, CA	NEIC Online Catalog	Sharp and others (1989)
2004, M 6.0 Parkfield, CA	NEIC Online Catalog	Rymer and others (2006)

TABLE 2.—Earthquakes used in the seismo-lineament analysis.

Date ID (Year-Month-Day-Hour-Minute-Second)	A=Primary B=Auxiliary	Depth (km)	Magnitude	Source
20031031010718	A	11.18	2.94	Hauksson, 2004
19941026041847	B	4.66	2.4	Hardebeck, 2005
19871017092508	A	12.03	2.85	Hardebeck, 2005
20000319063847	B	7.5	2.07	Hauksson, 2004
20010806090728	A	11.32	1.55	Hauksson, 2004
20021014013500	A	9.29	1.9	Hauksson, 2004
20030328054413	A	6.75	2.91	Hauksson, 2004
20030607191122	A	8.09	1.8	Hauksson, 2004
20030801183519	B	7.33	2.32	Hauksson, 2004
19780314235900	B	13.6	3.1	Hauksson, 1990
19800401040200	B	14	2.8	Hauksson, 1990
19730902062804	B	13.9	2.3	Lee and others, 1979

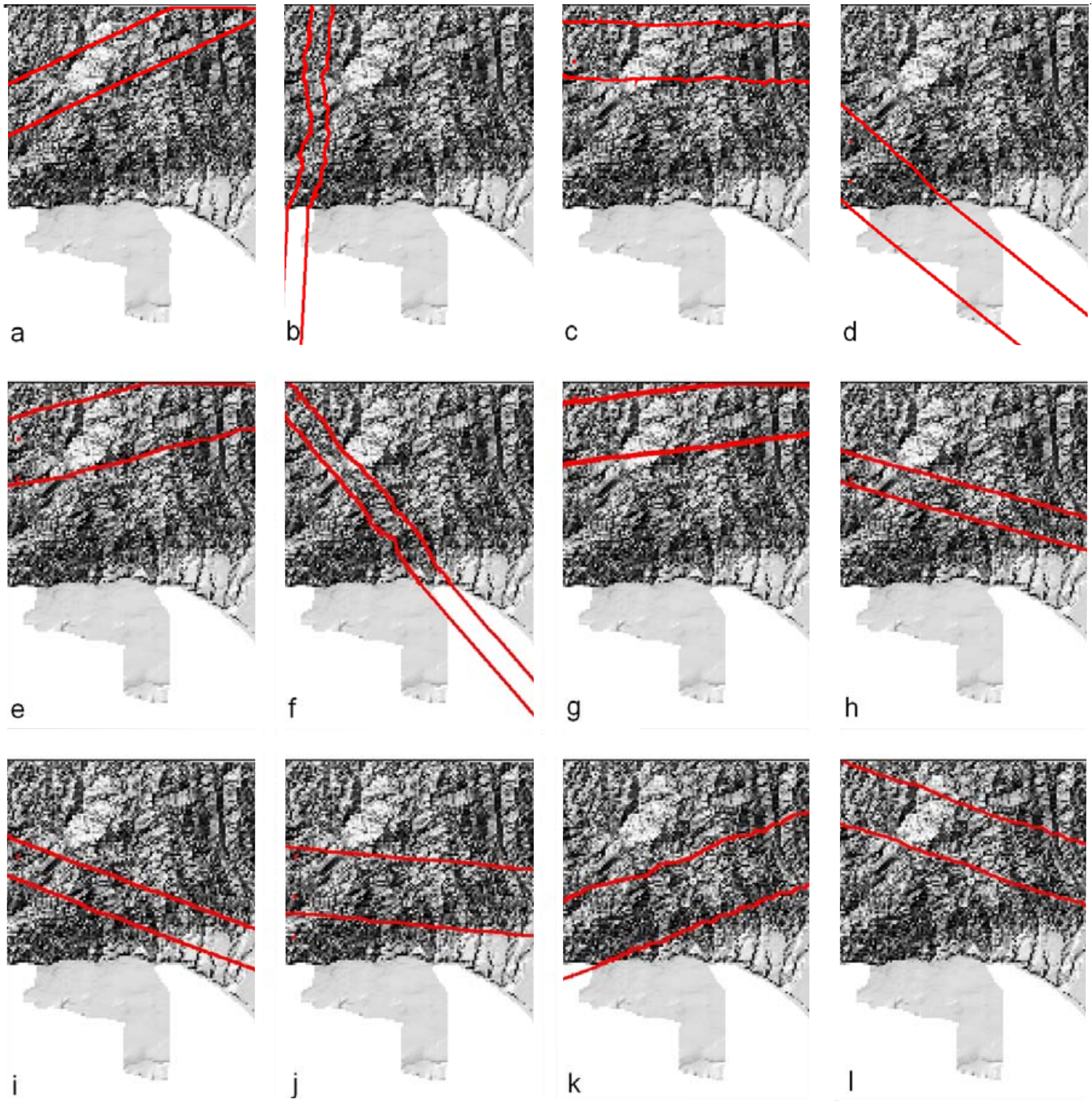

FIGURE 8.—Screenshots of seismo-lineament swaths derived from focal mechanism solutions examined in this study. (a) 20030328054-A, (b) 1994102041-B, (c) 19730902062-B, (d) 19780314235-B, (e) 19800401040-B, (f) 19871017092-A, (g) 2000031906-B, (h) 20010806090-A, (i) 20021014013-A, (j)2003103010-A, (k) 20030607191-A, (l) 20030801183-B.

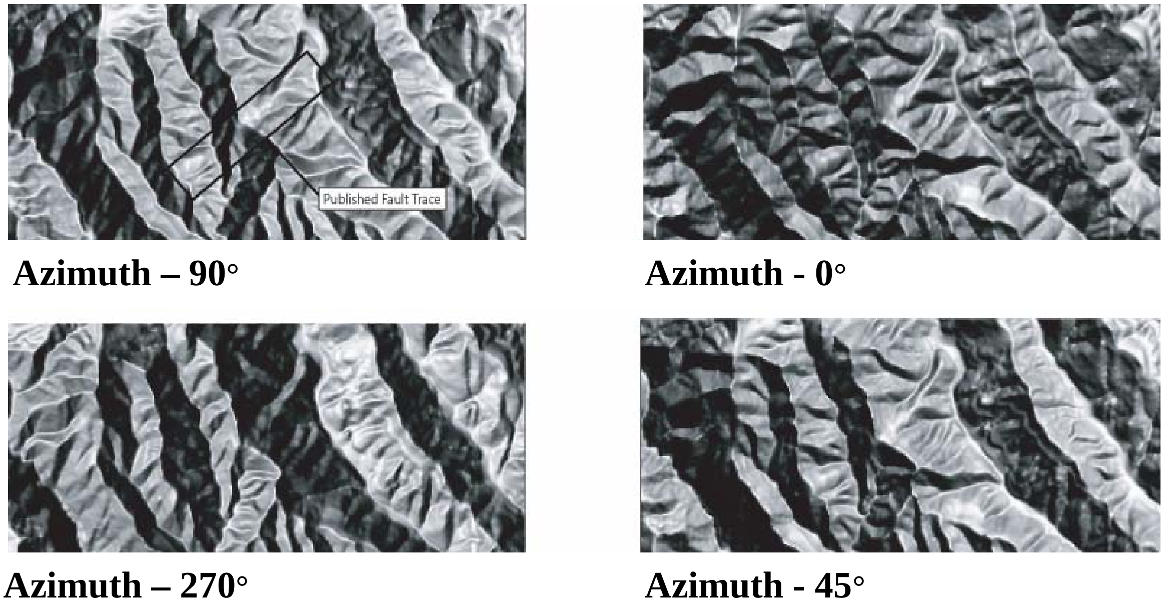

FIGURE 9.—Screenshots of hillshade images created using different sun azimuths. Note the difference in visibility of the surface trace of a published fault in the study area based on the sun azimuth.

(Gammill and Cronin, 2004). Local lineaments are defined as being 0.5 to 2 km in length while composite lineaments consist of a series of local lineaments that may extend for tens of kilometers.

DEMs provide an unobstructed view of the Earth's surface without distractions such as vegetation and man-made objects, which are typical elements of aerial photography. Another benefit of a DEM is that it can be artificially illuminated from multiple directions and elevations, accentuating different features based on the illumination angle (figure 9). A series of hillshade maps were created with the Topanga 10 m DEM using the "raster to hillshade" function in ArcGIS assuming a sun angle of 60º and sun azimuths of 270º, 0º, and 90º.

Using the Hydrology Modeling toolbar in ArcGIS, a shapefile was created which delineates drainages in the study area. To begin the process, a smoothed DEM in which extreme topographic differences are filled in was created using the “fill” function in the ArcToolbox. After creating the smoothed DEM, the flow direction was calculated by applying the “flow direction” function to the topographically smoothed DEM. After creating the grid indicating direction of flow, a new grid which delineates the drainage network was created by applying the “flow accumulation” function to the flow direction grid.

The flow accumulation grid assigns values to each cell based on the slope and elevation of the cell and adjacent cells. In order to create a shapefile that delineates drainage, values that represented the dominant drainage had to be visually identified and extracted from the grid. Grid values that correlated with drainages were in the range of 150 – 580150. This range was determined by classifying the values into intervals and visually determining which values correlated with drainage evident in the topographic map. Using the “reclassification function” in the ArcGIS Editor Toolbar, values that fell within this range were reclassified as “1” while values that did not fall within the range were classified as “2”. Following reclassification, the raster was converted into a shapefile using the “grid to feature” function in the Spatial Analysis Toolbar. Features in the shapefile that had a value of “2” were deleted. The remaining features, with a value of “1”, delineated drainages in the study area.

The same method that was used in the creation of the drainage shapefile was applied to create a shapefile which delineates ridges in the study area. In order to create the shapefile, the original DEM that was used in the drainage creation process was multiplied by “-1”, causing the values that typically depict ridges to be switched with the values depicting drainage. The drainage and ridgeline shapefiles were used in the geomorphic analysis to accentuate anomalies that may not be clearly visible in the DEMs. Alignments involving drainage channels and ridgelines could be easily observed using the data.

In order to perform a repeatable geomorphic lineament analysis, only features that frequently develop along faults were analyzed. A partial list of geomorphic features that may be related to faulting follows (Wesson and others, 1975; McCalpin 1996; Burbank and Anderson, 2001)

a. Stream channels aligned across a drainage divide
b. Lower-order (smaller) stream channels aligned across a higher-order stream channel.
c. Anomalously straight segment of a stream channel
d. Aligned straight segments of a stream channel

e. Lower-order stream channel whose trend is directed upstream relative to the higher-order stream it intersects, so water flowing from the smaller stream into the larger stream has to change directions through an acute angle
f. Abrupt changes in gradient along a stream channel
    (1) Stream channel steps down in direction of flow, evinced by rapids or a waterfall (knick point)
    (2) Stream channel steps up in direction of flow, evinced by a pond
g. Apparent lateral deflection of an incised stream channel or flood plain
h. Abrupt changes in gradient along a ridge crest
    (1) Ridge crest steps down abruptly in the direction the ridge is decreasing in elevation
    (2) Ridge crest steps up in the direction the ridge is decreasing in elevation
    (3) A saddle in the ridge crest
i. Apparent lateral deflection of a ridge crest
j. Abrupt changes in the gradient of a surface localized along a narrow linear step (fault scarp)
k. Benches or faceted spurs at the base of ridges that are unrelated to coastal erosion
l. A set of ridges in an en echelon array
m. A topographic basin along a linear trough (pull-apart basin, sag pond)
n. A topographic hill along a linear trough (pop-up, pressure ridge)

Prior to conducting the geomorphic lineament analysis, a visual analysis of previously published faults in the study area was conducted to determine what geomorphic features typically mark the surface trace of faults in the Topanga Quadrangle

(Dibblee, 1992; and Yerkes and Campbell, 1997). The most commonly observed features in the analysis were: stream channels aligned across a drainage divide, anomalously straight stream segments, aligned segments of a stream channel, abrupt changes in gradient along a ridge crest or along a stream channel, and an abrupt change in the gradient of a surface localized along a narrow linear step (figure 10).

After the files were created in ArcGIS and criteria for identification of potentially fault-related lineaments were determined, the geomorphic lineament analysis was conducted within the seismo-lineament swaths. Lineaments visible from the different illumination angles were traced and combined into a composite map.

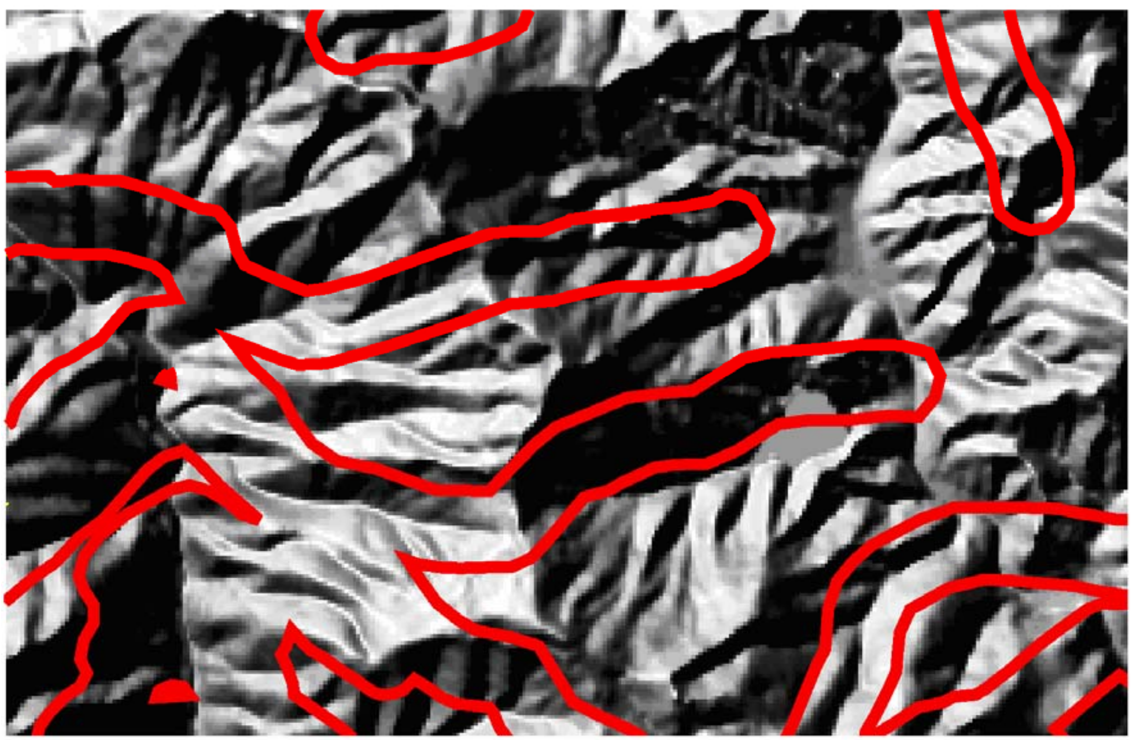

FIGURE 10.—Screenshot of two east-west trending faults in the study area that cut across drainage divides (Red curves mark 50 m buffers placed using ArcGIS around the surface trace of published faults) Published faults from Dibblee (1992).

Field Methods

Seismo-lineament and geomorphic analysis led to hypotheses regarding the location of potentially seismogenic faults. Areas that intersected seismo-lineament swaths were examined in the field to identify evidence of faulting. Due to extensive urbanization and mature vegetation, accessible outcrops in the Topanga Quadrangle are primarily located along road cuts, trails, and fire roads. Where faults were identified in the seismo-lineament swath, data were measured and described. The fault location was mapped using a handheld GPS unit set in UTM format with the NAD 27 datum. Between 7 and 12 measurements of strike, dip, and rake were collected on each fault surface, and descriptions of the fault core, damage zone, and host rock were recorded. Photographs and fault rock samples were also collected.

Correlation of Fault Surfaces with Earthquakes

In order for a fault to be considered correlative with a specific earthquake and potentially seismogenic, three criteria must be met: the surface trace of the fault must be located within the seismo-lineament swath, the fault surface and fault-plane solution must have similar orientations, and the shear striae on the fault and the slip vector of the fault-plane solution must have similar orientations. Faults that did not meet these criteria were not identified as potentially seismogenic. All faults identified within the seismo-lineament swath for a specific earthquake were examined.

Fisher statistics were used to determine the 95% confidence interval of the fault surface and slip-vector measurements using a method by Cronin (2007). The strike, dip, and associated radius of the confidence interval of the fault and focal mechanism solution were plotted on a stereonet. Correlation was determined when error margins from the fault and focal mechanism solution overlapped on the stereonet. To determine if the slip orientation of the fault and the earthquake were correlative, the trend, plunge, and associated confidence interval of the fault and focal mechanism solution were plotted. Similar to strike and dip, correlation was determined when error margins from the fault and focal mechanism solution overlapped on a stereonet (figure 11).

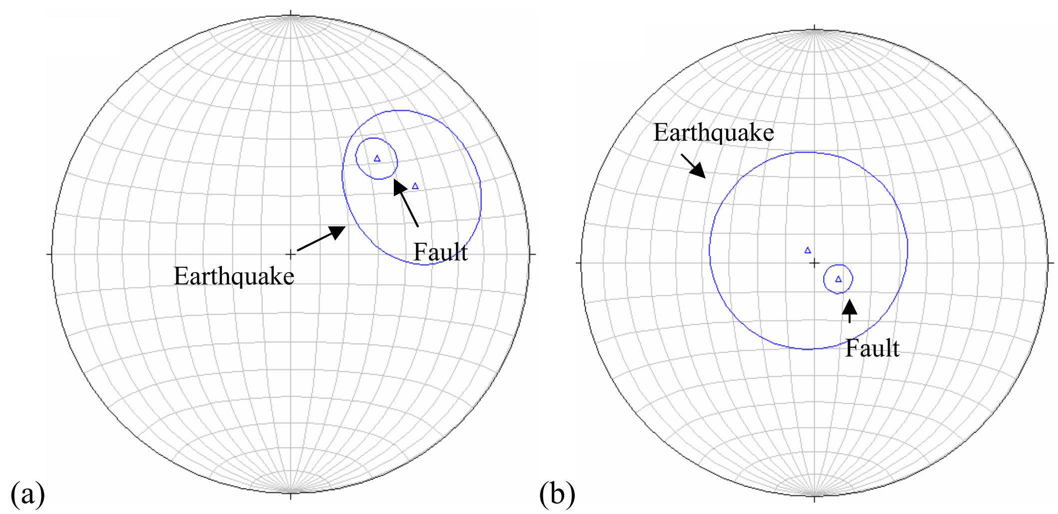

FIGURE 11.—Lower hemisphere, equal area stereonet plots of data showing the correlation between (a) trend and plunge of the slip-vector, and (b) strike and dip of the fault surface.

Near-Shore Sub-Bottom Acoustic Data

The near-shore sub-bottom acoustic data used in this study for creation of the offshore DEMs were contracted by Dr. James E. Slosson and collected by Dr. Robert F. Dill of Dill GeoMarine Consultants and Dr. Tim Norall of EcoSystems Management, Inc., during two independent surveys in the winter of 1993 and summer of 1997. Both surveys were conducted from a specially equipped 25 ft (8.3 m) survey vessel. Navigation during data collection was monitored using a Motorola Mini-Range electronic positioning system with an accuracy of ± 6 ft. (2 m). A dual frequency seismic system designed by EcoSystems Management was used in both studies to determine the acoustic stratigraphy of the study areas. The seismic system recorded data at 3.5 KHz and 200 to 2000 Hz simultaneously. The 3.5 KHz frequency data provided high resolution but shallow penetration while the lower frequency "Boomer" recorders allowed for deep penetration (Dill, 1993; figure 12).

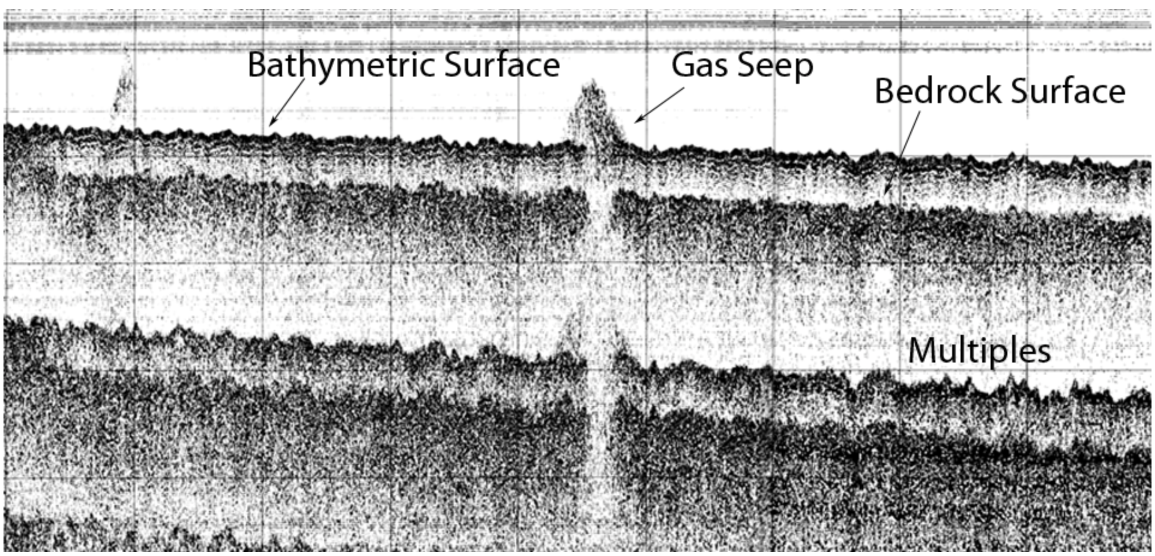

FIGURE 12.—Screenshot 3.5 KHz frequency acoustic data. The feature in the center of the image is a gas screen that wipes out underlying seismic reflections. In low quality seismic data, surfaces are mimicked resulting in what is referred to as a multiple.

The first dataset was collected on July 21-23, 1993, to assess an area of active landslides in the Castellammare Mesa of western Santa Monica, California (Slosson and Dill, 1994). The purpose of the study was to record the seismic stratigraphy of a near-shore portion of the Santa Monica Bay and determine if there was evidence of present or ancient landslides beyond the shoreline.

The study area is located in the Santa Monica Bay seaward of an area known as Castle Rock in the Will Rogers Beach State Park. The seismic lines which were collected parallel to the shore extend from Tuna Canyon to the juncture of Sunset Boulevard and Pacific Coast Highway. The seismic lines extend approximately 2 miles offshore, totaling 35.5 miles of seismic line collected in the study area (Slosson and Dill, 1994).

The second dataset was collected on January 22-24, 1997. The purpose of the study was similar to that of the previous study conducted in 1993; to asses the possibility of the offshore extension of landslides in the area.

The area of interest in the 1997 study lies directly to the west of the 1993 study. It extends parallel to the shoreline from slightly west of Piedra Gorda Canyon to approximately 0.5 miles east of Topanga Canyon. The area extends approximately 1.5 miles offshore towards the south. Tracklines in the eastern portion of the survey overlap with those of the 1993 survey, allowing for merging of the two surveys.

Importing and Combining the Two Surveys

To begin the offshore DEM creation, data from the two surveys were merged into one spreadsheet file with columns delineating the survey name, point number, latitude and longitude, depth to bedrock (ft), depth to seafloor (ft), and sediment thickness (ft). In the paper seismic records the depth is recorded in meters. In order to use the seismic records to adjust values in the dataset, the points were converted to meters. After the files were merged, the new spreadsheet file was converted into a vector point file in ArcGIS using the “add xy data” command.

When comparing data points from the two surveys, it was evident that there existed minor variations in depth in the independent surveys, and a systematically consistent variation in depth along the section of the study area where the two surveys overlapped. Minor depth variations exclusive to the independent surveys are probably due primarily to tidal flux, wave action, and seasonal fluxes in sand. Because these errors were not accounted for during data collection, it is impossible to create an entirely accurate merger of the data. However, applying a method described in more detail below which involved adjusting intersecting “depth to bedrock” values and applying gradients to adjacent points, inaccuracies were minimized, resulting in an adequately realistic interpretation.

The two survey grids consist of lines trending N-S intersected by E-W trending lines. In addition to the N-S and E-W lines, two lines were run which dissect the lines diagonally (figure 13). The average variation in depth values between points at the intersection of any two lines in the 1993 survey was 1.4 ± 0.5 m. The two diagonal lines in the survey were designated as control lines along which all other lines were adjusted. The diagonal lines were chosen as control lines because they intersect a majority of the lines in the survey, and they were both collected in one continuous sweep, resulting in minimal tidal influence. At the intersection of each N-S and E-W line with the diagonal control lines seismic records from the two datasets were compared. Where value of the point did not match the value of the adjacent control point, the point was adjusted to match that of the control line. Data points adjacent to the corrected points on either side were adjusted slightly to create a gradient that gradually reduced to zero. The line that contained the new adjusted value was then used as a temporary control line to adjust other lines that did not intersect the diagonal control lines.

In the spreadsheet file of initial picks made by Dill (1993), some gas screens were mapped as bedrock surfaces. Where this phenomenon occurred, bedrock depths were adjusted according to the depth observed in the seismic paper record and the corresponding sediment thickness value was adjusted to agree with the new picks. After data were corrected for depth variations exclusive to the individual surveys, a method was used to minimize variations in depth between the two surveys. Variations between the two surveys were likely a result of seasonal tidal influence and sand budget, because the two surveys were collected during different times of the year, one in the winter and one in the summer (figure 14).

One hundred eighteen pairs of points from the two surveys that were within 30 meters of each other were analyzed to determine the average difference in depth between

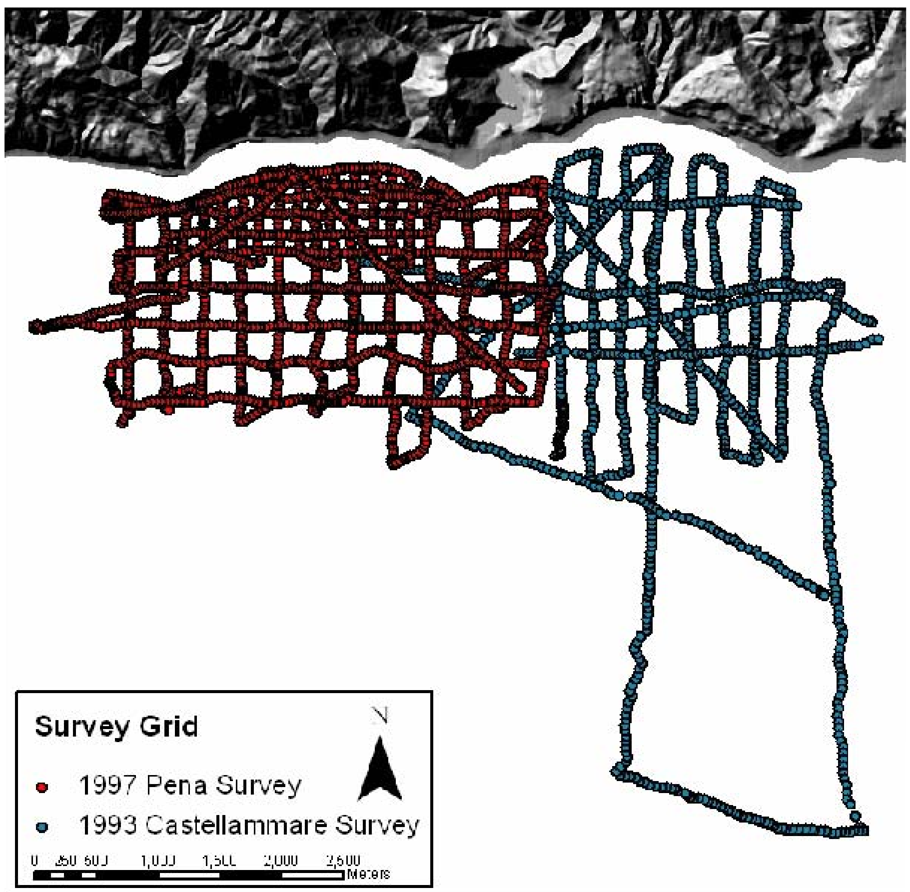

FIGURE 13.—Map of tracklines for the two individual surveys. Note the two diagonal lines in each survey used to correct errors in the individual surveys and the area of overlap used to correlate the two surveys.

TABLE 3.—Depth difference of overlapping points from the two different surveys. Note 52 pairs of matching points after data correction.

Initial Data Points Depth Difference (m)	# of Pairs	Corrected Data Points Depths Difference (m)	# of Pairs
0	1	0	52
1	13	1	51
2	51	2	14
3	40	3	1
4	3	4	0

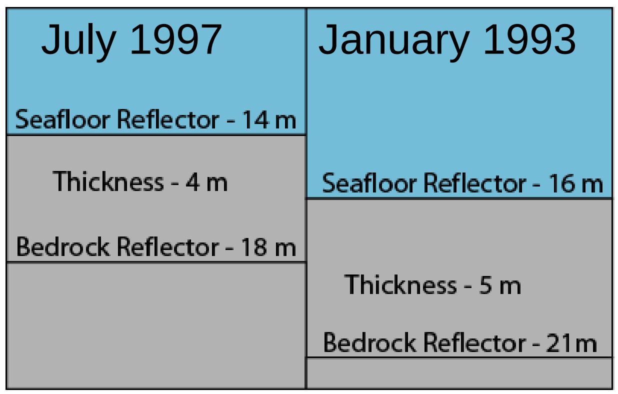

FIGURE 14.—Diagram showing typical variations in sediment thickness and water level that affected the two surveys.

corresponding points in the two surveys. The pairs had an average depth difference of 2.4 ± 0.2 m. In order to minimize the difference between the two surveys, 2.4 m were added to all of the seafloor and bedrock values in the 1997 survey. After adding 2.4 m, the average difference between two adjacent data points was less than 1 meter (0.7 ± 0.1 m) (table 3). The remaining mismatched pairs were adjusted using the same method employed on the individual surveys

Raster Interpolation and Merging

After the data points were corrected and correlated between the two surveys, 2 m contours of bedrock and seafloor depths were created by hand and digitized as shapefiles in ArcGIS 9.1. Hand contouring was chosen because contouring algorithms in ArcGIS and Erdas Imagine resulted in cosmetic errors related to the location of the tracklines. Using the "Topo-to-Raster" tool in the ArcGIS Toolbox, continuous rasters for the bedrock and seafloor surfaces were created with 1 x 1 m horizontal resolution (figures 15 and 16). After creating the bedrock and bathymetric rasters, a raster was created depicting the thickness of unconsolidated sediment in the study area by subtracting the bathymetric raster from the bedrock raster using the Raster Calculator in ArcGIS (figure 17).

The seafloor raster was merged with a bathymetric survey by Dartnell and others (2004) using the "mosaic function" in the ArcGIS Toolbox. The survey by Dartnell and others was produced at 16 x 16 m resolution, and it was necessary that the seafloor DEM be resampled at the same resolution to allow for merging (figure 18). At the intersection of the bathymetric survey and seafloor raster, a blending function in the ArcToolbox was applied. This created a smooth transition between the two surveys (figure 19). The bedrock DEM was merged with the onshore USGS DEM using the ArcToolbox in ArcGIS. Elevation values in the USGS DEM were recorded in feet with a pixel size of 10 m. The offshore bedrock DEM was converted to feet using the Raster Calculator in ArcGIS and resampled to a pixel size of 10 m (figure 20).

Interpretation of Offshore Data

The original intent of the offshore surveys was to characterize offshore landslide movement (Dill, 1994). Due to the scope of the original project, the type of seismic data collected does not penetrate deeply, which would be beneficial for interpretation of faults. The interpretation of possible offshore connections of the Santa Monica Fault and the

Malibu Coast Fault Zone was based on topographic trends in the bedrock surface, zones denuded of sediment, and lineation of gas seeps. Areas that correspond spatially with seismo-lineaments were also analyzed to identify possible geomorphic indicators of fault movement.

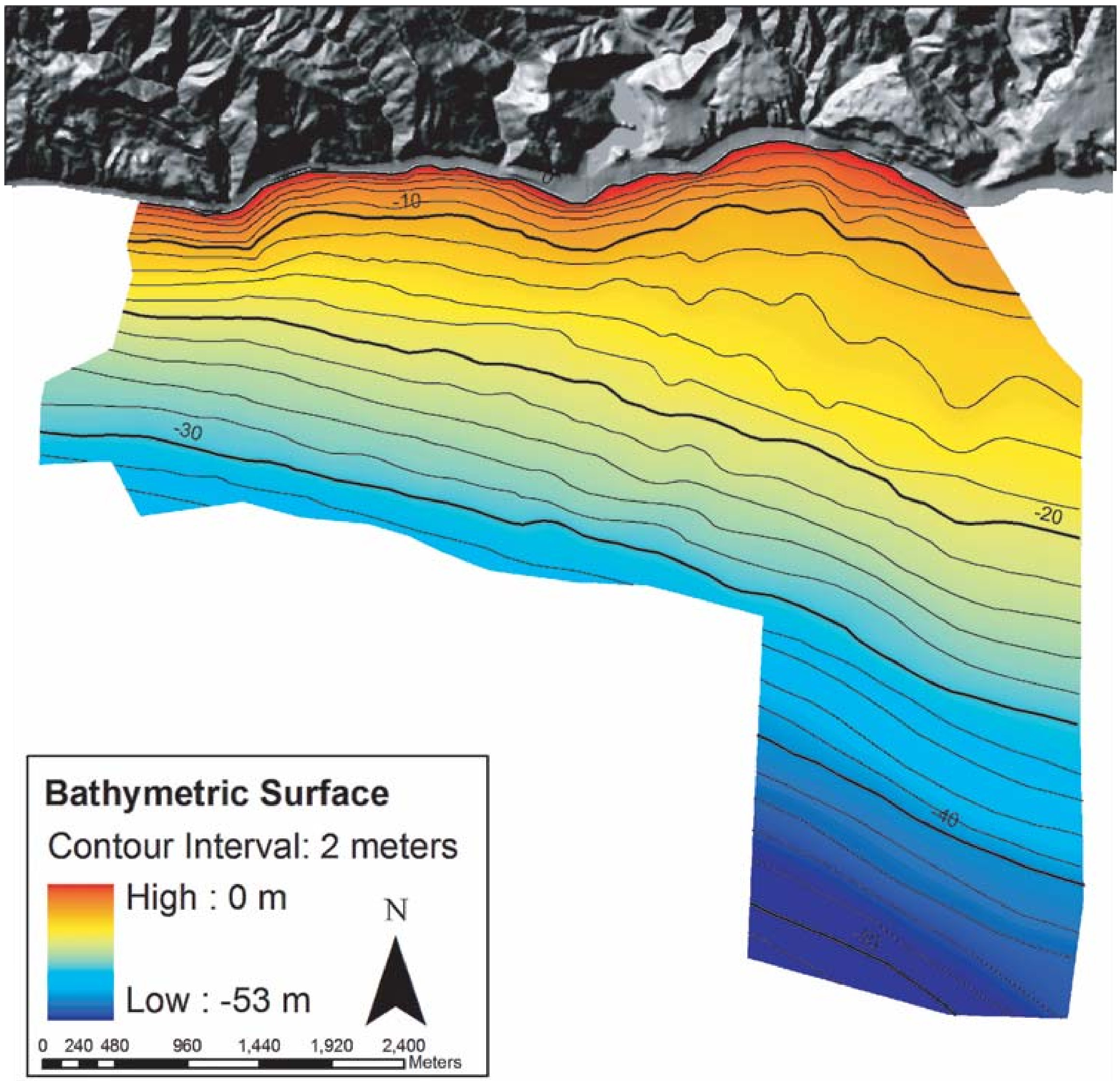

FIGURE 15.—Bathymetric surface map of offshore study area. Data were contoured by hand.

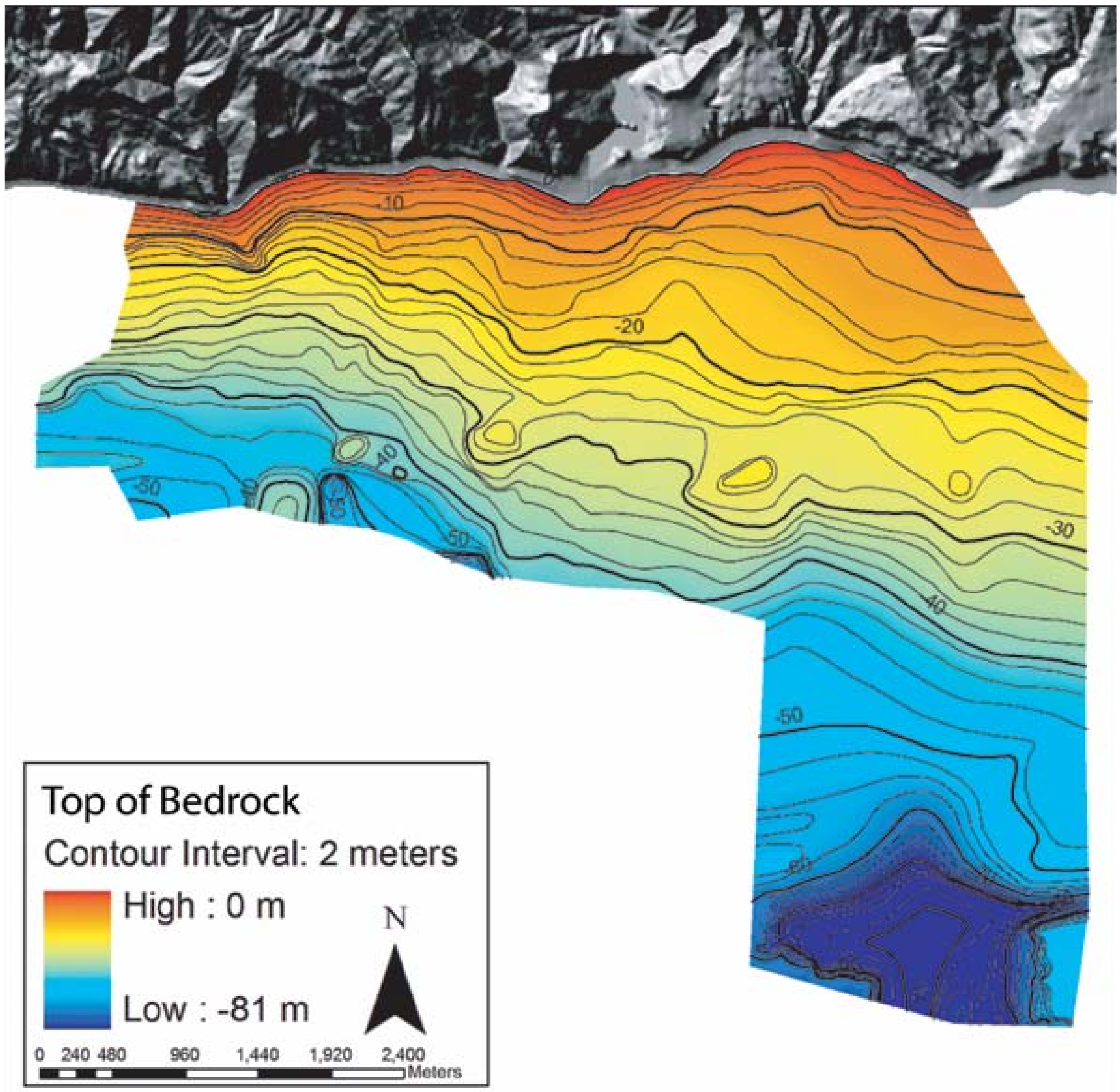

FIGURE 16.—Structure map of top of acoustic bedrock reflectors in seismic survey. Data were contoured by hand.

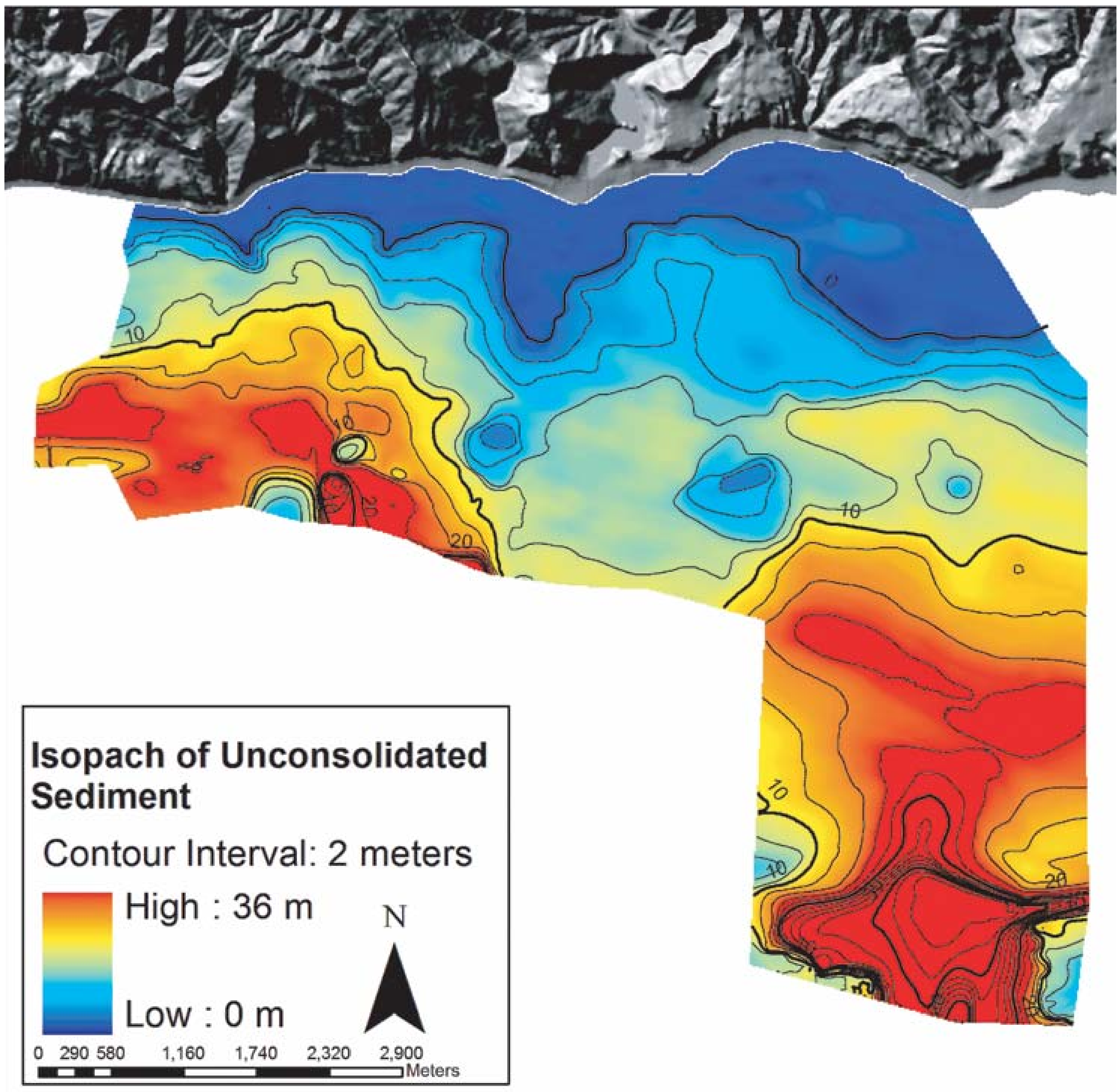

FIGURE 17.—Isopach of unconsolidated sediment in offshore study area interpreted as Holocene by Dill (1993).

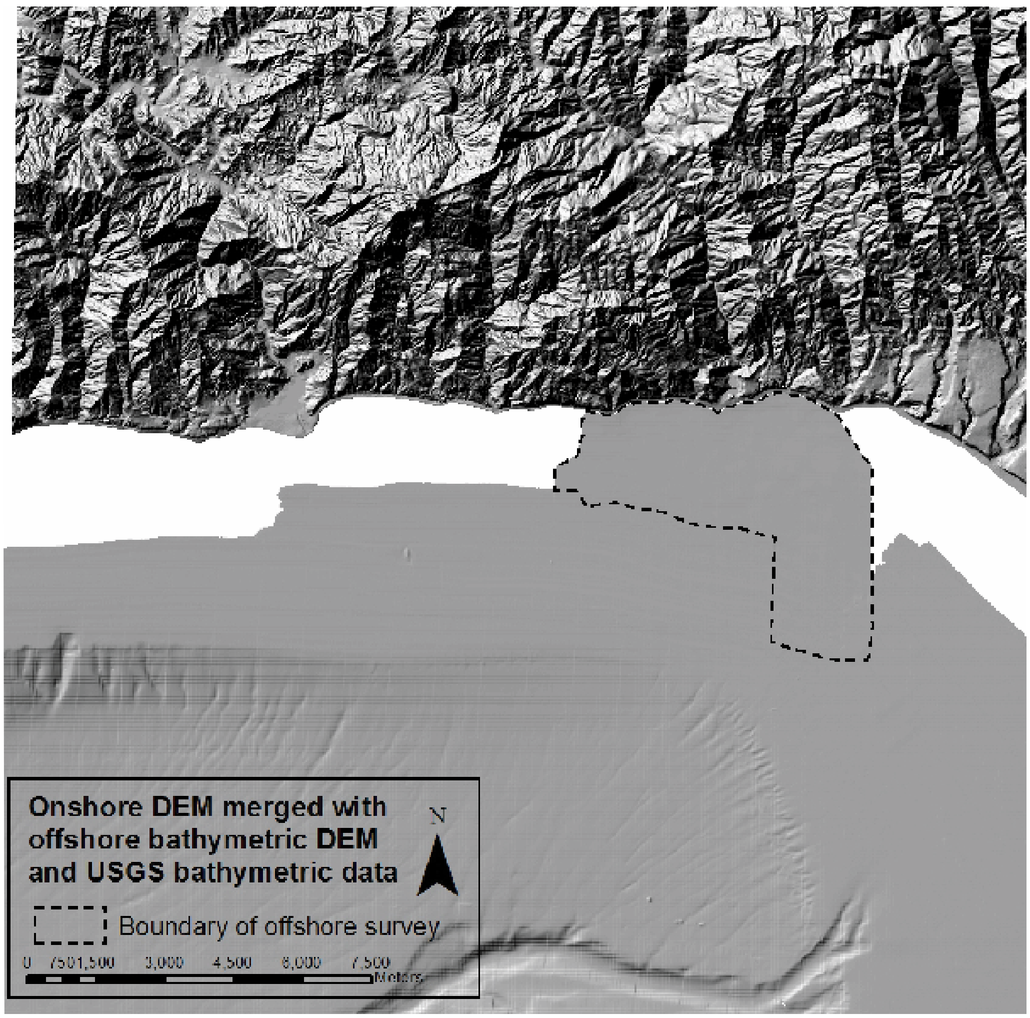

FIGURE 18.—Hillshade of bathymetric surface merged with USGS Bathymetric data and DEM images of the Malibu Beach and Topanga 7.5' Quadrangles (Dartnell and others, 2004).

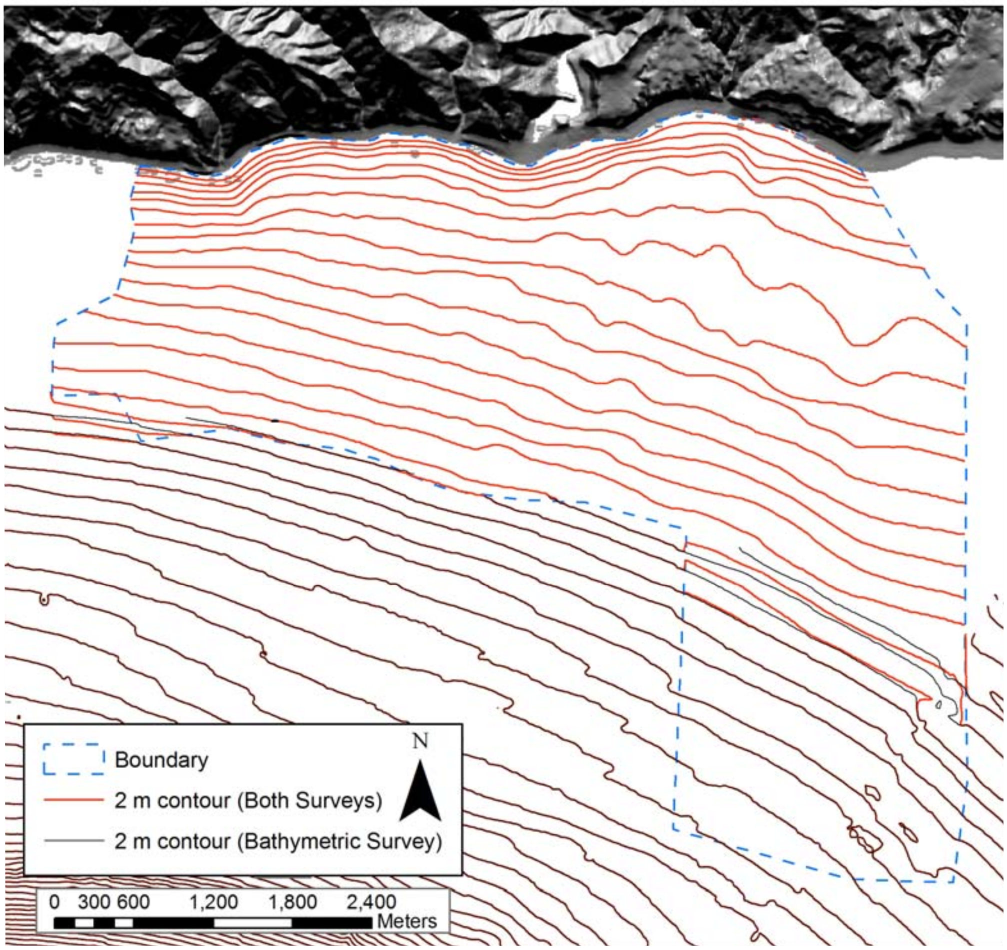

FIGURE 19.—Map showing minor differences between depth values in the original bathymetric survey (brown) by Dartnell and others (2004) and the near-shore survey combined with the bathymetric survey (red). Note minor variations in contour lines near the left-center and lower-right portions of the map.

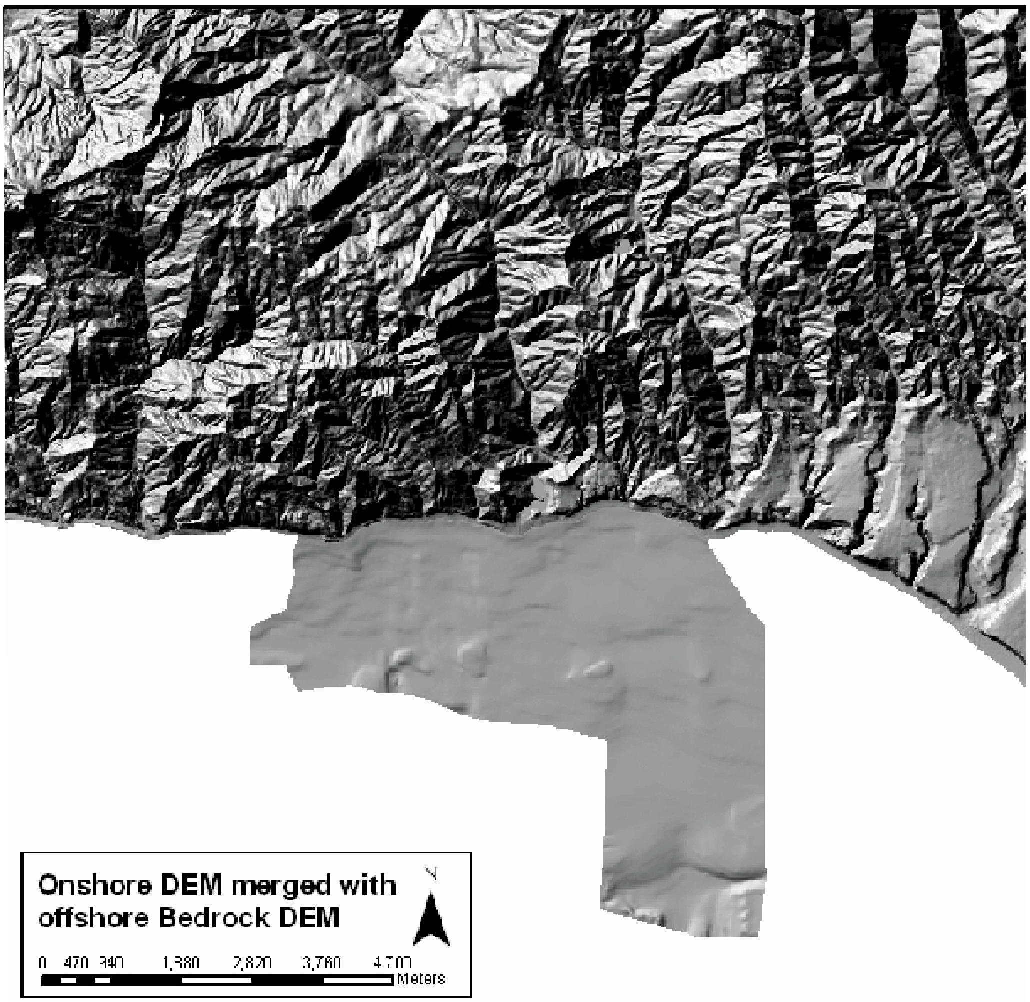

FIGURE 20.—Hillshade of offshore acoustic bedrock surface merged with to USGS onshore DEM.

CHAPTER FOUR

Results

Introduction and Onshore Data

In order to test the effectiveness of the seismo-lineament methods, it was applied to earthquakes associated with known surface rupture. In all of the tests, the ground-rupture associated with the surface rupture was located within the seismo-lineament swath, supporting the validity of the seismo-lineament method. Surface and slip orientations from the surface ruptures were similar to those of the published focal mechanism solutions (figures 21 and 22 and appendix B)

A geomorphic lineament map was used in conjunction with aerial photos and maps displaying boundaries of the seismo-lineament swaths to conduct field work in the study area (figure 23). Twenty-eight faults were identified and analyzed to determine their correlation with the earthquake events. Twenty of the faults were previously unmapped (figure 24).

Saddle Peak 1 Fault

The Saddle Peak 1 Fault is located in a roadcut at UTM 0350067, 3771465 at mile marker 1.69 on Saddle Peak Road. The elevation of the outcrop is ~2,263 ft. The total damage zone of the fault is 76 ± 2.5 cm wide and marked by offset beds of the Lower Topanga Formation as mapped by Dibblee (1992), and a drag fold on the right side (hanging wall) of the fault (figure 25). The fault has a dip azimuth of 329° ± 15° and dip angle of 76° ± 4°. Slickenlines on the surface of the fault have a trend of 356° ± 20° and plunge of 75° ± 5°. The left side of the fault (footwall) consists of a medium to thinly-bedded, very-fine sandstone underlain by basalt. At the base of the roadcut, a volcanic unit overlies poorly-sorted, coarse-grained sandstone with conglomerate interbeds. No damage zone was observed on the footwall of the fault.

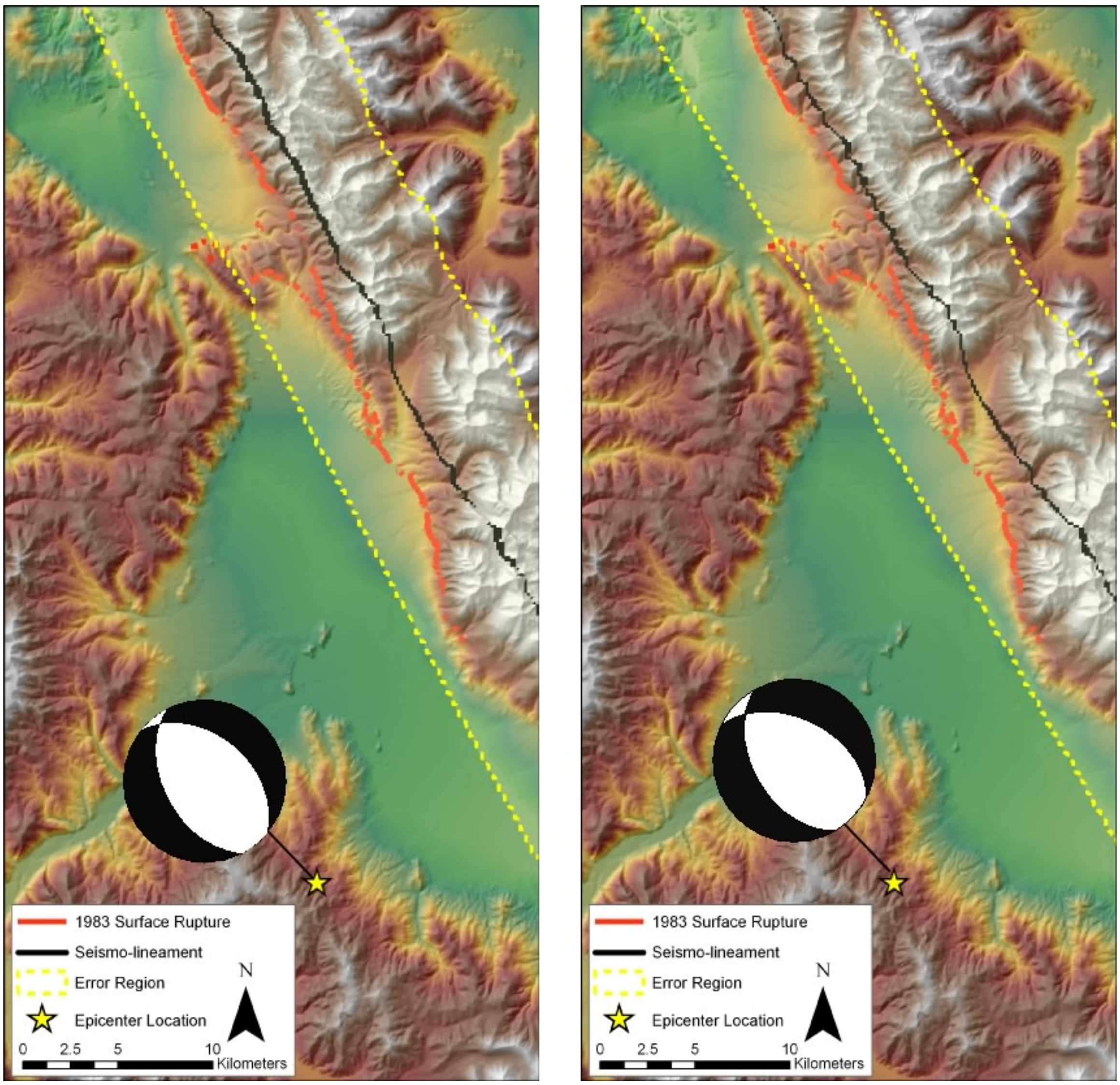

FIGURE 21—Screenshots of seismo-lineaments from the 1983, Borah Peak, ID Earthquake projected to the surface of DEM. Source parameters for the earthquake on the left by Ward and Barrientos (1986), and on the right by Nabelek and others (1986).

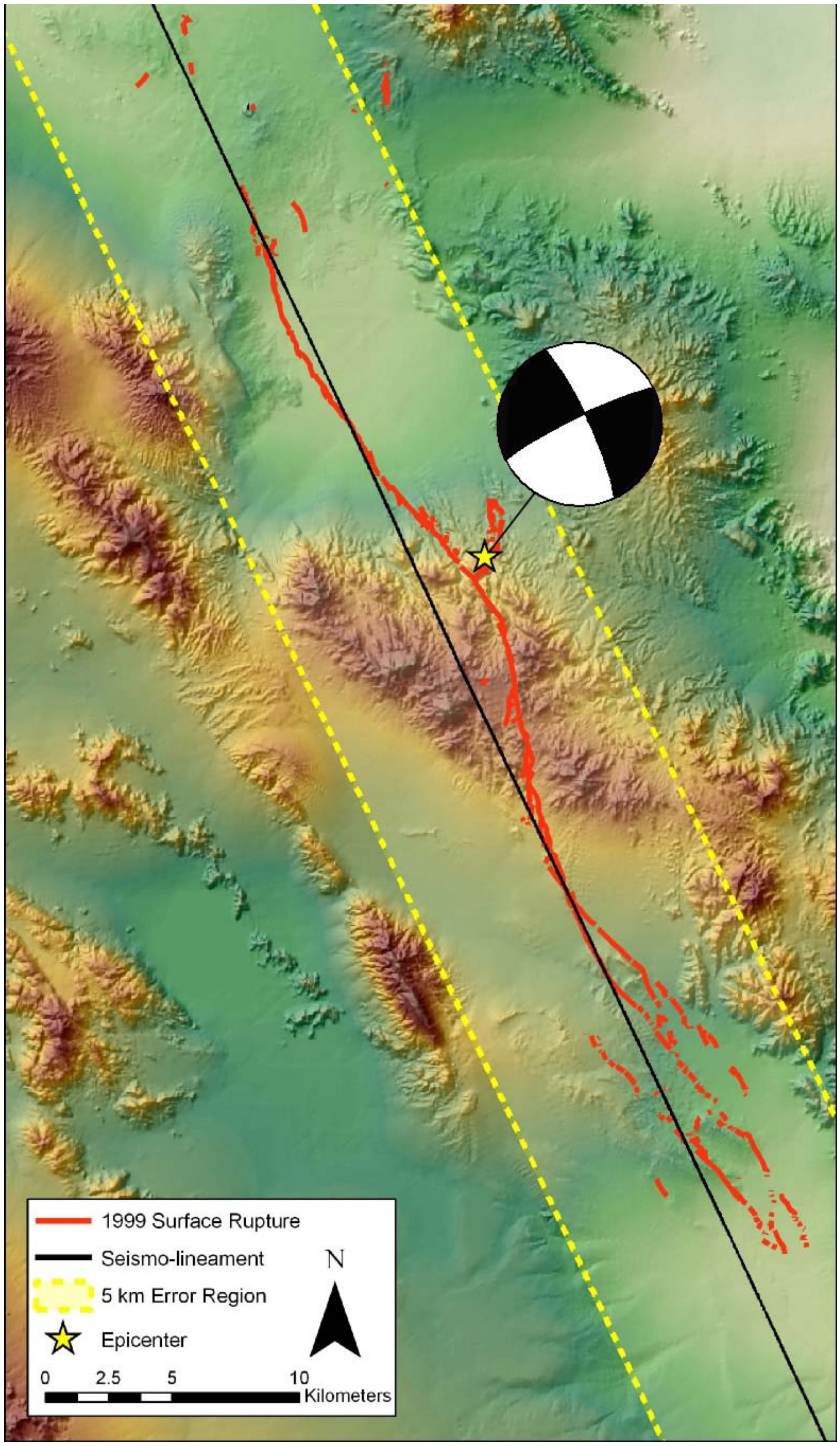

FIGURE 22.—Screenshot of seismo-lineament from the 1999, Hector Mine, CA Earthquake. Source parameters from the NEIC online catalog.

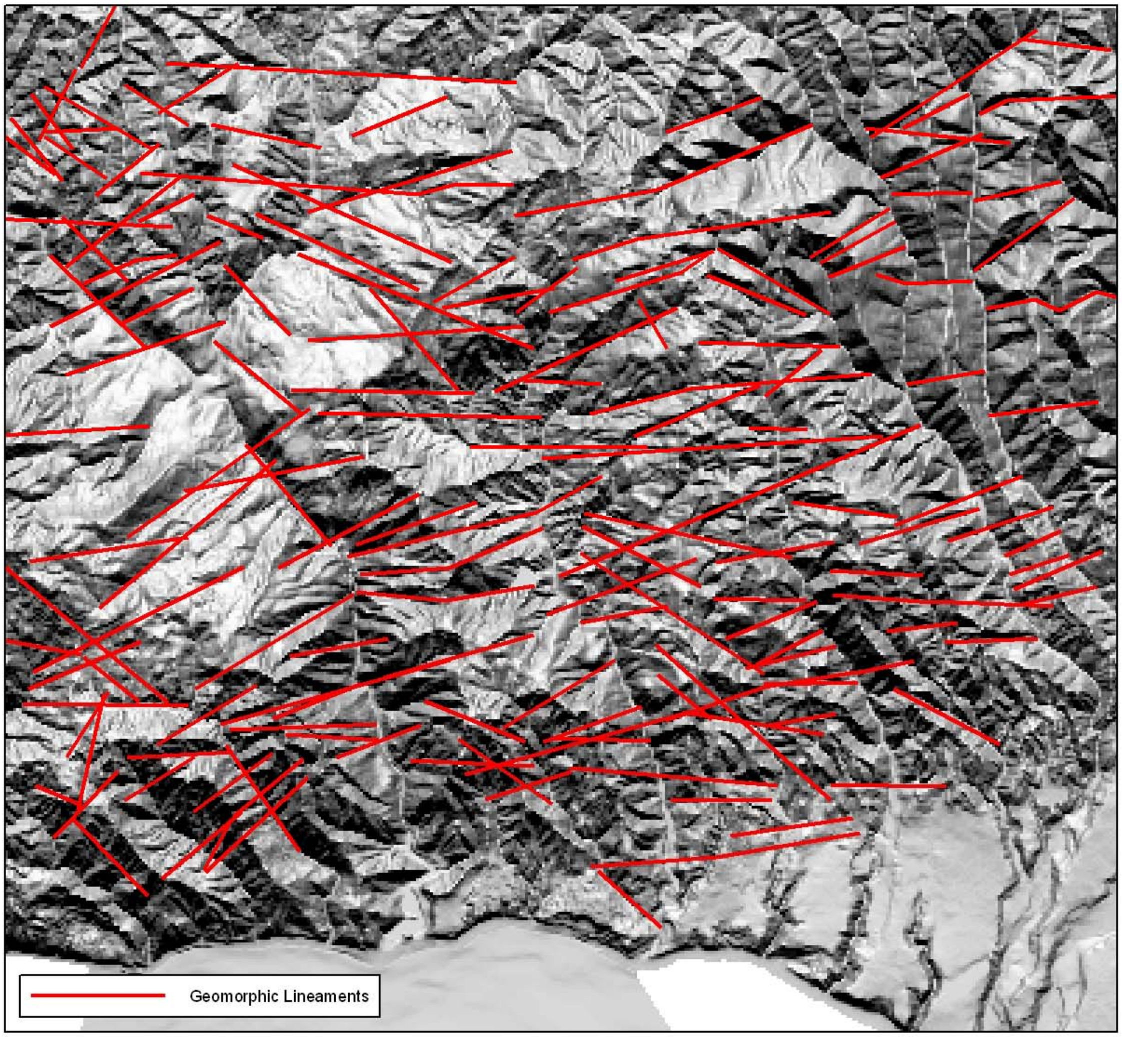

FIGURE 23.—Geomorphic lineaments identified in the study. Only lineaments that were within the seismo-lineament swaths were recorded

The fault rock consists of a fine fault gouge commingled with small angular clasts. The hanging wall consists of a medium to thinly-bedded, very-fine sandstone underlain by basalt. The two units in the footwall likely correlate with the upper two units in the hanging wall, suggesting minor vertical displacement. The hanging wall in the vicinity of the fault is highly fractured, and has experienced drag and layer parallel slip along the beds, evidenced by cataclasite along the bedding planes. Beds on the left side of the fault are sub-horizontal, dipping 15° to 20°, while beds on the right side of the fault vary in dip from 30° to 70°. The fault zone is directly adjacent to a small drainage, and potentially related to development of the drainage. Although the Saddle Peak 1 Fault is located within the surface trace of one or more seismo-lineaments examined in the study, the fault does not meet the other criteria and therefore is not considered potentially seismogenic.

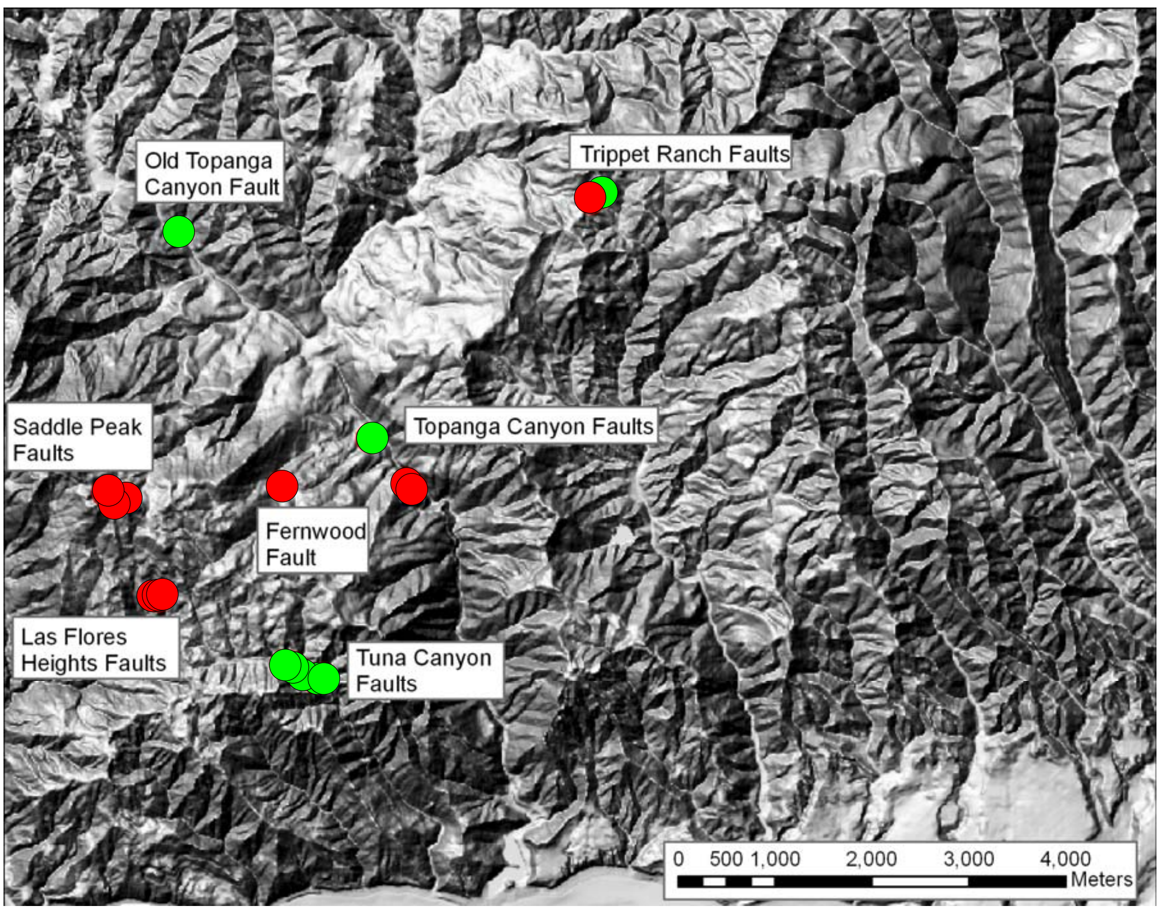

FIGURE 24.—Map showing location of previously-mapped (green) and unmapped (red) faults identified during field work. Names were given to faults in this study based on their geographic location.

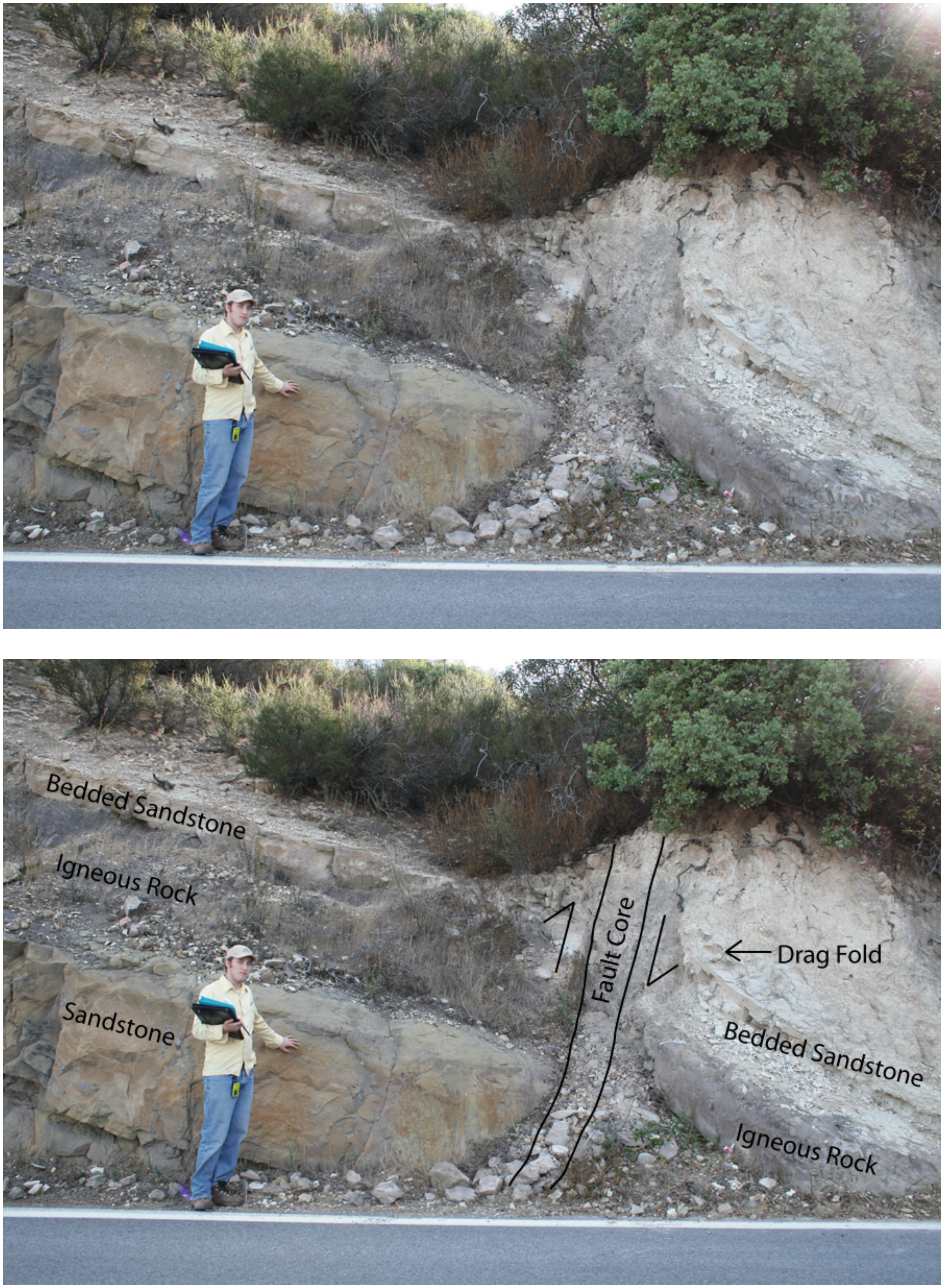

FIGURE 25.—(a) Uninterpreted and (b) interpreted photograph of the Saddle Peak 1 Fault. Note drag fold in the footwall resulting from fault movement. Also note correlation of bedded sandstone and igneous rock on both sides of the fault.

Saddle Peak 2 Fault

The Saddle Peak 2 Fault is located in a roadcut at UTM 0350189, 3771534 at mile marker 1.8 on Saddle Peak Road. The elevation of the outcrop is ~2286 ft. The fault is present in rocks of the Lower Topanga Canyon Formation as mapped by Dibblee (1992), and has a dip azimuth of 124° ± 27° and dip angle of 80° ± 5°. Slickenlines on the surface of the fault have a trend of 42° ± 10° and plunge of 45° ± 7°. The fault rock consists of a 9 ± 5 cm thick zone of coarse-grained, grayish-yellow fault gouge with angular, pebble-sized clasts of sandstone. The damage zone consists of a 2-2.5 m wide zone of minor fractures on the left side of the fault (hanging wall) and extensive fracturing on the right side (footwall). Also present in the footwall are numerous faults with very minor offset.

The left side of the fault consists of dark, highly-weathered basalt underlain by very-coarse, poorly-sorted sandstone with some conglomerate interbeds. The unit contains more conglomeratic beds at the base. The right side of the fault consists of a grayish-yellow, poorly-sorted conglomerate with ~80% cobble and boulder size clasts underlain by 1-2 m of grayish yellow, very-coarse, poorly-sorted sandstone with ~5% cobbles. The fault is also present in an outcrop across the road from the roadcut. Although the definite sense of displacement is unknown, it appears as though the lower conglomerate unit on the left side of the fault correlates with the conglomerate at the top of the right side of the fault. This would indicate ~5 m of throw (figure 26). Due to the low rake of slickenlines, the fault does not appear to be caused by road construction. Directly to the east of the outcrop is a moderately large drainage. It is possible that the drainage is established along a more significant fault parallel to the one exposed in

FIGURE 26.—(a) Uninterpreted and (b) interpreted photograph of the Saddle Peak 2 Fault.

outcrop, but the covered interval renders it unrecognizable in the absence of a trench study. Although the Saddle Peak 2 Fault is located within the seismo-lineament for the 20030328054-A event, the fault does not meet the other criteria and therefore is not considered potentially seismogenic.

Saddle Peak 3, 4, and 5 Faults

The Saddle Peak 3, 4, and 5 Faults are located at UTM 0350012, 3772569, west of mile marker 1.69 on Saddle Peak Road. The elevation of the outcrop is ~2313 ft. The Saddle Peak 3 Fault is marked by offset beds of the Lower Topanga Canyon Formation as mapped by Dibblee (1992), and extensive jointing in the roadcut (figure 27). The fault has a dip azimuth of 132° ± 11° and dip angle of 38° ± 8°. Slickenlines on the surface of the fault have a trend of 152° ± 9° and plunge of 36° ± 7°. The fault core consists of light-tan gray cataclasite with some fault gouge. The damage zone is ~10 m wide, and consists of very extensive jointing on the left side of the fault (hanging wall) and moderate jointing on the right side of the fault (footwall). The rock on both sides of the fault consists of light tan gray, coarse-grained, poorly-sorted sandstone with conglomerate interbeds underlain by 2 m of medium-bedded, medium- to coarse-grained sandstone. Vertical offset of the fault is ~25 cm.

To the right of the Saddle Peak 3 Fault are the Saddle Peak 4 and 5 Faults which are exposed in rocks of the Lower Topanga Canyon Formation as mapped by Dibblee (1992). The Saddle Peak 4 Fault has a dip azimuth of 131° ± 25° and dip angle of 84° ± 2°. No slip-direction indicators are visible on the fault surface. The vertical displacement is unknown because beds are not correlative on either end of the fault. The Saddle Peak 5 Fault has a dip azimuth of 101° ± 14° and dip angle of 68° ± 5°. No slip-

FIGURE 27.—(a) Uninterpreted and (b) interpreted photograph of the Saddle Peak 3 and 4 Faults.

direction indicators are visible on the fault surface. Approximately 3 m of vertical displacement is evidenced by light gray, silty sandstone that is offset on both sides of the fault. All three of the faults appear to have both a lateral and normal component slip. Although the Saddle Peak 3, 4, and 5 Faults are located within the surface trace of one or more seismo-lineaments examined in the study, the faults do not meet the other criteria and therefore are not considered potentially seismogenic.

Fernwood 1 Fault

The Fernwood 1 Fault is located in a roadcut at UTM 0351785, 3771650 at mile marker 0.11, exiting the village of Fernwood. The elevation of the outcrop is ~1337 ft. The rock on both sides of the fault is a poorly fractured medium-brown, medium to coarse-grained sandstone and conglomerate interbeds of the Lower Topanga Canyon Formation as mapped by Dibblee (1992) (figure 28). The fault is a nearly vertical "credit card" fault (i.e., has a very thin to negligible gouge zone) with a dip azimuth of 244° ± 33° and dip angle of 81° ± 5°. Slickenlines on the surface of the fault have a trend of 158° ± 3° and plunge of 16° ± 3° with some mineralization on the surface. Lack of a damage zone and fault rock suggests that only minor slip has occurred along the fault. The fault may be related to a larger fault zone that could be buried in the drainage adjacent to the roadcut. No geomorphic effect of the fault is evident.

A fault in approximately the same location as the Fernwood 1 Fault, but with a different orientation, is on the published map of the Topanga Quadrangle by Yerkes and Campbell (1997). Although the fault is located within the surface trace of one or more seismo-lineaments examined in the study, the fault do not meet the other criteria and therefore are not considered potentially seismogenic.

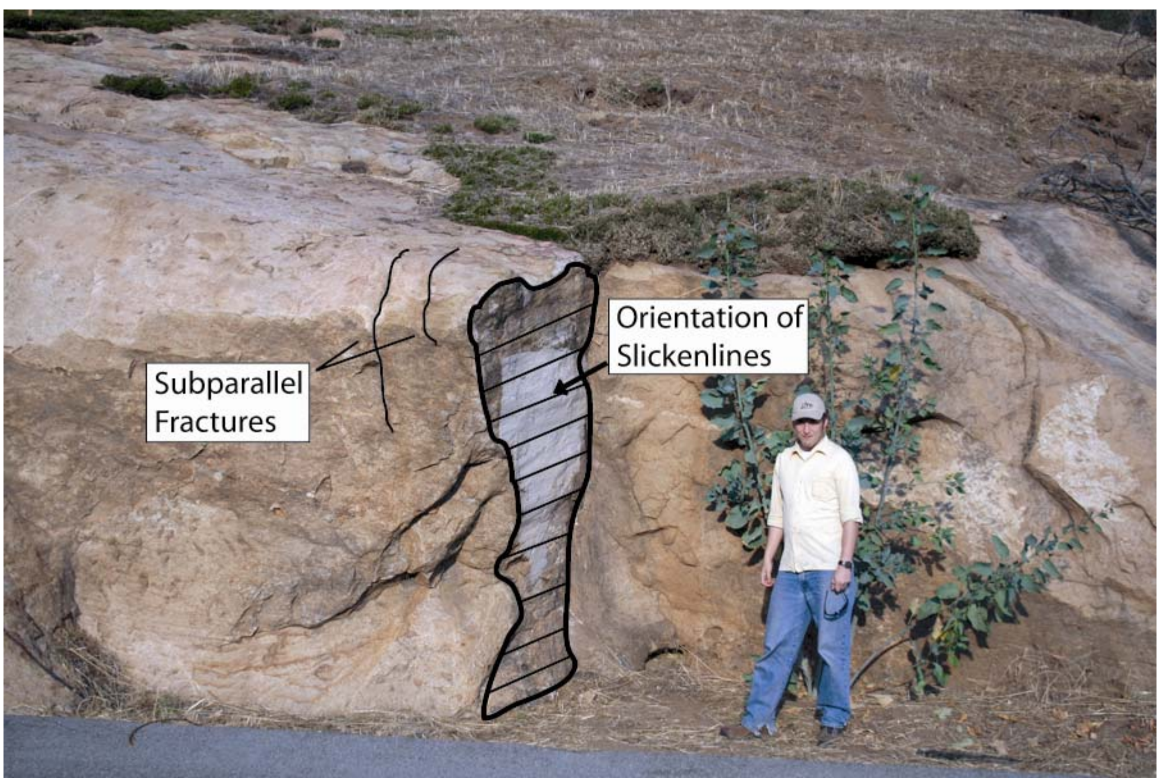

FIGURE 28.—(a) Uninterpreted and (b) interpreted photograph of the Fernwood 1 Fault.

Las Flores Heights 1 Fault

The Las Flores Heights 1 Fault is located in a roadcut at UTM 0350515, 3770494 at a bend in Las Flores Heights Road. The elevation of the outcrop is ~1588 ft. The width of the fault is unknown because only one side of the fault is exposed at this site due to road construction and valley development parallel to the fault (figure 29). The fault has a dip azimuth of 82° ± 15° and dip angle of 61° ± 7°. Slickenlines on the surface have a trend of 122° ± 8° and plunge of 39° ± 6°. The rock is a light-brownish gray to dark-yellowish orange, poorly-lithified, very coarse-grained, poorly-sorted conglomeratic sandstone. It is poorly to moderately fractured and contains multiple parallel striated surfaces. Due to the nearly horizontal orientation of striations, the fault does not appear to be related to landslides or road construction.

The Las Flores Heights 1 Fault is located within the seismo-lineament swath for the 20031031010718-A and 20030607191-A events. The trend and plunge of slickenlines, and strike and dip of the fault surface fall within the range of possible orientations for the earthquake events. The fault and the earthquake event are similar in spatial location, fault orientation, and slip direction, suggesting that the fault is potentially seismogenic (figure 30).

Las Flores Heights 2 Fault

The Las Flores Heights 2 Fault is located at UTM 0350478, 3770511 on Las Flores Heights Road. The elevation of the outcrop is ~1580 ft. The fault is evidenced by extensive fracturing and a large surface with multiple slickenlines in rocks of the Lower Topanga Formation as mapped by Dibblee (1992). The fault has a dip azimuth of 228° ±

FIGURE 29.—(a) Uninterpreted and (b) interpreted photograph of Las Flores Heights 1 Fault.

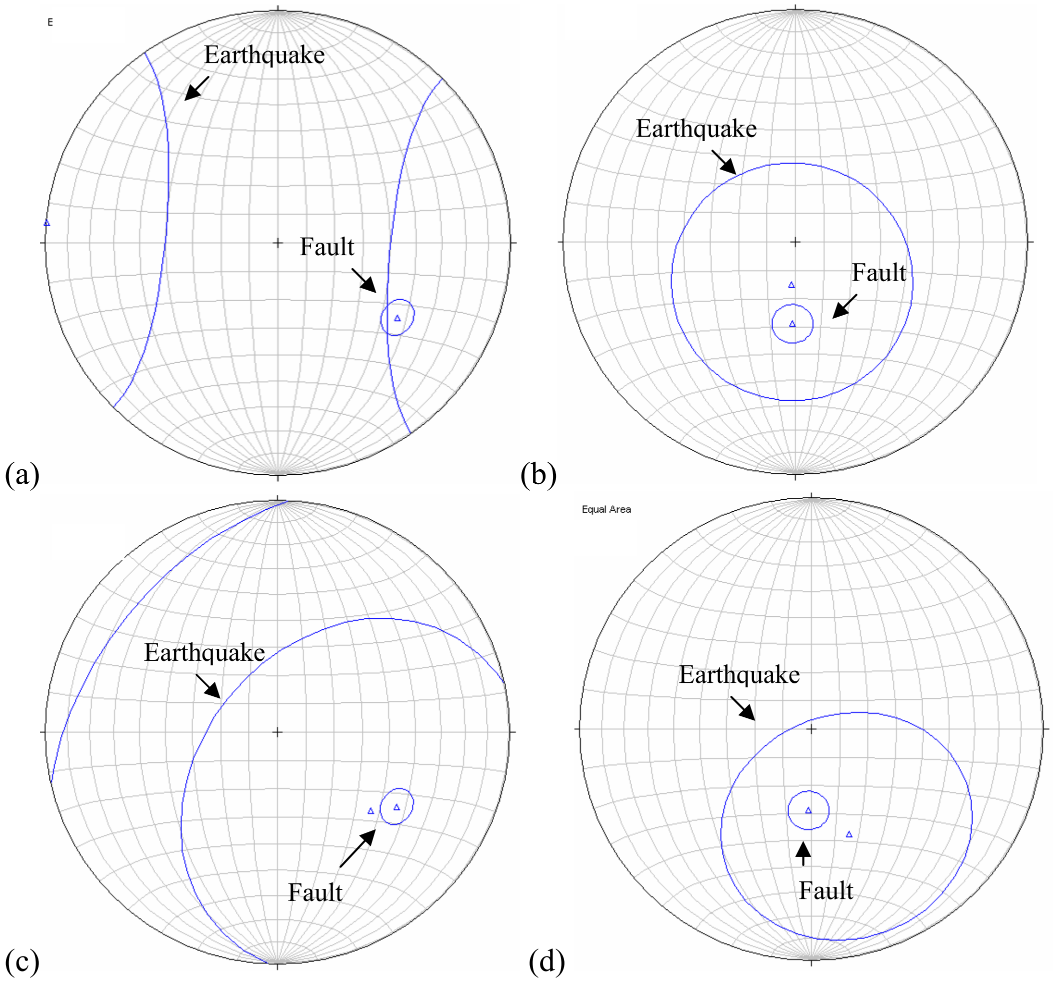

FIGURE 30.—Lower hemisphere, equal area projection of data from earthquake events 20031031010718-A and 20030607191-A, and the Las Flores Heights 1 Fault. Ellipses bound the 90% C.I. of (a) slip-vector, (b) fault surface orientation, (c) slip-vector, and (d) fault surface orientations (Stereonets created using Stereonet for Windows v.1.2 by Richard Allmendinger).

8° and dip angle of 50° ± 5°. Slickenlines on the fault surface have a trend of 144° ± 4° and plunge of 8° ± 4°. Only the footwall and less than ~1 m of the hanging wall of the fault is exposed because the fault parallels the road. No fault rock is exposed in the outcrop. Rock on both sides of the fault consists of shallow dipping, light tan, poorly-sorted, coarse-grained sandstone. The fault does not appear to be involved in landsliding. Although the Las Flores Heights 2 Fault is located within the surface trace of one or more seismo-lineaments examined in the study, the fault does not meet the other criteria and therefore is not considered potentially seismogenic.

Las Flores Heights 3 Fault

The Las Flores Heights 3 Fault is also located at UTM 0350478, 3770511 on Las Flores Heights Road in rocks of the Lower Topanga Formation as mapped by Dibblee (1992), and displaces the Las Flores Heights 2 Fault. The elevation of the outcrop is ~1580 ft. The fault has a dip azimuth of 124° ± 3° and dip angle of 54° ± 2°. Slickenlines on the fault surface have a trend of 199° ± 4° and plunge of 20° ± 3°. The fault core consists of ~0.5 to 2 cm light tan, weathered cataclasite. Rock on both sides of the fault consists of shallow-dipping, light-tan, poorly-sorted, coarse-grained, highly fractured sandstone (figure 31). To the right of the fault is a sub parallel fault with ~2 cm of cataclasite in the fault core.

The Las Flores Heights 3 Fault is located within the seismo-lineament swath for the 20030607191-A event. The trend and plunge of slickenlines, and strike and dip of the fault surface fall within the range of possible orientations for the earthquake event. The fault and the earthquake event are similar in spatial location, fault orientation, and slip direction, suggesting that the fault is potentially seismogenic (figure 32)

Las Flores Heights 4 Fault

The Las Flores Heights 4 Fault is located at UTM 0350490, 3770510 on Las Flores Heights Road. The elevation of the outcrop is ~1578 ft. The fault is marked by a ~3 m wide damage zone with a 68 ± 12 cm wide fault core in rocks of the Lower Topanga Formation as mapped by Dibblee (1992). The fault has a dip azimuth of 124°

and dip angle of 85° ± 9°. No measurable slickenlines are visible on thesurface of the fault. The fault core consists of grayish orange, moderately- to well-cemented fault breccia with 5% sand matrix. Many of the clasts in the fault core have slickenlines on the surface. The damage zone extends ~1 m on both sides of the fault, and is characterized by extensive tightly-spaced fractures that parallel the fault (figure 33). Although the Las Flores Heights 4 Fault is located within the surface trace of one or more seismo-lineaments examined in the study, the fault does not meet the other criteria and therefore is not considered potentially seismogenic.

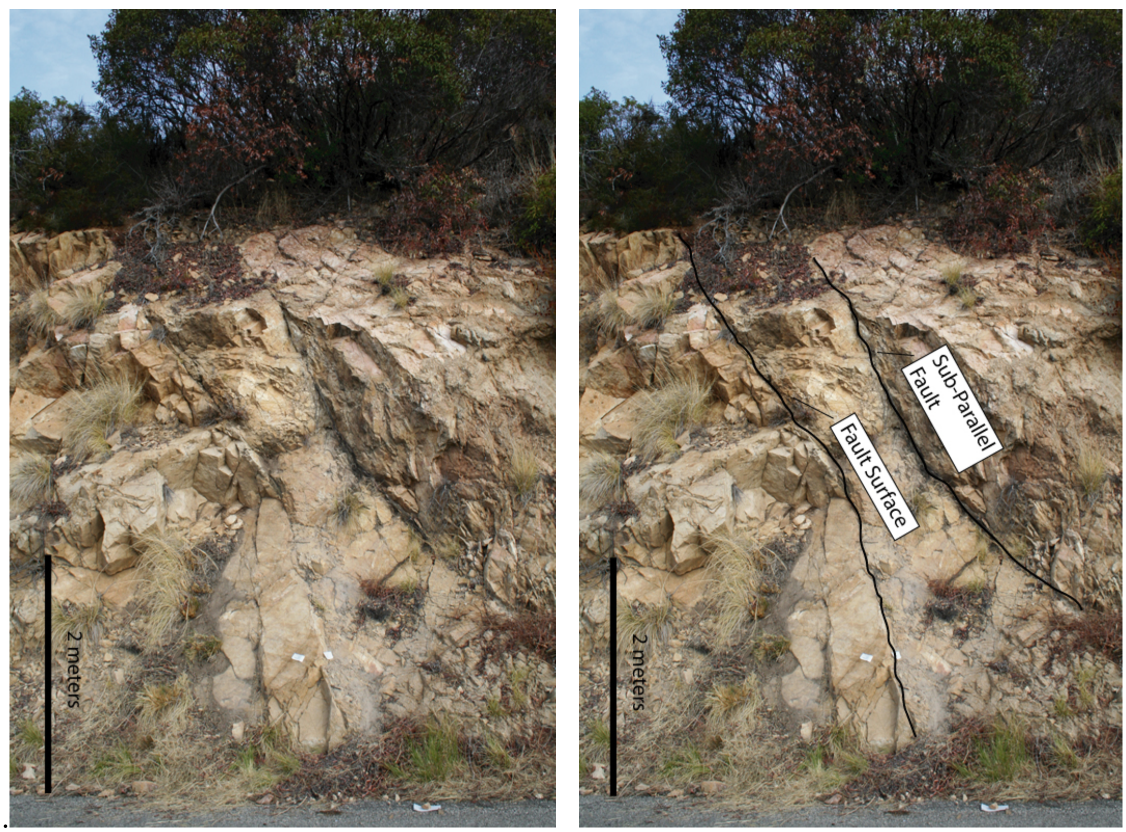

FIGURE 31.—(a) Uninterpreted and (b) interpreted photograph of Las Flores Heights 3 Fault.

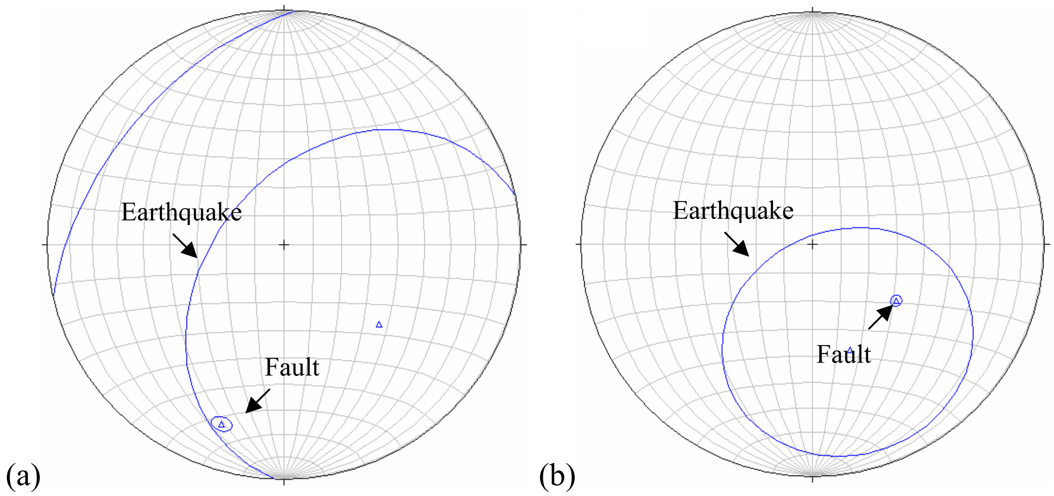

FIGURE 32.—Lower hemisphere, equal area projection of data from earthquake event 20030607191-A and the Las Flores Heights 3 Fault. Ellipses bound the 90% C.I. of (a) slip-vector, and (b) fault surface orientation. (Stereonets created using Stereonet for Windows v.1.2 by Richard Allmendinger).

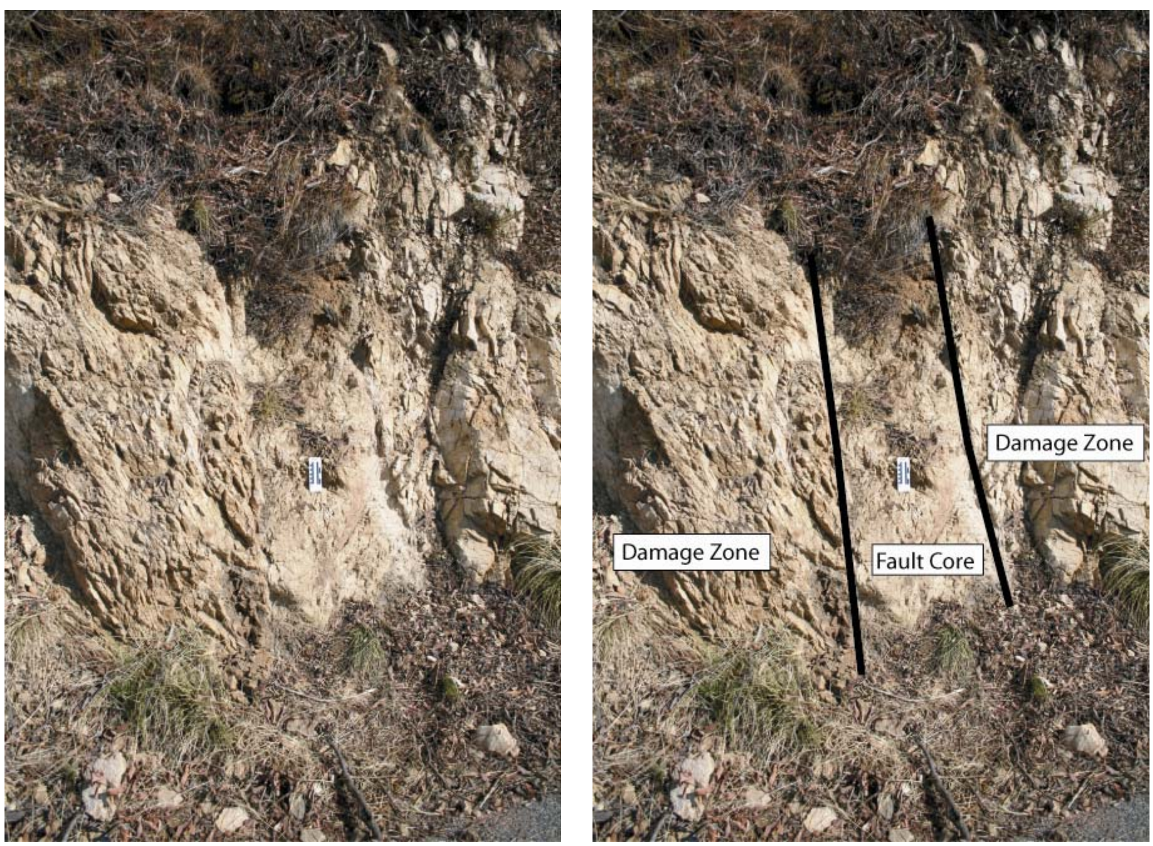

FIGURE 33.—(a) Uninterpreted and (b) interpreted photograph of Las Flores Heights 4 Fault. Note 6 in. (15.25 cm) ruler for scale.

Las Flores Heights 5 Fault

The Las Flores Heights 5 Fault is located at UTM 0350500, 3770500 on Las Flores Heights road. The elevation of the fault is ~1591 ft. The fault is marked by the truncation of beds in the roadcut (figure 34). The fault has a dip azimuth of 341° ± 14°and dip angle of 75° ± 4°. No measurable slickenlines are visible on the surface of the fault due to extensive weathering of the fault surface. Fault rock consists of moderate yellowish brown, brittle fault gouge. The damage zone is ~4 m wide, and characterized by extensive jointing and striated surfaces on clasts in the zone. Rocks on the left side of the fault (hanging wall) consist of moderate brown and dark yellowish brown very-coarse, moderately- to poorly-sorted sandstone conglomerate. Rocks on the right side of the fault (footwall) consist of moderate yellowish brown, fine-grained volcanic rock underlain by red gray, very-coarse, sandstone. Weathering of the fault zone has resulted in the development of a small drainage in the side of the roadcut which lines up with drainage in a bench across the canyon.

The Las Flores Heights 5 Fault is located within the seismo-lineament swath for the 20031031010718-A event. The strike and dip of the fault surface fall within the range of possible orientations for the earthquake events. However, since slip-vector were not available due to weathering of the fault surface, the fault does not meet the criteria and therefore cannot be considered potentially seismogenic (figure 35).

Las Flores Heights 6 Fault

The Las Flores Heights 6 Fault is located in a roadcut at UTM 0350527, 3770491, immediately adjacent to Las Flores Heights 1 Fault at a bend in Las Flores Heights Road. The elevation of the outcrop is ~1636 ft. The width of the fault is unknown because only

FIGURE 34.—(a) Uninterpreted and (b) interpreted photograph of Las Flores Heights 5 Fault. No slickenlines were visible on the fault surface.

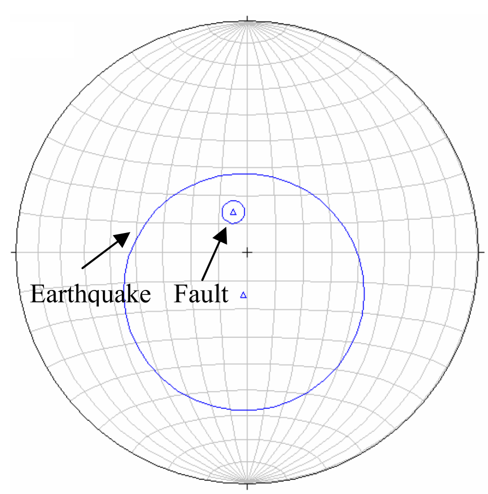

FIGURE 35.—Lower hemisphere, equal area projection of 90% C.I. of strike and dip data from earthquake event 20031031010718-A and the Las Flores Heights 5 Fault. (Stereonet created using Stereonet for Windows v.1.2 by Richard Allmendinger).

one side of the fault was exposed at this site due to road construction and valley development parallel to the fault (figure 36). The fault is in rocks of the Lower Topanga Formation as mapped by Dibblee (1992), and has a dip azimuth of 164° ± 7° and dip angle of 42° ± 5°. Slickenlines on the surface have a trend of 236° ± 5° and plunge of 15° ± 5°. The lithology consists of light brownish gray to dark yellowish orange, poorly lithified, very coarse-grained, poorly-sorted conglomeratic sandstone. Underlying the sandstone is a light-brownish-orange igneous rock that is extremely weathered. Due to the nearly horizontal rake of striations, the fault does not appear to be related to landslides or road construction.

The Las Flores Heights 6 Fault is located within the seismo-lineament swath for the 20031031010718-A event. The trend and plunge of slickenlines, and strike and dip of the fault surface fall within the range of possible orientations for the earthquake event. The fault and the earthquake event are similar in spatial location, fault orientation, and slip direction, suggesting that the fault is potentially seismogenic (figure 37).

Tuna Canyon 1 Fault

The Tuna Canyon 1 Fault is located in a roadcut at UTM 0351824, 3769804 at mile marker 2.97 on Tuna Canyon Road. The elevation of the outcrop is ~1363 ft. The fault is evidenced by a striated surface and highly-weathered fault breccia present in rocks of the Santa Susana Formation as mapped by Dibblee (1992). The fault has a dip azimuth of 341° ± 10° and dip angle of 77° ± 2°. Slickenlines on the surface of the fault have a trend of 52° ± 6° and plunge of 54° ± 3°. The fault surface contains relatively deep grooves ~1-2 cm deep that parallel the slickenlines. This suggests significant

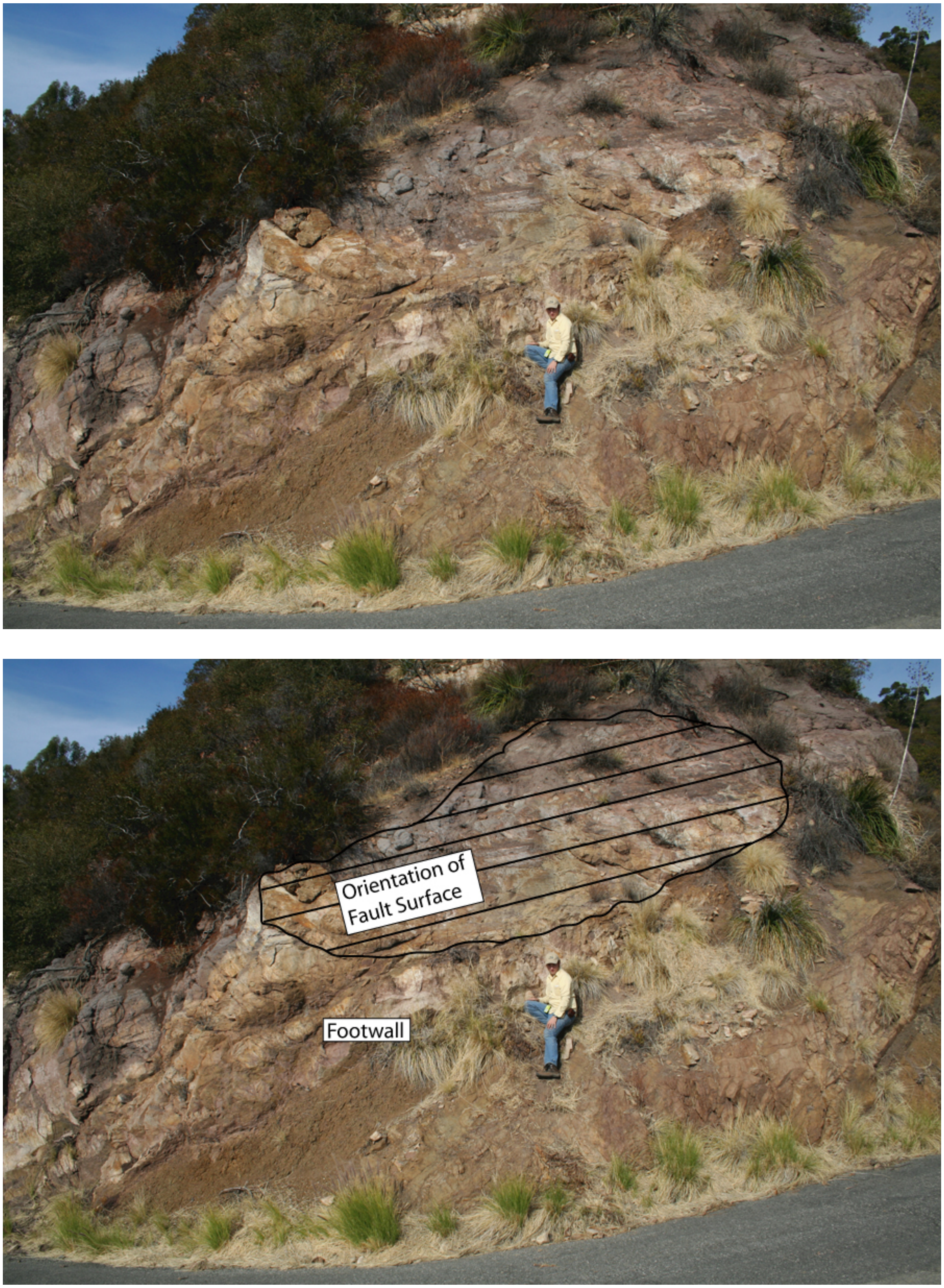

FIGURE 36.—(a) Uninterpreted and (b) interpreted photograph of Las Flores Heights 6 Fault.

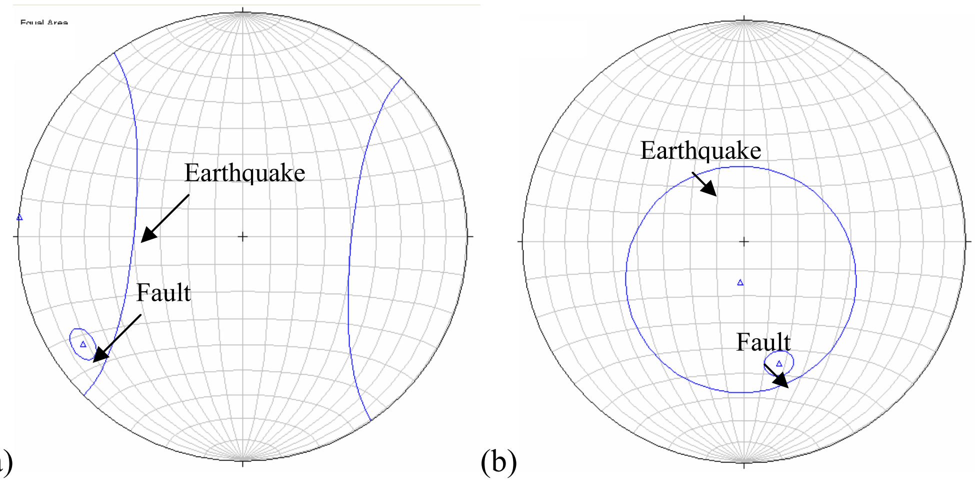

(a) (b)

FIGURE 37.—Lower hemisphere, equal area projection of data from earthquake events 20031031010718-A and the Las Flores Heights 6 Fault. Ellipses bound the 90% C.I. of (a) slip-vector, and (b) fault surface orientation, (Stereonets created using Stereonet for Windows v.1.2 by Richard Allmendinger).

movement along the fault plane parallel to the grooves (figure 38). Only the left side of the fault (foot wall) is exposed. The right side (hanging wall) is covered and contains a small drainage that has weathered out. Adjacent to the weathered area on the right side of the fault is the same conglomerate unit that is present on the left side of the fault. The damage zone that still remains after extensive weathering is 76 ± 22 cm thick and consists of moderate-brown very-highly weathered fault breccia and cataclasite composed of material from the adjacent rock, and a small zone of very highly-fractured cobbles and sandstone adjacent to the fault surface. The rock on the left side of the fault consists of moderate-brown, moderate- to poorly-sorted conglomerate with ~10% sandy matrix and clasts ranging in size from 1-20 cm. The fault does not appear to be involved in landsliding. Although the fault is located within the surface trace of one or more seismo-lineaments, the fault does not meet the other criteria and therefore is not considered potentially seismogenic.

FIGURE 38.—Photo of ~1-2 cm deep grooves in the surface of the Tuna Canyon 1 Fault which suggests significant movement along the fault.

Tuna Canyon 2 Fault

The Tuna Canyon 2 Fault is located at UTM 0351903, 3769805 on Tuna Canyon Road, directly east of the Tuna Canyon 1 Fault. The elevation of the outcrop is ~1395 ft. The fault is marked by a surface with extensive striations and a gouge zone in rocks of the Santa Susan Formation as mapped by Dibblee (1992) (figure 39). The fault has a dip azimuth of 198° ± 25° and dip angle of 87° ± 1°. Slickenlines on the surface of the fault have a trend of 286° ± 4° and plunge of 23° ± 3°. The core of the fault consists of a 14 ± 6 cm thick zone of dark yellowish-orange, medium-grained fault gouge with tree roots growing inside the zone. The damage zone on either end of the fault is ~125 cm wide and consists of extensive jointing. Rock on both sides of the fault consists of moderate

Figure 39.—(a) Uninterpreted and (b) interpreted photograph of Tuna Canyon 2 Fault.

brown, very poorly-sorted, shallow dipping conglomerate with clasts ranging from 2-45 cm in size in a sandstone matrix. The fault does not appear to be involved in landsliding.

The Tuna Canyon 2 Fault is located within the seismo-lineament swath for the 20031031010718-A event. The trend and plunge of slickenlines, and strike and dip of the fault surface fall within the range of possible orientations for the earthquake event. The fault and earthquake event are similar in spatial location, fault orientation, and slip direction, suggesting that the Tuna Canyon 2 Fault potentially seismogenic (figure 40).

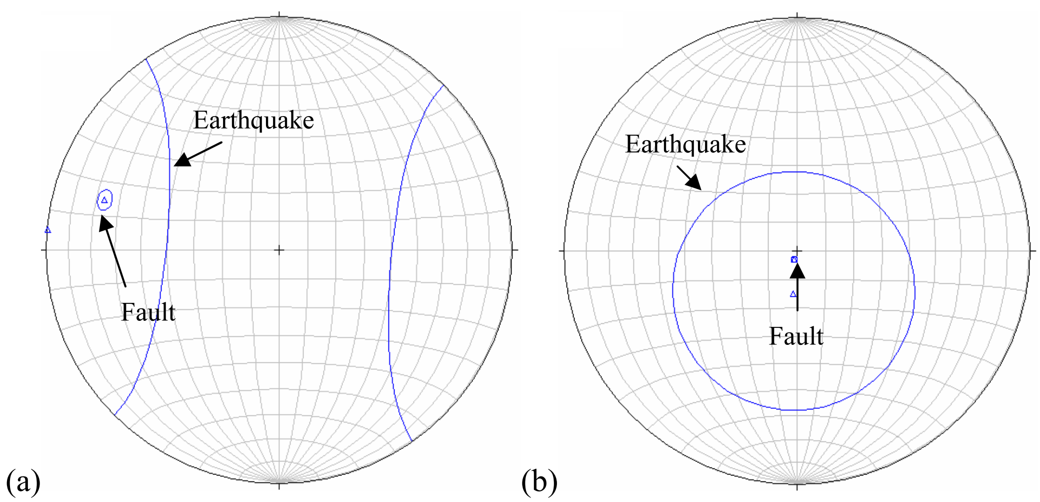

FIGURE 40.—Lower hemisphere, equal area projection of data from earthquake event 20031031010718-A and the Tuna Canyon 2 Fault. Ellipses bound the 90% C.I. of (a) slip-vector, and (b) fault surface orientation. (Stereonets created using Stereonet for Windows v.1.2 by Richard Allmendinger).

Tuna Canyon Faults 3-8

Based on their spatial location, orientation, and slip characteristics, Tuna Canyon Faults 3-8 appear to be part of the same fault zone that was mapped by Dibblee in unnamed marine strata of Late Cretaceous age (1992). Multiple joints and faults with minor displacement in the zone have similar attitudes; suggesting that slip is partitioned among multiple displacement faults.

The Tuna Canyon 3 Fault is located at UTM 0352005, 3769724 on Tuna Canyon Road. The elevation of the outcrop is ~1357 ft. The fault is marked by numerous sheared cobbles in the outcrop. The fault has a dip azimuth of 140° ± 18° and dip angle of 67° ± 7°. Slickenlines on the fault surface have a trend of 223° ± 6° and plunge of 14° ± 6°. The damage zone surrounding the fault is ~ 8 m wide, and consists of extensive jointing, and multiple small-displacement faults. Rock on both sides of the fault consists of light tan, poorly-sorted conglomerate with poorly-sorted, coarse-grained, sandstone interbeds. Adjacent to the fault is a sub-parallel fault with ~1 m vertical displacement (figure 41). The fault does not appear to be involved in landsliding.

The Tuna Canyon 3 Fault is located within the seismo-lineament swath for the 20031031010718-A event. The trend and plunge of slickenlines, and strike and dip of the fault surface fall within the range of possible orientations for the earthquake event. The fault and the earthquake event are similar in spatial location, fault orientation, and slip direction, suggesting that the fault is potentially seismogenic (figure 42).

The Tuna Canyon 4 Fault is located at UTM 0351997, 3769705, southeast of the Tuna Canyon 3 Fault. The elevation of the outcrop is ~1347 ft. The fault is marked by an abrupt vertical contact between shallow-dipping conglomerate beds (which extends west of the fault) and sandstone (which extends east of the fault) (figure 43). The fault has a dip azimuth of ~125° and dip angle of 89° ± 1°. A ~7 m damage zone is present. The right side of the fault contains numerous tightly-spaced vertical joints, and intensely-

FIGURE 41.—(a) Uninterpreted and (b) interpreted photograph of Tuna Canyon 3 Fault. Note joints that are sub-parallel to the fault.

sheared cobbles. The left side of the fault contains numerous tightly-spaced vertical joints. No measurable slickenlines are visible on the surface of the fault due to extensive weathering. Rock on the left side of the fault consists of slightly dipping, medium tan orange, medium-sorted, medium-grained sandstone. Rock on the right side of the fault is the same lithology as rock in the Tuna Canyon 3 Fault.

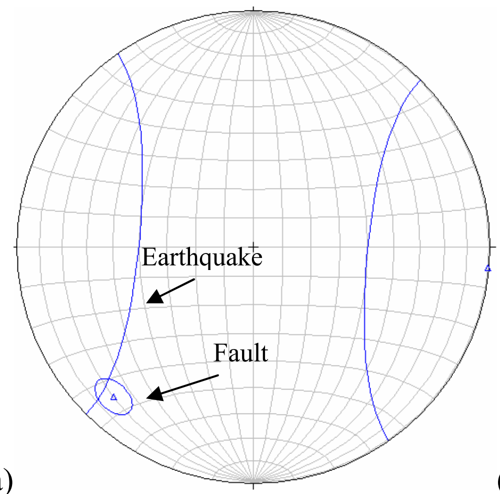

(a)

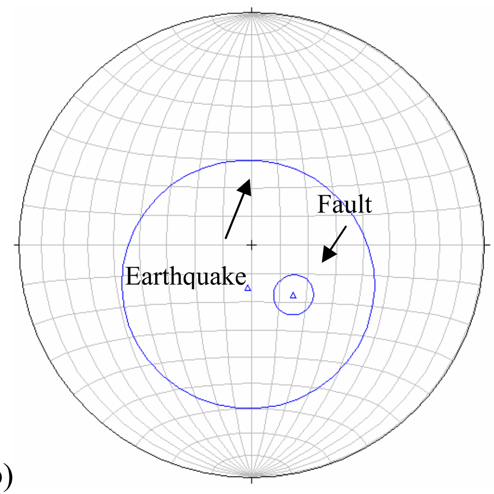

(b)

FIGURE 42.— Lower hemisphere, equal area projection of data from earthquake event 20031031010718-A and the Tuna Canyon 3 Fault. Ellipses bound the 90% C.I. of (a) slip-vector, and (b) fault surface orientation. (Stereonets created using Stereonet for Windows v.1.2 by Richard Allmendinger).

The Tuna Canyon 4 Fault is located within the seismo-lineament swath for the 20030607191-A event. The strike and dip of the fault surface fall within the range of possible orientations for the earthquake events. However, since slip-vector data was not collected, the fault does not meet the criteria and therefore cannot be considered potentially seismogenic at this time (figure 44).

The Tuna Canyon 5 Fault is located at UTM 0351997, 2769705, directly to the west of the Tuna Canyon 5 Fault. The elevation of the outcrop is ~1347 ft. The fault is marked by sheared cobbles and extensive fracturing. The fault has a dip azimuth of 320°

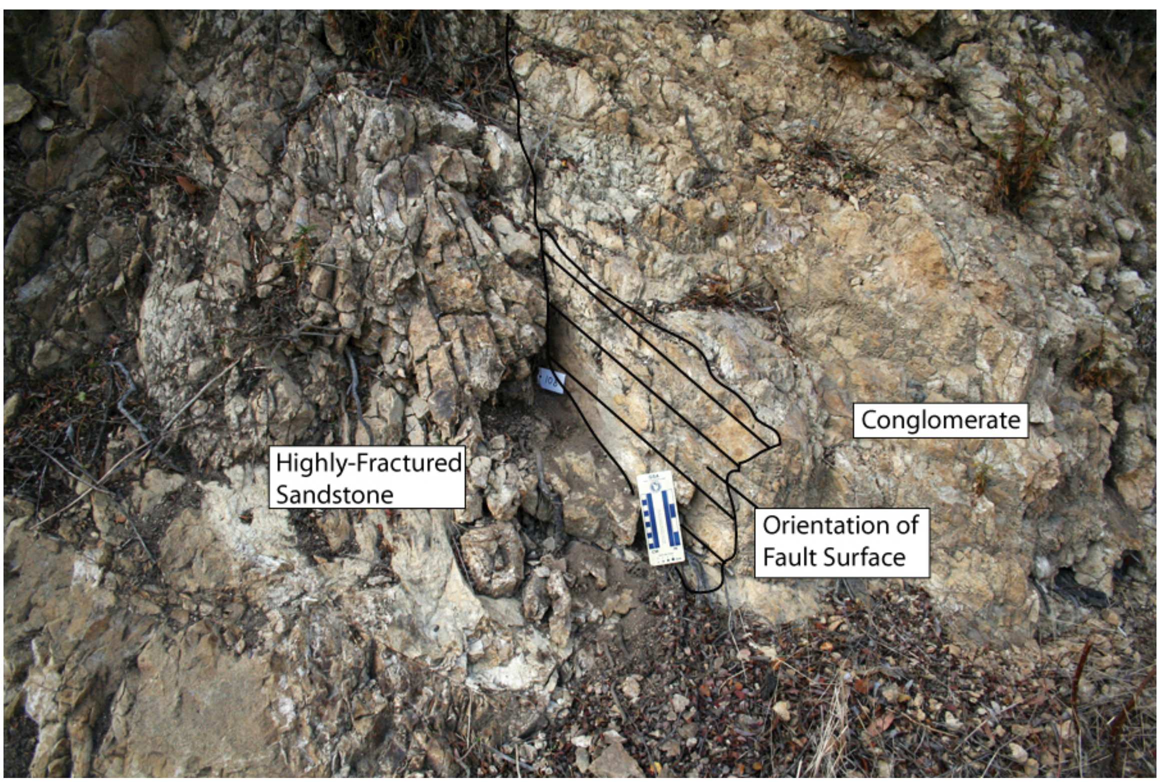

FIGURE 43.—(a) Uninterpreted and (b) interpreted photograph of Tuna Canyon 4 Fault. Note 6 inch (15.25 cm) ruler for scale.

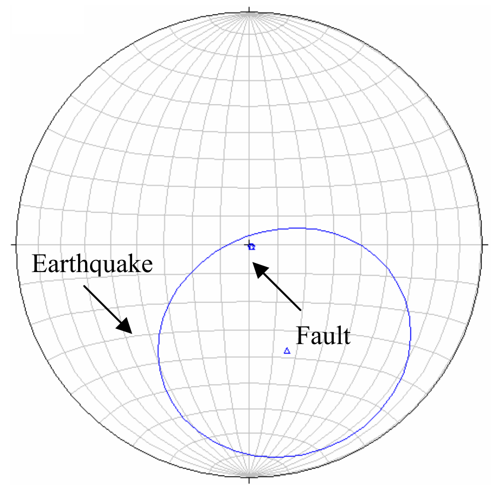

FIGURE 44.—Lower hemisphere, equal area projection of 90% C.I. of fault surface orientation data from earthquake event 20030607191-A with the Tuna Canyon 4 Fault. (Stereonets created using Stereonet for Windows v.1.2 by Richard Allmendinger).

± 12° and dip angle of 75° ± 3°. Slickenlines on the fault surface have a trend of 47° ± 5° and plunge of 11° ± 5°. Rock on both sides of the fault consists of light tan, poorly-sorted conglomerate. The fault does not appear to be involved in landsliding.

The Tuna Canyon 5 Fault is located within the seismo-lineament swath for the 20031031010718-A event. The trend and plunge of slickenlines, and strike and dip of the fault surface fall within the range of possible orientations for the earthquake event. The fault and the earthquake event are similar in spatial location, fault orientation, and slip direction, suggesting that the fault is potentially seismogenic (figure 45).

The Tuna Canyon 6 Fault is located at UTM 0352143, 3769662, on Tuna Canyon Road. The elevation of the outcrop is ~1253 ft. The fault is marked by a large, exposed surface with multiple slickenlines. The fault has a dip azimuth of 169° ± 59° and dip angle of 78° ± 11°. Slickenlines on the fault surface have a trend of 256° ± 5° and plunge of 15° ± 5°. Rock on both sides of the fault consists of shallow-dipping, light tan orange, poorly-

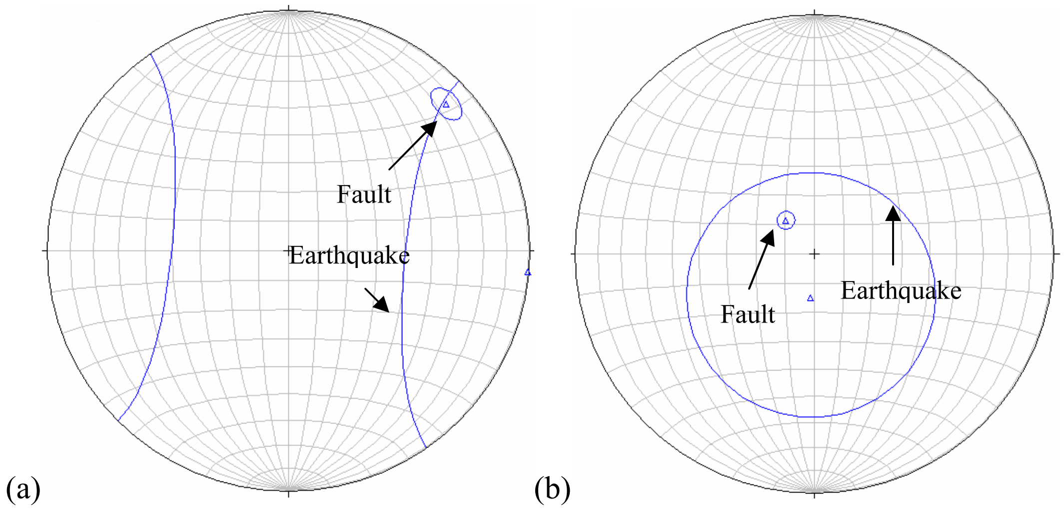

FIGURE 45.—Lower hemisphere, equal area projection of data from earthquake event 20031031010718-A and the Tuna Canyon 5 Fault. Ellipses bound the 90% C.I. of (a) slip-vector, and (b) fault surface orientation. (Stereonets created using Stereonet for Windows v.1.2 by Richard Allmendinger).

sorted, medium- to coarse-grained sandstone. Multiple vertical joints with slickenlines trend parallel to the fault (figure 46).

The Tuna Canyon 6 Fault is located within the seismo-lineament swath for the 20031031010718-A event. The trend and plunge of slickenlines, and strike and dip of the fault surface fall within the range of possible orientations for the earthquake event. The fault and the earthquake event are similar in spatial location, fault orientation, and slip direction, suggesting that the fault is potentially seismogenic (figure 47).

The Tuna Canyon 7 Fault is located at UTM 0352214, 3769673, on Tuna Canyon Road. The elevation of the outcrop is ~1283 ft. The fault is marked by a large, exposed surface with multiple slickenlines. The fault has a dip azimuth of 342° ± 21° and dip angle of 73° ± 6°. Slickenlines on the fault surface have a trend of 69° ± 4° and plunge of 9° ± 4°. Rock on both sides of the fault consists of shallow-dipping, light tan orange, poorly-sorted, medium- to coarse-grained sandstone.

FIGURE 46.—(a) Uninterpreted and (b) interpreted photograph of Tuna Canyon 6 Fault.

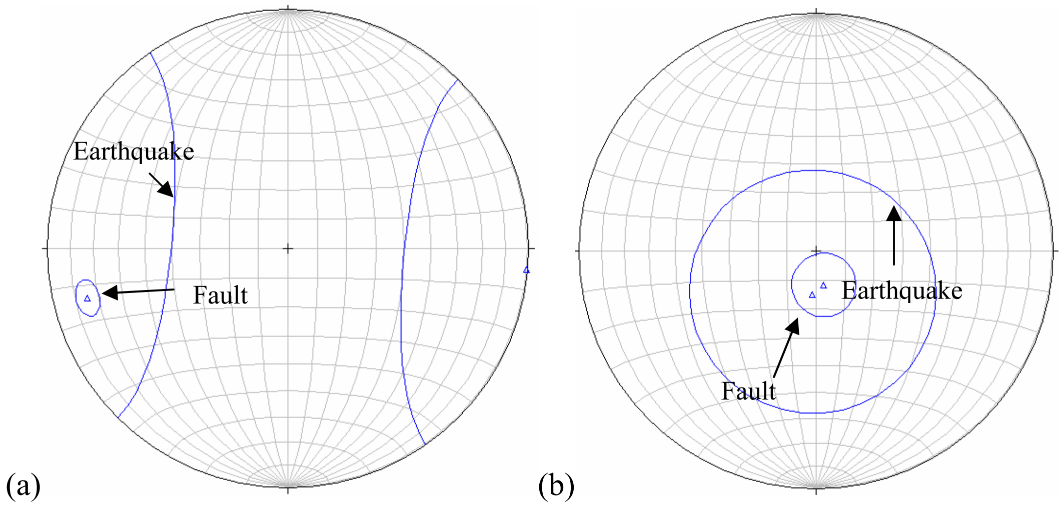

FIGURE 47.—Lower hemisphere, equal area projection of data from earthquake event 20031031010718-A and the Tuna Canyon 6 Fault. Ellipses bound the 90% C.I. of (a) slip-vector, and (b) fault surface orientation. (Stereonets created using Stereonet for Windows v.1.2 by Richard Allmendinger).

The Tuna Canyon 7 Fault is located within the seismo-lineament swath for the 20031031010718-A event. The trend and plunge of slickenlines, and strike and dip of the fault surface fall within the range of possible orientations for the earthquake event. The fault and the earthquake event are similar in spatial location, fault orientation, and slip direction, suggesting that the fault is potentially seismogenic (figure48).

The Tuna Canyon 8 Fault is located at UTM 0352175, 3769664 on Tuna Canyon Road. The elevation of the outcrop is ~1294. The fault is marked by a ~1 m wide zone of very highly sheared sandstone with fault gouge in between sandstone clasts. The fault has a dip azimuth of 148° ± 58° and dip angle of 82° ± 7°. Only one slickenline on the fault surface could be measured. It has a trend of 242° and plunge of 49°. Rock on both sides of the fault consists of shallow-dipping, light tan orange, poorly-sorted, medium- to coarse-grained sandstone. The Tuna Canyon 8 Fault is located within the seismo-lineament swath for the 20030607191-A event. The strike and dip of the fault surface fall within the range of possible orientations for the earthquake events. However, since slip-vector data was not collected, the fault does not meet the criteria and therefore cannot be considered potentially seismogenic at this time (figure 49).

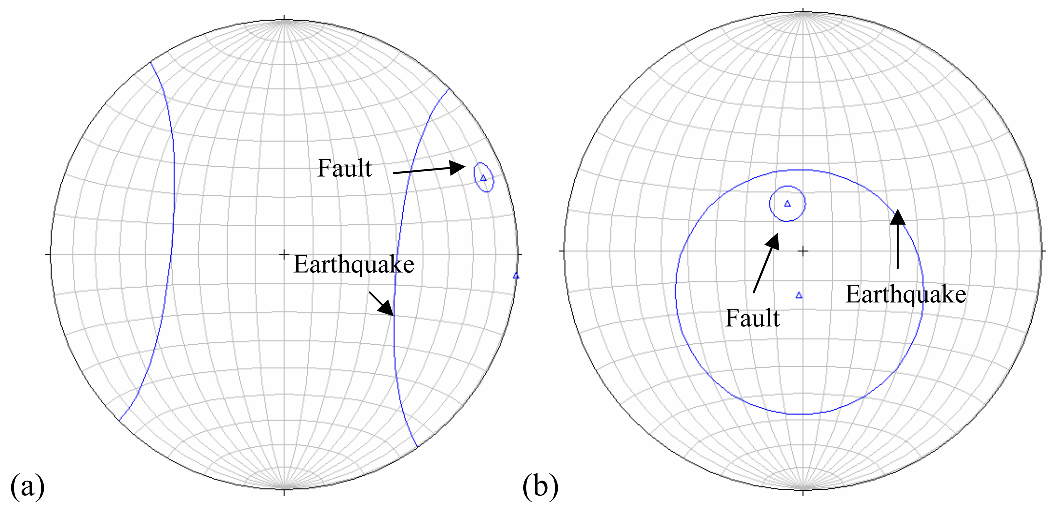

FIGURE 48.—Lower hemisphere, equal area projection of data from earthquake event 20031031010718-A and the Tuna Canyon 7 Fault. Ellipses bound the 90% C.I. of (a) slip-vector, and (b) fault surface orientation. (Stereonets created using Stereonet for Windows v.1.2 by Richard Allmendinger).

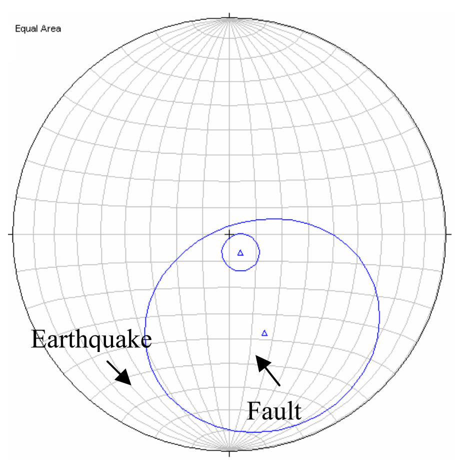

FIGURE 49.—Lower hemisphere, equal area projection of 90% C.I. of fault surface orientation data from earthquake event 20030607191-A and the Tuna Canyon 8 Fault. (Stereonets created using Stereonet for Windows v.1.2 by Richard Allmendinger).

Old Topanga Canyon 1 Fault

Old Topanga Canyon 1 Fault is located at UTM 0350735, 3774257 on Old Topanga Canyon Road, northwest of Topanga. The elevation of the outcrop is ~858 ft. The fault is marked by offset conglomerate beds of the Lower Topanga Formation as mapped by Dibblee (1992). The fault has a dip azimuth of 91° ± 5° and dip angle of 49° ± 3°. Slickenlines on the surface of the fault have a trend of 168° ± 4° and plunge of 15° ± 4°. The fault is a "credit card" fault with minor calcite mineralization on the surface and very minor jointing on both sides of the fault (figure 50). Rock on both sides of the fault consists of shallow dipping, yellowish gray, very coarse, poorly sorted sandstone with ~1 m thick, poorly-sorted, conglomerate interbeds. The fault appears to have at least 2 m vertical displacement, evidenced by a thick conglomerate bed in the footwall that is not present in the hanging wall. Approximately 3-4 m above the road, a small 1-2 m deep cave has formed, likely a result of preferential weathering along the fault surface.

FIGURE 50.—Sub-horizontal slickenlines evidenced on the surface of the Old Topanga Canyon 1 Fault.

The Old Topanga Canyon 1 Fault is within ~110 m of the surface trace of a fault mapped by Dibblee (1992) and is likely part of the same fault zone. Although the fault is located within the surface trace of seismo-lineaments examined in the study, the fault does not meet the other criteria and therefore is not considered potentially seismogenic.

Topanga Canyon 1 Fault

The Topanga Canyon 1 Fault is located at UTM 0352715, 3772136 on Topanga Canyon Road, at the southern end of the City of Topanga. The elevation of the outcrop is ~743 ft. The fault is marked by offset conglomerate beds of the Lower Topanga Formation as mapped by Dibblee (1992). The fault has a dip azimuth of 119° ± 17° and dip angle of 65° ± 7°. Slickenlines on the surface of the fault have a trend of 198° ± 6° and plunge of 21° ± 6°. The fault rock is 11 ± 6 cm wide and consists of dark yellowish orange cataclasite. Rock on both sides of the fault consists of dark yellowish orange, very-coarse, poorly-sorted, poorly-cemented sandstone with 0.25 – 2 m thick poorly sorted conglomerate interbeds. Directly to the right of the fault is a second fault with approximately the same orientation. It has a dip azimuth of 124° ± 15° and dip angle of 56° ± 8°. Only one slickenline was measured on the surface, trending 197° and plunging 31°, similar to that of Topanga Canyon 1 Fault. The two faults are on a large cliff face, and are directly adjacent to a large drainage to the north. Based on correlation of conglomerate beds and similar slip vector orientations, it appears that the left fault is a high-angle reverse fault, while the right fault is a normal fault "pinching" out the slab in between the fault, similar to a seed being pinched between two fingers (figure 51).

The Topanga Canyon 1 Fault has been previously mapped by Dibblee (1992). Although the Topanga Canyon 1 Fault is located within the surface trace of one or more

FIGURE 51.—(a) Uninterpreted and (b) interpreted photograph of Topanga Canyon 1 Fault.

seismo-lineaments examined in the study, the fault does not meet the other criteria and therefore is not considered potentially seismogenic.

Topanga Canyon 2 Fault

The Topanga Canyon 2 Fault is located at UTM 0353145, 3771626 on Topanga Canyon Road, south of Topanga. The elevation of the outcrop is ~689 ft. The fault is marked by a large surface in the roadcut with extensive slickenlines (figure 52). The fault is in rocks of the Lower Topanga Canyon Formations as mapped by Dibblee (1992) and has a dip azimuth of 11° ± 12° and dip angle of 72° ± 4°. The surface of the fault has a trend of 324° ± 8° and plunge of 63° ± 3°. Slickenfibers on the surface of the fault suggest that the hanging wall moved down relative to the footwall. Rock on either end of the fault consists of grayish red purple, poorly-sorted, coarse sandstone conglomerate with moderate jointing that extends for ~0.5 m on both sides of the fault. The fault is not likely the result of road construction because slickenlines extend to the base of the roadcut. Within ~7 m of the fault on either side, numerous joints and very small displacement faults have approximately the same orientation as the Topanga Canyon 2 Fault. Across the road from the fault, a small roadcut has a fault surface with a dip azimuth of 22° ± 21° and dip angle of 73° ± 6°. The surface of the fault has a trend of 74° ± 24° and plunge of 64° ± 10°. Directly adjacent to the fault surface is a slight geomorphic slope that is potentially related to the fault.

The Topanga Canyon 2 Fault is located within the seismo-lineament swath for the 20010806090-A and 20021014013-A events. The fault and the earthquake events are similar in spatial location, fault orientation, and slip direction, suggesting that the fault is potentially seismogenic (figure 53).

FIGURE 52.—(a) Uninterpreted and (b) interpreted photograph of Topanga Canyon 2 Fault.

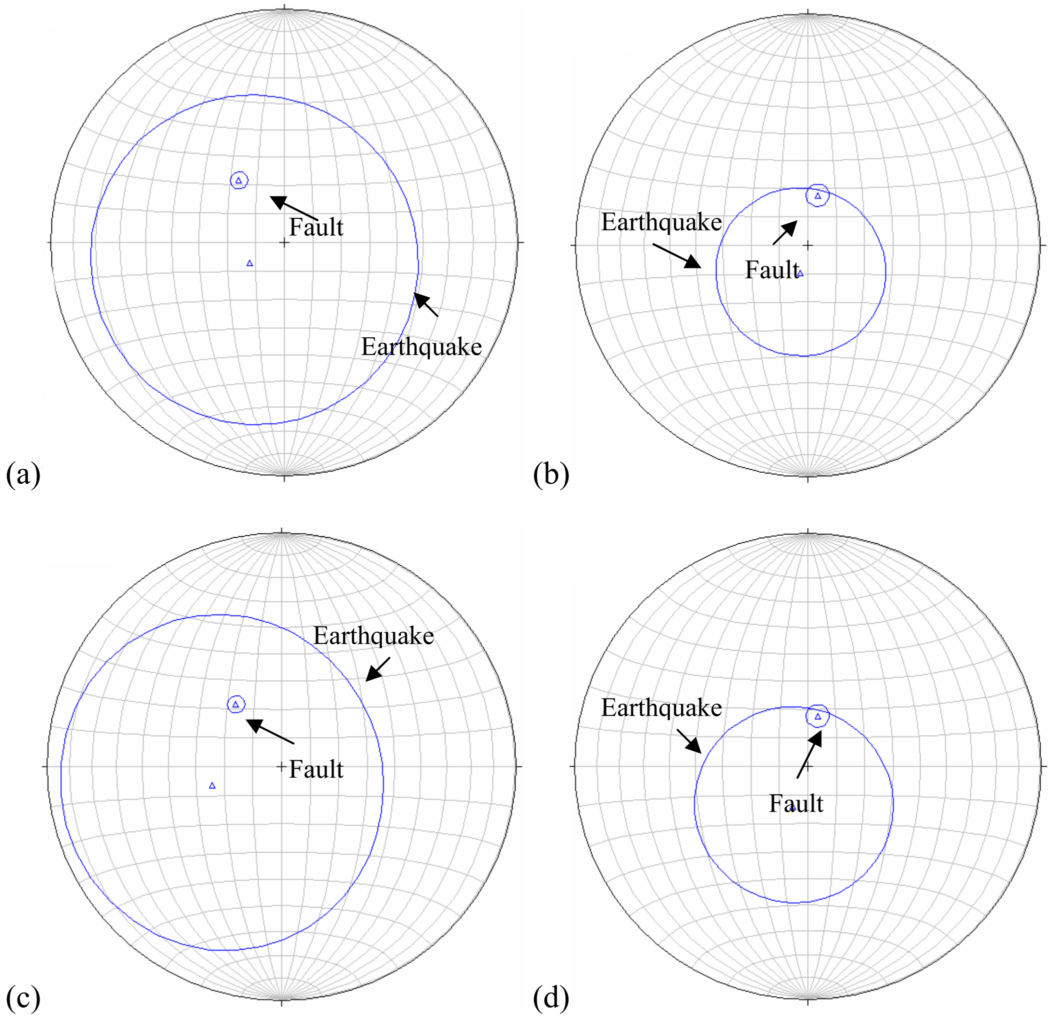

FIGURE 53.—Lower hemisphere, equal area projection of data from earthquake events 20010806090-A and 20021014013-A and the Topanga Canyon 2 Fault. Ellipses bound the 90% C.I. of (a) slip-vector, (b) fault surface, (c) slip-vector, and (d) fault surface orientations. (Stereonets created using Stereonet for Windows v.1.2 by Richard Allmendinger).

Topanga Canyon 3 Fault

The Topanga Canyon 3 Fault is located at UTM 0353095, 3771673 on Topanga Canyon road, south of Topanga. The elevation of the outcrop is ~697 ft. The fault is located along the left edge of a 2-3 m wide sub-vertical igneous dike interpreted as being of Middle Miocene age by Dibblee (1992) (figure 54). The fault is marked by highly-

FIGURE 54.—(a) Uninterpreted and (b) interpreted photograph of Topanga Canyon 3 and 4 Faults.

sheared igneous rock focused along a surface with multiple slickenlines. The fault has a dip azimuth of 186° ± 48° and dip angle of 75° ± 11°. Slickenlines on the fault surface have a trend of ~185° ± and plunge of 79° ± 13°. The fault core is a 9 ± 1 cm wide zone of dark yellowish brown, highly-sheared breccia fragments in a matrix of silt-sized fault gouge. The breccia fragments have multiple slickenlines, suggesting extensive shearing. Rock on the left side of the fault (hanging wall) consists of shallow-dipping, moderately fractured, very-coarse, poorly-sorted sandstone conglomerate of the Lower Topanga Formation as mapped by Dibblee (1992). Rock on the right side of the fault (footwall) consists of highly-sheared igneous rock. The fault is directly adjacent to a small drainage that is likely related to faulting.

The Topanga Canyon 3 Fault is located within the seismo-lineament swath for the 20010806090-A and 20021014013-A events. The fault and the earthquake events are similar in spatial location, fault orientation, and slip direction, suggesting that the fault is potentially seismogenic (figures 55).

Topanga Canyon 4 Fault

The Topanga Canyon 4 Fault is located at UTM 0353111, 3771661 on Topanga Canyon Road, ~10 m southeast of the Topanga Canyon 3 Fault. The elevation of the outcrop is ~717 ft. The fault is marked by offset conglomerate beds and slickenlines along the fault surface in rocks of the Lower Topanga Formation (figure 54, Dibblee, 1992). The fault has a dip azimuth of ~66° and dip angle of 89° ± 7°. Slickenlines on the fault surface have a trend of 81° ± 13° and plunge of 61° ± 6°. The fault core consists of sheared cobbles in a coarse silt matrix. The damage zone is ~2-3 m wide and consists of moderate, sub-parallel fractures. Rock on both sides of the fault consists of poorly-

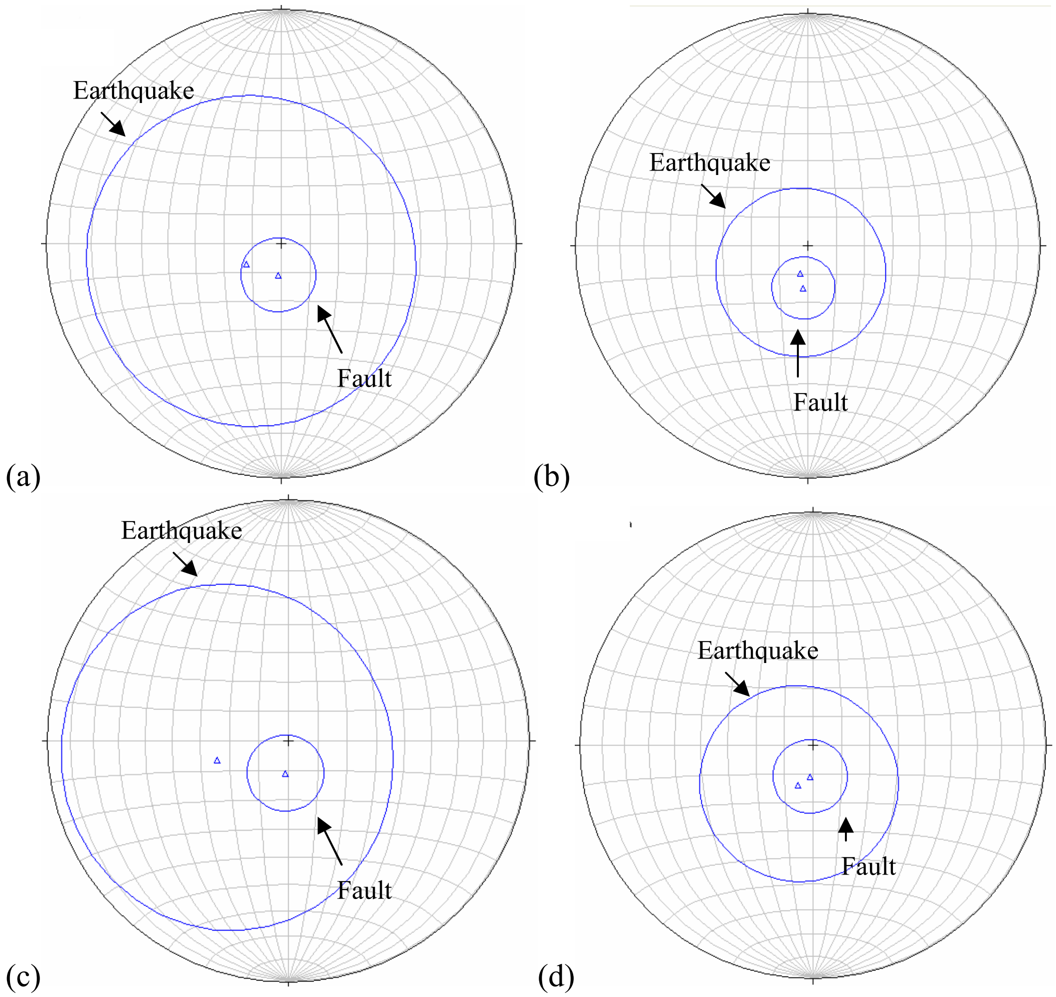

FIGURE 55.—Lower hemisphere, equal area projection of data from earthquake events 20010806090-A and 20021014013-A and the Topanga Canyon 3 Fault. Ellipses bound the 90% C.I. of (a) slip-vector, (b) fault surface, (c) slip-vector, and (d) fault surface orientations. (Stereonets created using Stereonet for Windows v.1.2 by Richard Allmendinger).

sorted, very coarse, sandstone conglomerate. The fault does not appear to be related to landslide development.

The Topanga Canyon 4 Fault is located within the seismo-lineament swath for the 20010806090-A and 20021014013-A events. The fault and the earthquake events are similar in spatial location, fault orientation, and slip direction, suggesting that the fault is potentially seismogenic (figure 56).

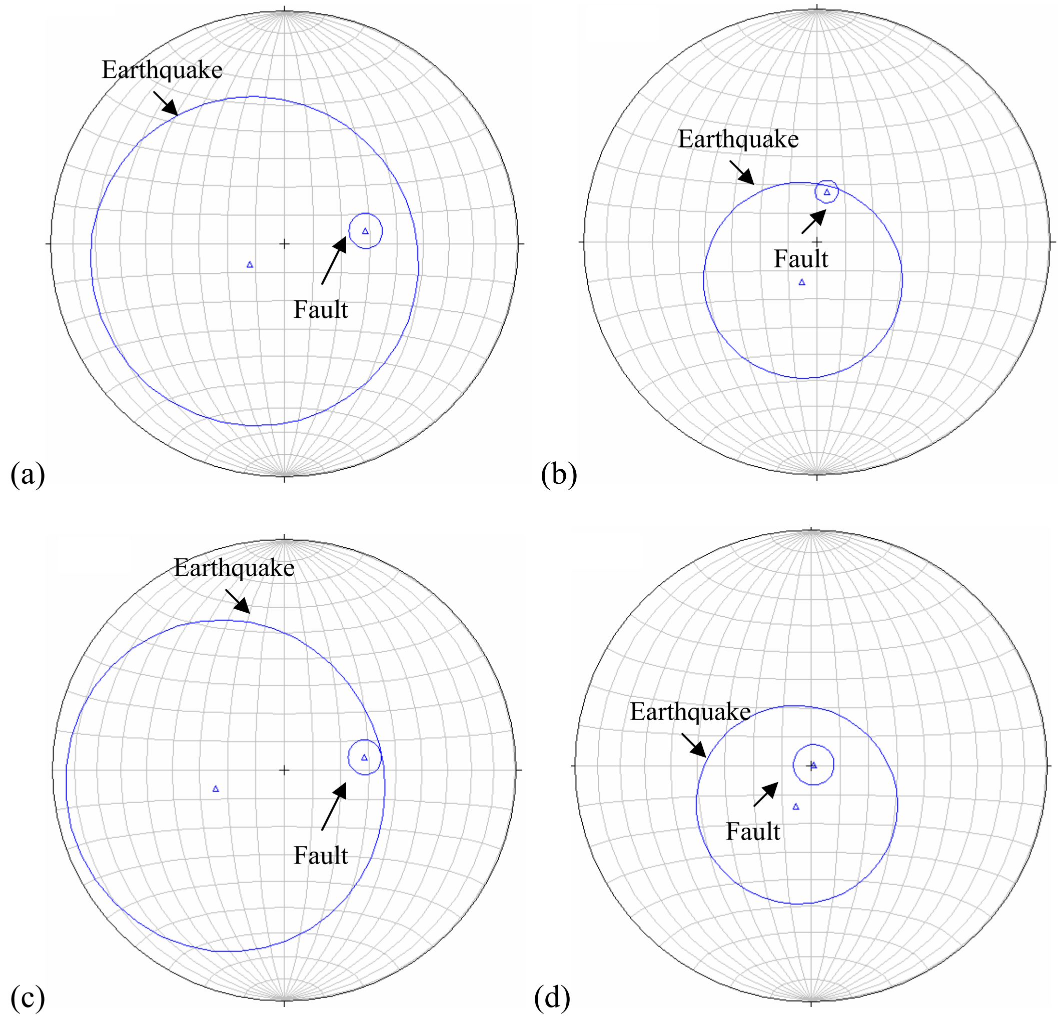

FIGURE 56.—Lower hemisphere, equal area projection of data from earthquake events 20010806090-A and 20021014013-A, and the Topanga Canyon 4 Fault. Ellipses bound the 90% C.I. of (a) slip-vector, and (b) fault surface orientations. (Stereonets created using Stereonet for Windows v.1.2 by Richard Allmendinger).

Topanga Canyon 5 Fault

The Topanga Canyon 5 Fault is located at UTM 35095, 3771673, on Topanga Canyon Road. The elevation of the outcrop is ~697 ft. The fault surface is along the left side of a 3-4 m wide, sub-vertical igneous dike interpreted by Dibblee (1992) as Middle Miocene in age (figure 57). The fault has a dip azimuth of 337° ± 4° and dip angle of 57°

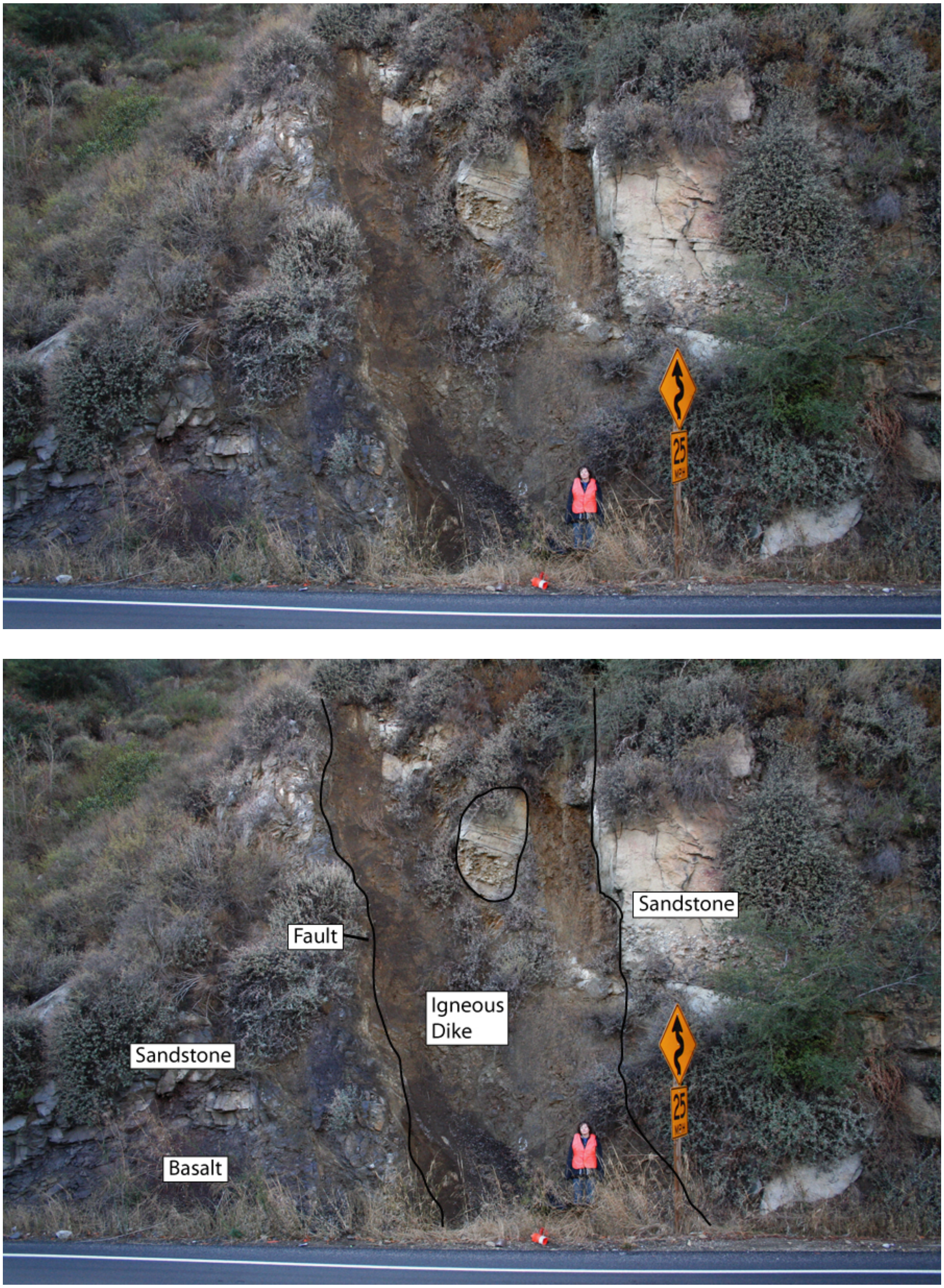

FIGURE 57.—(a) Uninterpreted and (b) interpreted photograph of Topanga Canyon 5 Fault.

± 2°. Slickenlines along the fault surface have a trend of 45° ± 9° and plunge of 31° ± 8°. The fault core consists of dusky yellowish-brown highly-sheared volcanic rock and metaconglomerate. The metaconglomerate along the edge of the fault core contains slickenlines on multiple surfaces, suggesting that slip occurred after the dike had become emplaced, metamorphosing the rock.

The damage zone is ~7 m and consists of multiple fractures. Rock on the left side of the fault (footwall) consists of shallow dipping, highly fractured, dark-purple to black basalt, poorly-sorted, very coarse-grained sandstone with conglomerate interbeds, metaconglomerate, and quartzite in rocks of the Lower Topanga Formation and Conejo Volcanics as mapped by Dibblee (1992). Rock on the right side of the fault (hanging wall) consists of dusky yellowish-brown, highly-sheared, highly weathered, igneous rock with slickenlines on multiple surfaces. The fault does not appear to be involved in landsliding. Although the Topanga Canyon 5 Fault is located within the surface trace of one or more seismo-lineaments examined in the study, the fault does not meet the other criteria and therefore is not considered potentially seismogenic.

Trippet Ranch 1 Fault

The Trippet Ranch 1 Fault is located at UTM 0354989, 3774582 at the Eagle Rock Junction on the Trippet Ranch Fire Road. The elevation of the outcrop is ~1653 ft. The fault is marked by a highly fractured zone with slickenlines on multiple surfaces in rocks of the Lower Topanga Formation as mapped by Dibblee (1992). The fault has a dip azimuth of 300° ± 20° and dip angle of 72° ± 6°. Slickenlines on the surface of the fault have a trend of 19° ± 6° and plunge of 23° ± 5°. Only the footwall of

FIGURE 58.—(a) Uninterpreted and (b) interpreted photograph of the Trippet Ranch 1 Fault. Only portions of the fault surface are exposed.

the fault is exposed due to construction of the fire road (figure 58). The fault core consists of dark yellowish orange, fine-grained, highly fractured, brittle cataclasite.

Rock in the footwall is dark yellowish orange, very coarse-grained, very poorly-sorted, highly fractured sandstone. The fault does not appear to be caused by road construction . The fault aligns with numerous sub-parallel fractures in an outcrop north of the fault. Although the fault is located within the surface trace of one or more seismo-lineaments examined in the study, the fault does not meet the other criteria and therefore is not considered potentially seismogenic.

Trippet Ranch 2 Fault

The Trippet Ranch 2 Fault is located at UTM 0355 083, 3774646, north of the Eagle Rock Junction on the Trippet Ranch Fire Road. The elevation of the outcrop is ~1691 ft. The fault is evidenced by a highly fractured zone with slickenlines on multiple surfaces in rocks of the Lower Topanga Formation as mapped by Dibblee (1992). The fault has a dip azimuth of 152° ± 11° and dip angle of 60° ± 6°. Slickenlines have a trend of 216° ± 11° and plunge of 37° ± 9°. Only the footwall of the fault is exposed due to growth of vegetation. Fault rock in the outcrop is dark yellowish orange, medium-grained, highly fractured, cataclasite. Rock in the footwall consists of dark yellowish orange, very coarse-grained, very poorly-sorted, highly fractured sandstone. Steps on the surface of the fault suggest that the hanging wall moved down relative to the footwall (figure 59). Numerous fault surfaces with similar orientations are located within the vicinity of the fault, but are inaccessible because of their height above the road. The fault does not appear to be a result of landsliding or road construction. The fault is on the published map of the Topanga 7.5’ Quadrangle by Yerkes and Campbell (1997).

FIGURE 59.—Steps on the surface of the Trippet Ranch 2 Fault suggest that the footwall (shown) was upthrown.

The fault is located within the seismo-lineament swath for the 2000031906-B and 20030328054-A events. The trend and plunge of slickenlines, and strike and dip of the fault surface fall within the range of possible orientations for the earthquake events. The Trippet Ranch 2 Fault and the earthquake events are similar in spatial location, fault orientation, and slip direction, suggesting that the Trippet Ranch 2 Fault is potentially seismogenic (figure 60).

Offshore Data

The interpretation of possible offshore connections of the Santa Monica Fault and Malibu Coast Fault Zone was based on topographic trends in the bedrock surface, zones denuded of Holocene sediment, and alignment of gas seeps. Five possible fault locations were interpreted in the offshore portion of the study area (figure 61).

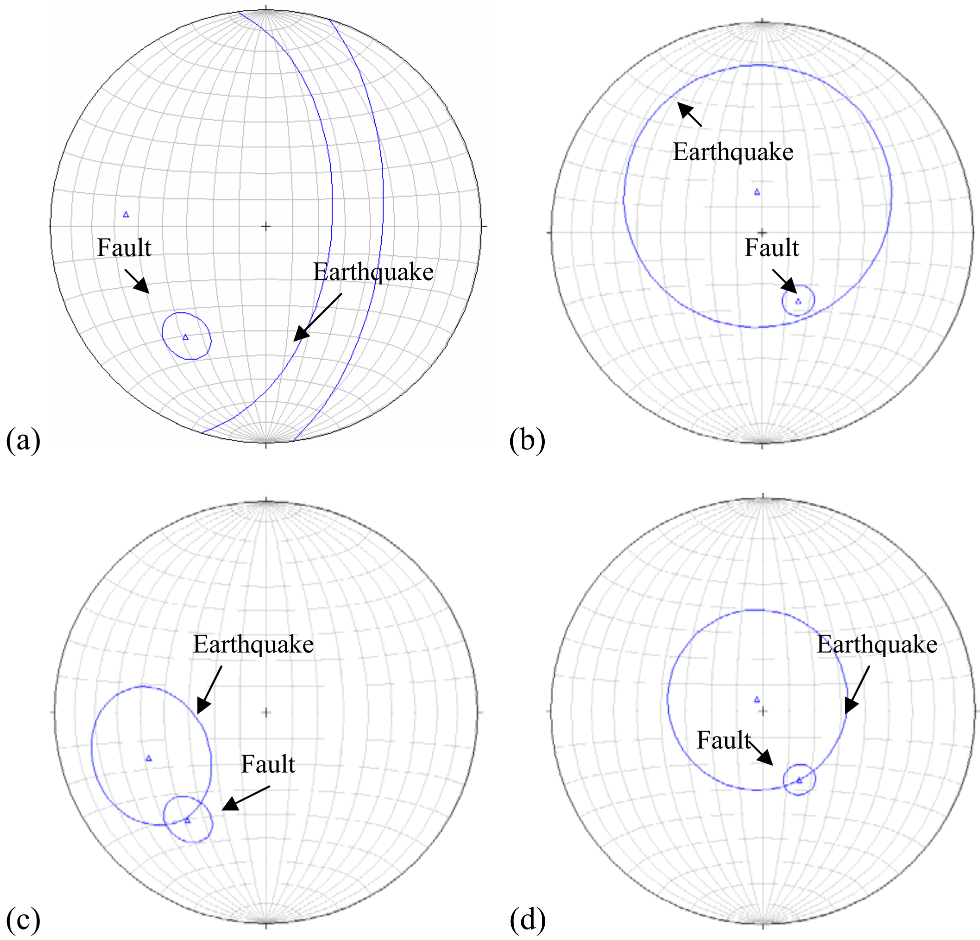

FIGURE 60.—Lower hemisphere, equal area projection of data from earthquake events 2000031906-B and 20030328054-A, and the Trippet Ranch 2 Fault. Ellipses bound the 90% C.I. of (a) slip-vector, (b) fault surface orientations, (c) slip-vector, and (d) fault surface orientations (Stereonets created using Stereonet for Windows v.1.2 by Richard Allmendinger).

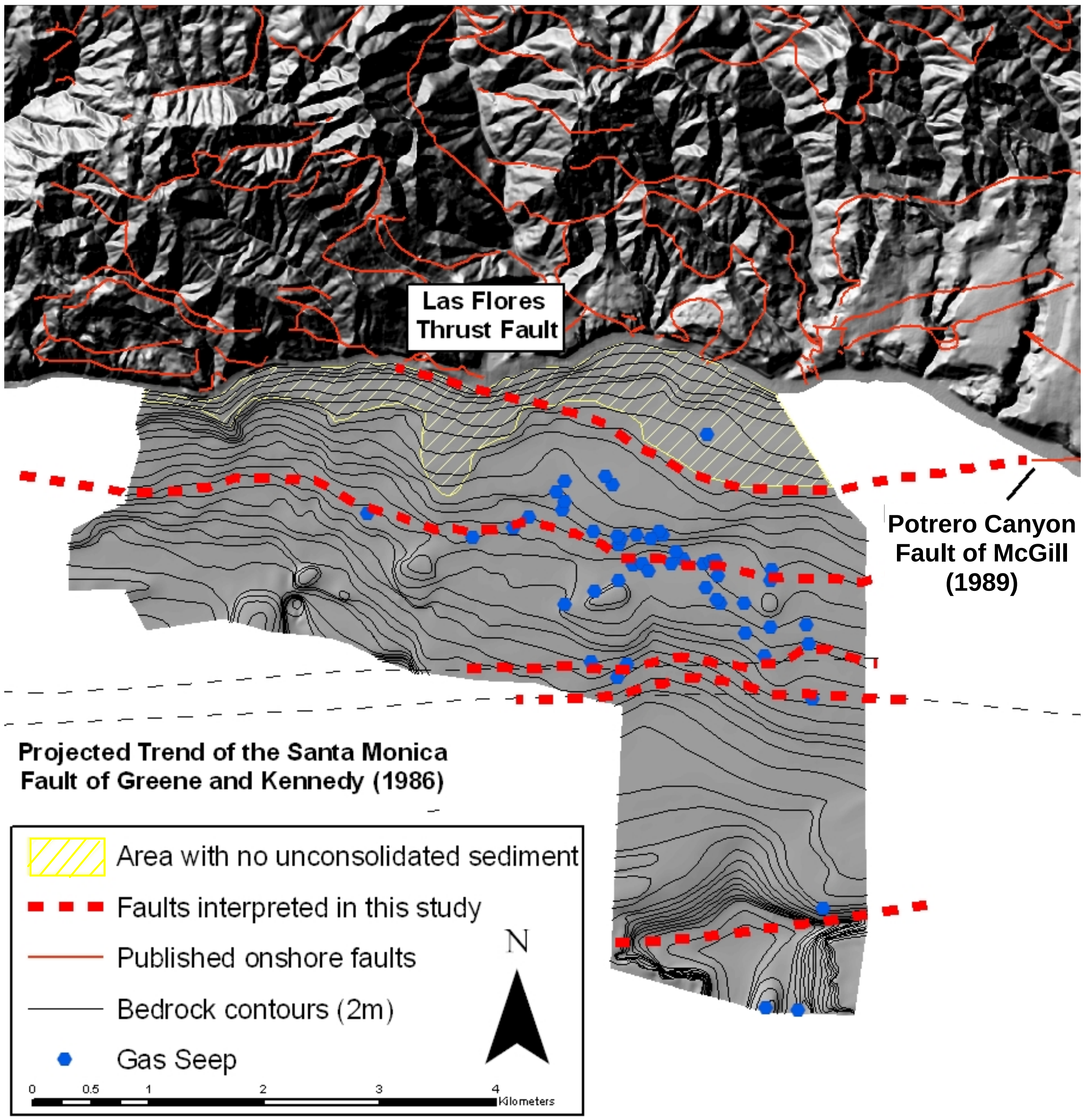

FIGURE 61.—Interpretation of faults in the Santa Monica Bay.

CHAPTER FIVE

Discussion and Conclusions

Onshore Faults

Faults at eleven locations were identified as “potentially seismogenic” in the Topanga 7.5’ Quadrangle. Many of the faults correlate with more than one seismo-lineament, suggesting the possibility of some interesting interactions between seismogenic faults (figure 62).

In recent studies conducted in the Point Dume and Malibu Beach Quadrangles to the west of the study area, Bayliss (2006) and Seidman and Cronin (2006) identified a previously unmapped, left-lateral strike-slip fault that correlates with the 20031031010718-A event and extends east through the Santa Monica Mountains. Bayliss (2006) suggests that the Santa Monica Mountains are in a zone of oblique convergence in which “strain is partitioned between thrusting along the Malibu Coast Fault Zone (Malibu Coast fault, Anacapa-Dume Faults) and strike-slip displacement along the newly identified fault.” Legg and others (2004) proposed a similar model of strain partitioning along a thrust fault and strike-slip fault in the Channel Islands, west of the Santa Monica Mountains (figure 63).

Bayliss (2006) suggests that the model by Legg and others (2004) may be applicable to the east along the Santa Monica Mountains. The Las Flores Heights 1 and 6, and Tuna Canyon 2, 3, 6, and 7 Faults, correlate with the 20031031010718-A strike-slip event. The Las Flores Heights 6 and Tuna Canyon 2, 3, 6, and 7 Faults strongly

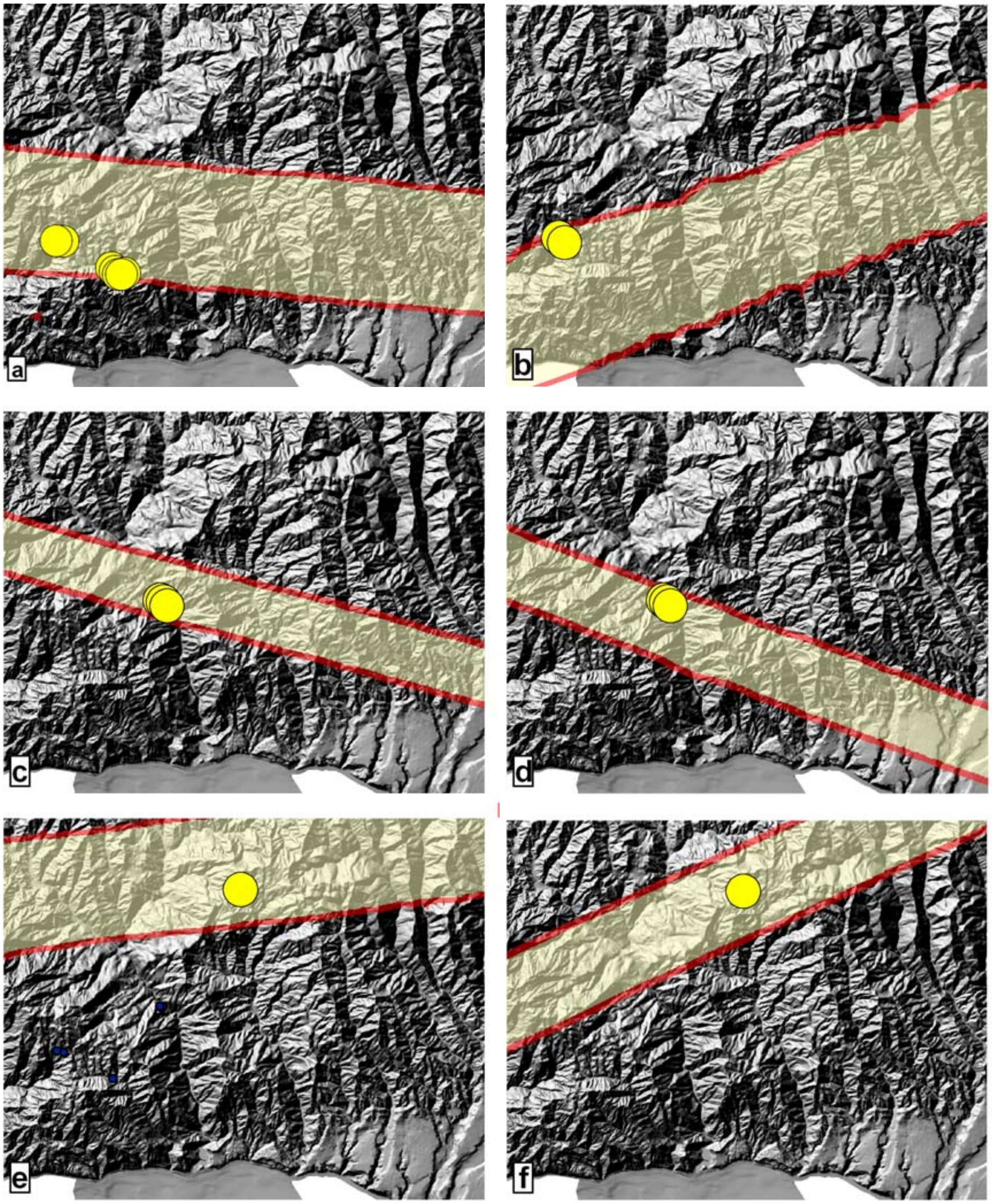

FIGURE 62.—Faults with similar fault surface orientation and slip characteristics as the (a) 20031031010718-A, (b) 20030607191-A, (c) 2001080609-A, (d) 20021014013-A (e) 2000031906-B, (f) 20030328054-A events.

correlate with the earthquake event; however, the Las Flores Heights 1 Fault only correlates due to the large error associated with the focal mechanism solution. The presence of the newly identified faults suggests that the left-lateral strike-slip fault of Bayliss (2006) extends east into the Topanga 7.5' Quadrangle (figure 64).

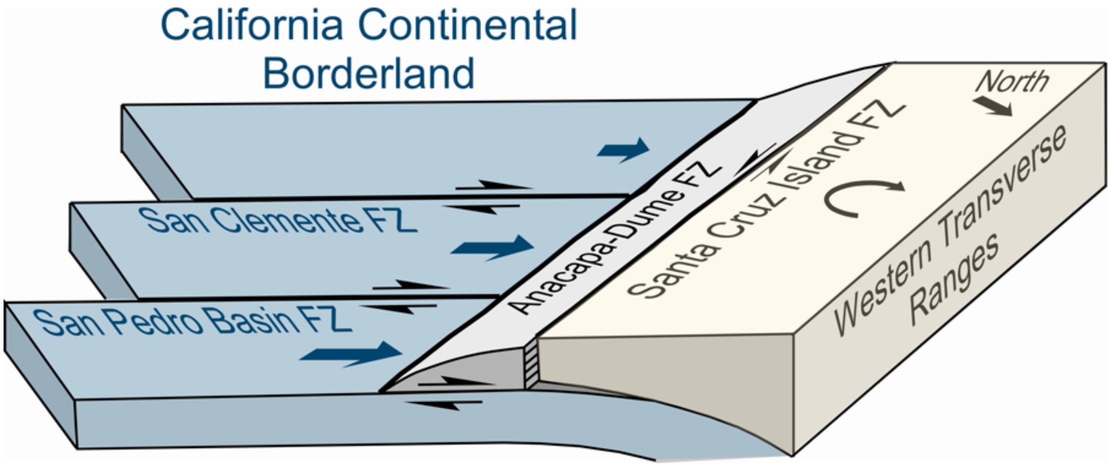

FIGURE 63.—Strain partitioning model proposed for the Channel Islands. Data suggest that this model may apply for the Santa Monica Mountains, modified from Legg and others (2004).

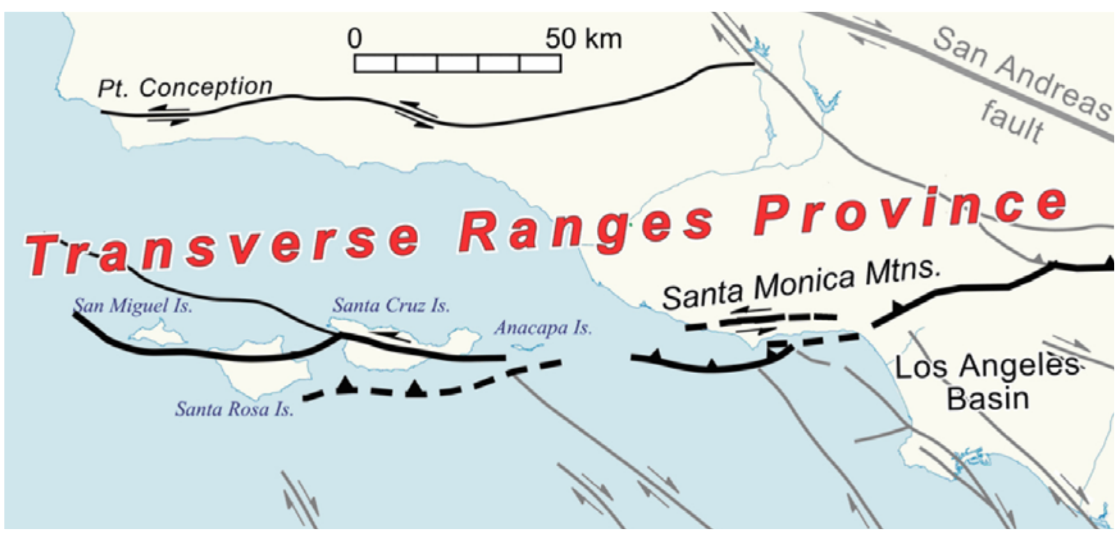

FIGURE 64.—The proposed strain partitioning model of Legg and others (2004) likely extends east into the Santa Monica Mountains.

The Las Flores Heights 1 and 3 Faults correlate with the 20030607191-A event which strikes northeast and has a normal-oblique component of slip. However, due to the large error associated with the focal mechanism solution the validity of the correlations is unable to be determined. The Topanga 2, 3, and 4 Faults correlate with the 20021014013-A and 2001080609-A events which strike east-southeast and have a reverse-oblique component of slip. The Trippet Ranch 2 Fault correlates with the 200031906-B and 20030328054-A events which strike east-northeast and have a normal-oblique component of slip. The identification of potentially seismogenic faults in this study suggests that the active tectonics of the Santa Monica Mountains is more complex than previously assumed.

Potential relationships between events with similar fault plane surface orientations and slip-characteristics exist within the dataset (figure 65). Overlapping sub-parallel seismo-lineaments could be the result of two earthquake events occurring along the same fault plane, or strain being distributed along multiple faults. Sub-parallel seismo-lineaments that do not overlap could provide evidence of strain being distributed along multiple faults.

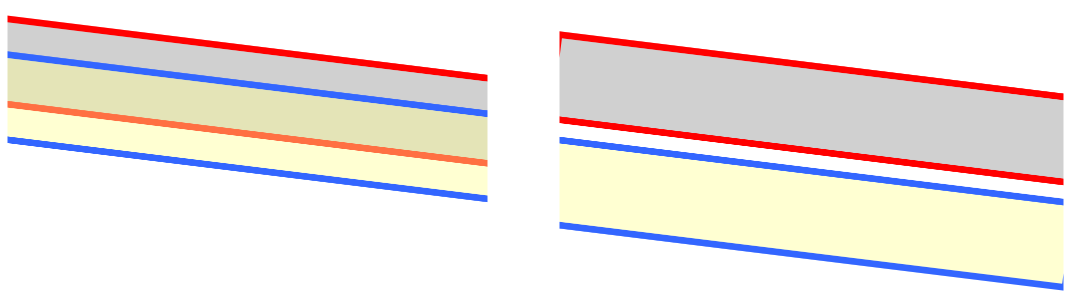

FIGURE 65.—Potential relationships between events with similar orientation and slip characteristics. (a) Sub-parallel seismo-lineaments with overlap, and (b) sub-parallel seismo-lineaments without overlap.

The 2001080609-A, and 20021014013-A events both display reverse-oblique motion along southwest dipping fault planes with overlapping seismo-lineament swaths. The two events correlate with the Topanga 2, 3, and 4 Faults and indicate the possibility that strain is being accommodated through reverse-oblique motion occurring along the same fault plane, or distributed along multiple faults (figure 66).

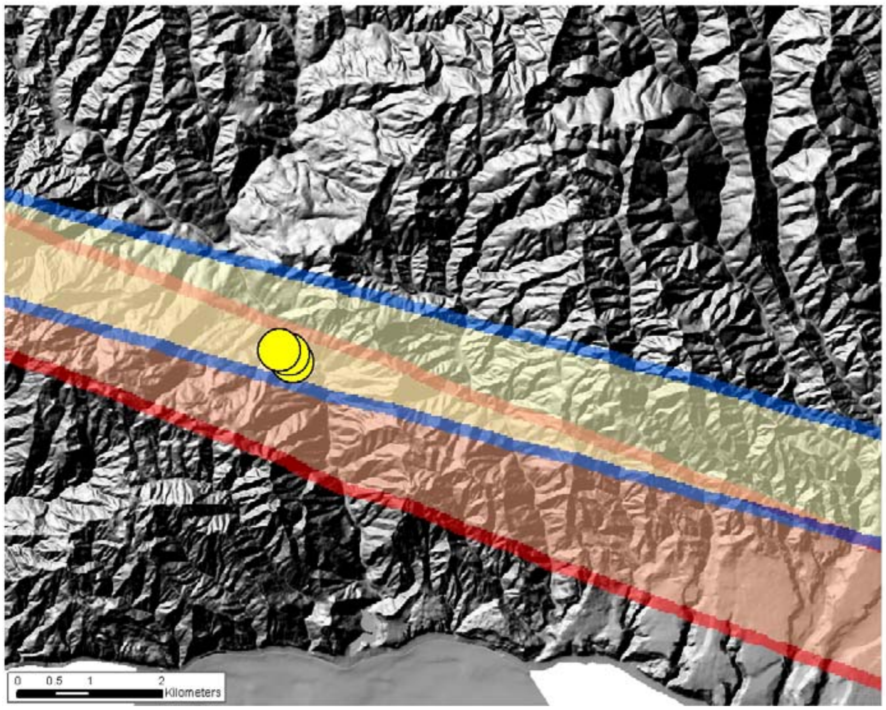

FIGURE 66.—Example of sub-parallel seismo-lineaments with overlap (red polygon – seismo-lineament for the 20021014013-A event, yellow polygon – seismo-lineament for the 2001080609-A event, and yellow dots – faults that correlate with the events.)

The 20030607191-A, and 20030328054-A events both display normal-oblique motion along northeast dipping fault planes without overlap of seismo-lineament swaths. The two events correlate with faults identified in the field and indicate the possibility that strain is being accommodated through normal-oblique motion occurring multiple seismogenic faults (figure 67).

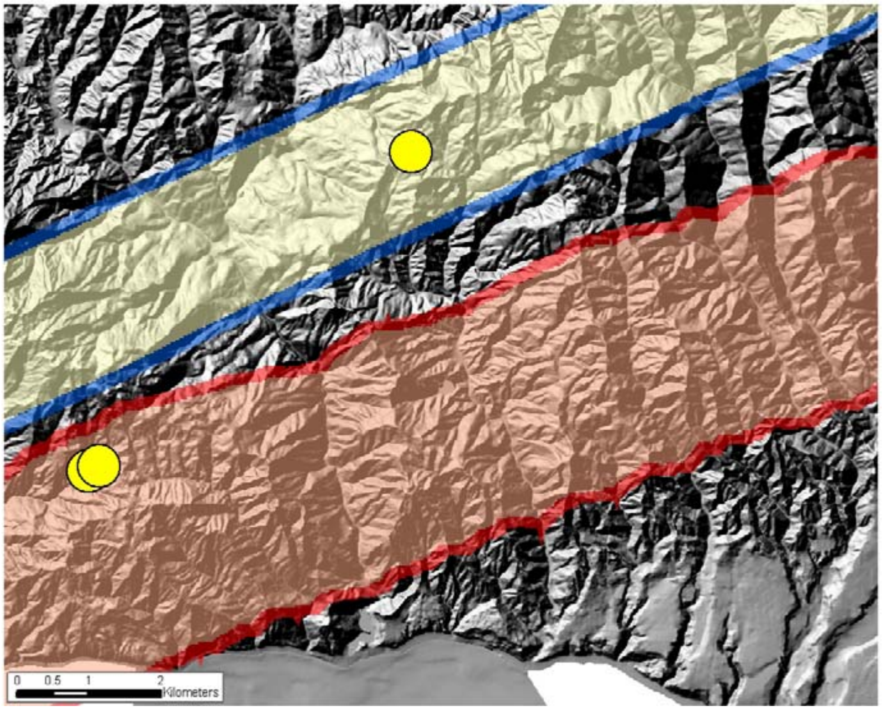

FIGURE 67.—Example of sub-parallel seismo-lineaments without overlap (red polygon – seismo-lineament for the 20030607191-A event, yellow polygon – seismo-lineament for the 20030328054-A event, and yellow dots – faults that correlate with the events).

Seismo-Lineament Analysis

In order to project a fault plane from a focal mechanism solution to the surface of a DEM, an assumption is made that the fault being projected is planar. Seismic, well, and field data show that faults can and often do curve. However, in areas of rugged terrain and private property constraints such as the Santa Monica Mountains, such methods cannot be employed to determine the subsurface geometry of the faults. It is in these areas that this analysis provides the most reasonable estimate of locations where the surface trace of a fault associated with a specific earthquake may be located.

In order to classify a fault as potentially seismogenic, a method was used which involved plotting the error regions for strike and dip, and trend and plunge for a specific earthquake and fault onto a stereonet. When the error regions overlapped, it was determined that the earthquake and fault have similar characteristics and are correlative. Error associated with measurements collected in the field was typically ~2-15º. However, error associated with the focal mechanism solutions was typically much larger (~25-80º). The large error associated with some focal mechanism solutions indicates the substantial uncertainty in correlation for those events.

Offshore Study Area

Five faults were interpreted in the near-shore portion of the Santa Monica Bay (figure 68). Due to the low penetration of the sub-bottom data, and the poor resolution of subsurface geometries in the boomer data, no definite offsets were detected; however, faults were typically projected along zones where the subsurface geometry was undeterminable due to gas seeps or extensive fracturing from tectonic activity. Previous attempts have been made by researchers to correlate faults in the Santa Monica Bay using geophysical methods (e.g., Greene and Kennedy,1986; Junger and Wagner, 1977). Treiman (1994) suggests that the fault locations are "judged to be uncertain and largely non-reproducible" because of possible navigational error and lack of sufficient trackline crossings.

The northern offshore fault interpreted in this study correlates with the southern edge of a denuded zone where little to no unconsolidated sediment is present. Bedding surfaces in this area appear highly contorted and are likely a result of tectonic activity (Dill, 1993). The southern boundary of the denuded zone is potentially an offshore extension of the Potrero Canyon Fault mapped along the eastern shore of Santa Monica Bay by Greene and Kennedy (1986). They suggest that the fault extends westward into the bay and connects with an onshore fault at some point along the Santa Monica coastline. Based on the trend of the denuded surface and bathymetric contours, the fault potentially links onshore with the Las Flores Thrust Fault, directly south of Topanga Canyon (figure 69).

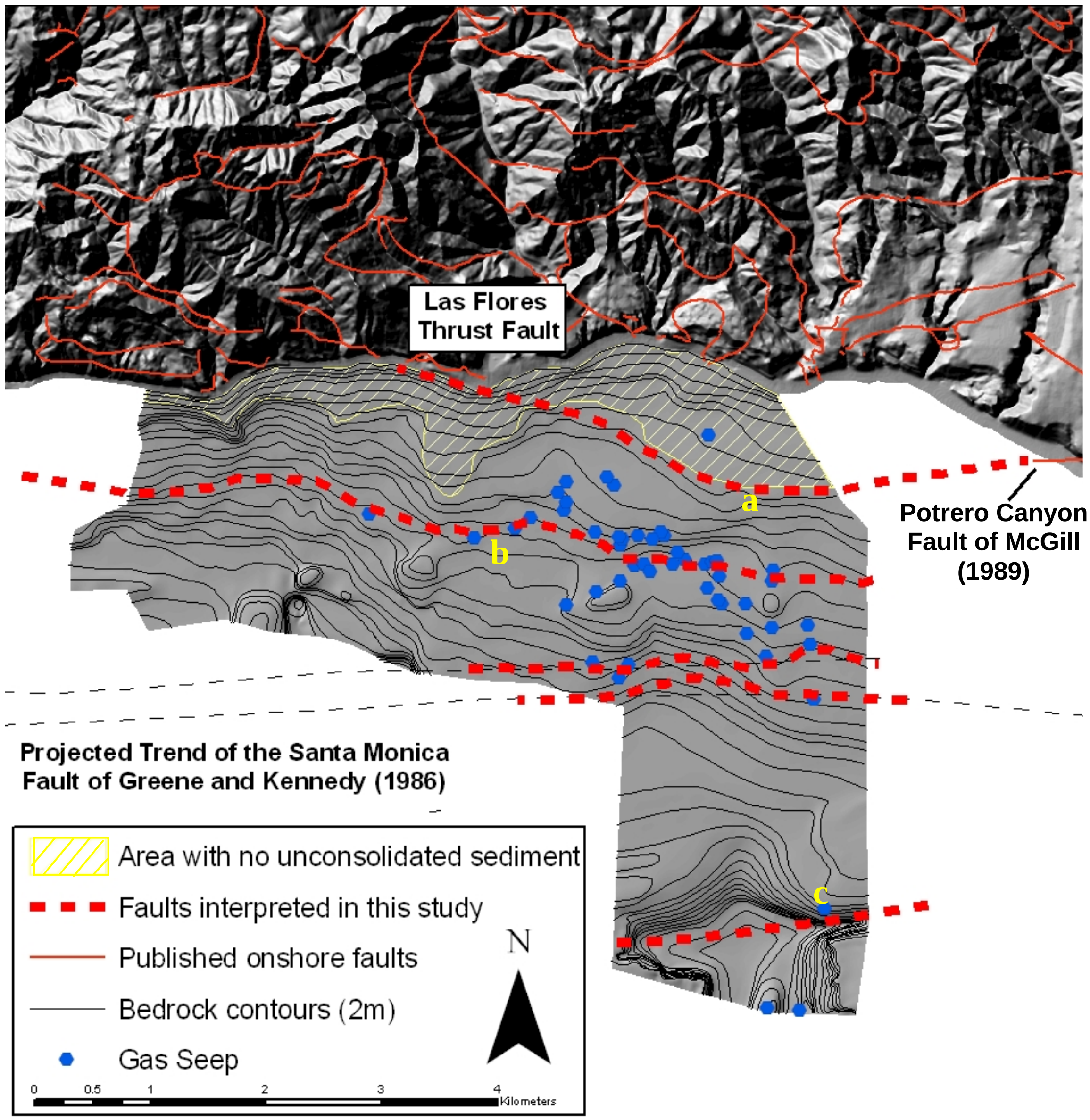

FIGURE 68.—Interpretation of faults in the Santa Monica bay based on sub-bottom acoustic data. Letters denote location of seismic lines in figures 67, 68, and 69.

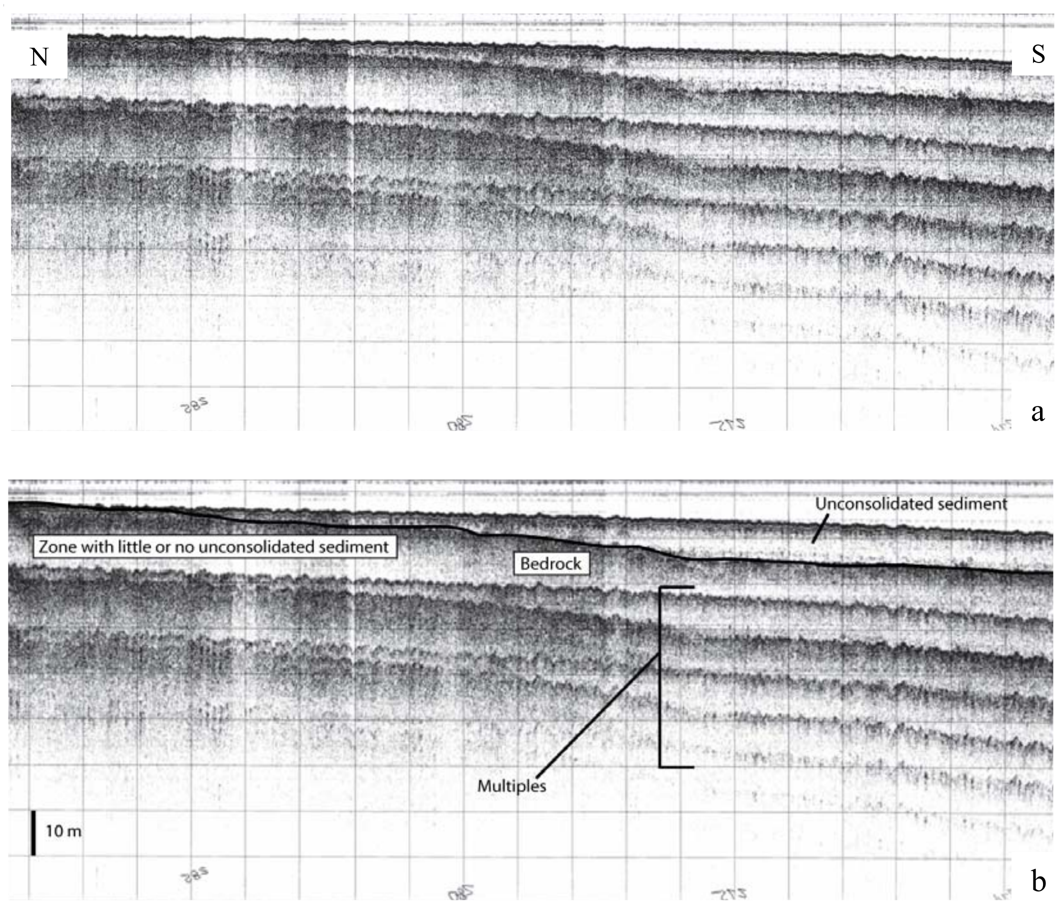

FIGURE 69.—(a) Uninterpreted and (b) interpreted seismic lines from location “a” in figure 68. (b) Near-shore area that is devoid of infered Holocene sediment. The boundary of this zone is on trend with the offshore projection of the Potrero fault.

The two faults interpreted in the center of the image correlate with the offshore location of the Santa Monica Fault of Junger and Wagner (1977), and link with the onshore location of the Santa Monica Fault of Greene and others (1986) that is located directly east of the study area. The fault locations were chosen based on locations of gas seeps, topographic trends, and areas where the seismic data appeared disturbed due to gas seeps or potential tectonic activity. The fault interpreted directly north of the two center faults correlates with the offshore trend of the Malibu Coast Fault of Dibblee (1992) and was interpreted based on bedrock trends and gas seeps (figure 70). Although the fault appears to merge with the Santa Monica Fault, it potentially trends towards the north at the point just to the southwest of the “a” on the map, to merge with the Potrero Canyon Fault. The southern fault location interpreted along the southern edge of the study area is marked in the digitized seismic records and bedrock map by a large linear trough that cuts perpendicular to beds that have undergone tilting (figure 71).

An alternate interpretation of offshore fault connections in the Santa Monica Bay is also presented in which one strand of the Santa Monica Fault trends northeast, merging with the Malibu Coast Fault (figure 72). The interpreted northeast trend of the Santa Monica Fault is based on an apparent structural trend visible in the bedrock structure map. The other strand of the Santa Monica Fault is interpreted to continue east towards the onshore location of the Santa Monica Fault. Due to ambiguity of the seismic data, both interpretations of offshore faults appear potentially valid because in many seismic records subsurface geometries are undeterminable.

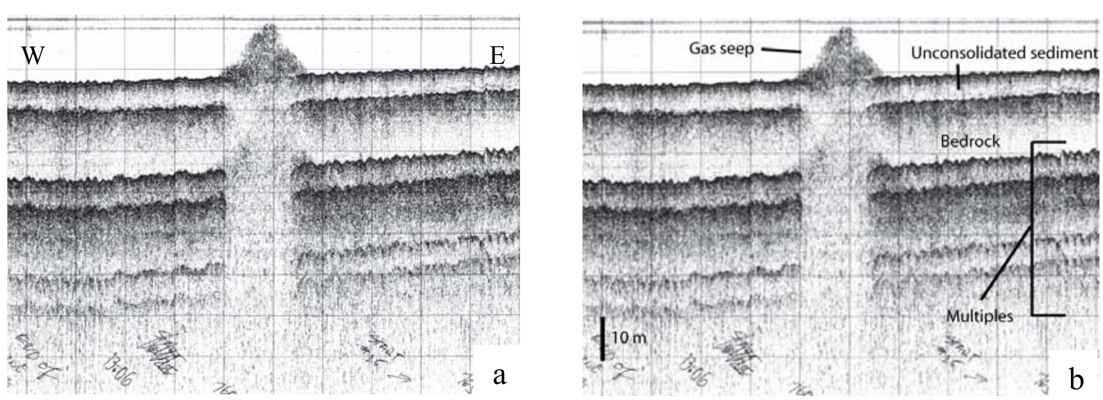

FIGURE 70.—(a) Uninterpreted and (b) interpreted seismic lines from location “b” in figure 68. Along trend of the inferred Malibu Coast Fault of Dibblee (1992) bubble screens were noted, inferred to be gas seeps associated with fractured underlying petroliferous formations.

Seismo-lineament swaths from three seismic events project into the Santa Monica Bay. Although the seismo-lineaments correlate spatially with the faults, the faults cannot be classified as potentially seismogenic because the fault surface and slip-vector orientation cannot be determined using the sub-bottom acoustic data (figure 73). In a previous study by Seidman and Cronin (2006) the auxilary plane for the March 31, 1974 event was evaluated and determined not to correlate with surface traces of faults in the Santa Monica Mountains. That would suggest that if surface traces of the fault that caused the March 31 event exist, they would likely be present in the seismo-lineament swath for the nodal plane that projected into the Santa Monica Bay.

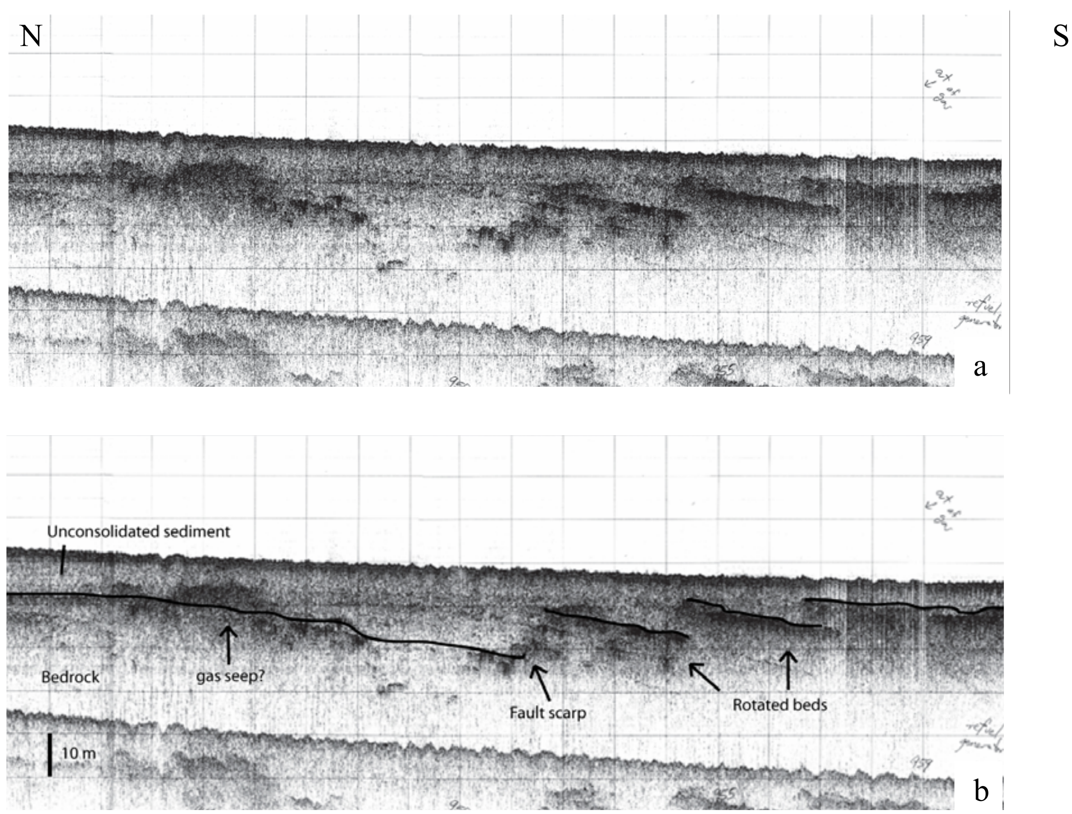

FIGURE 71.—(a) Uninterpreted and (b) interpreted seismic lines from location “c” in figure 68. Tilted structures within a buried channel located in the southern portion of the study area.

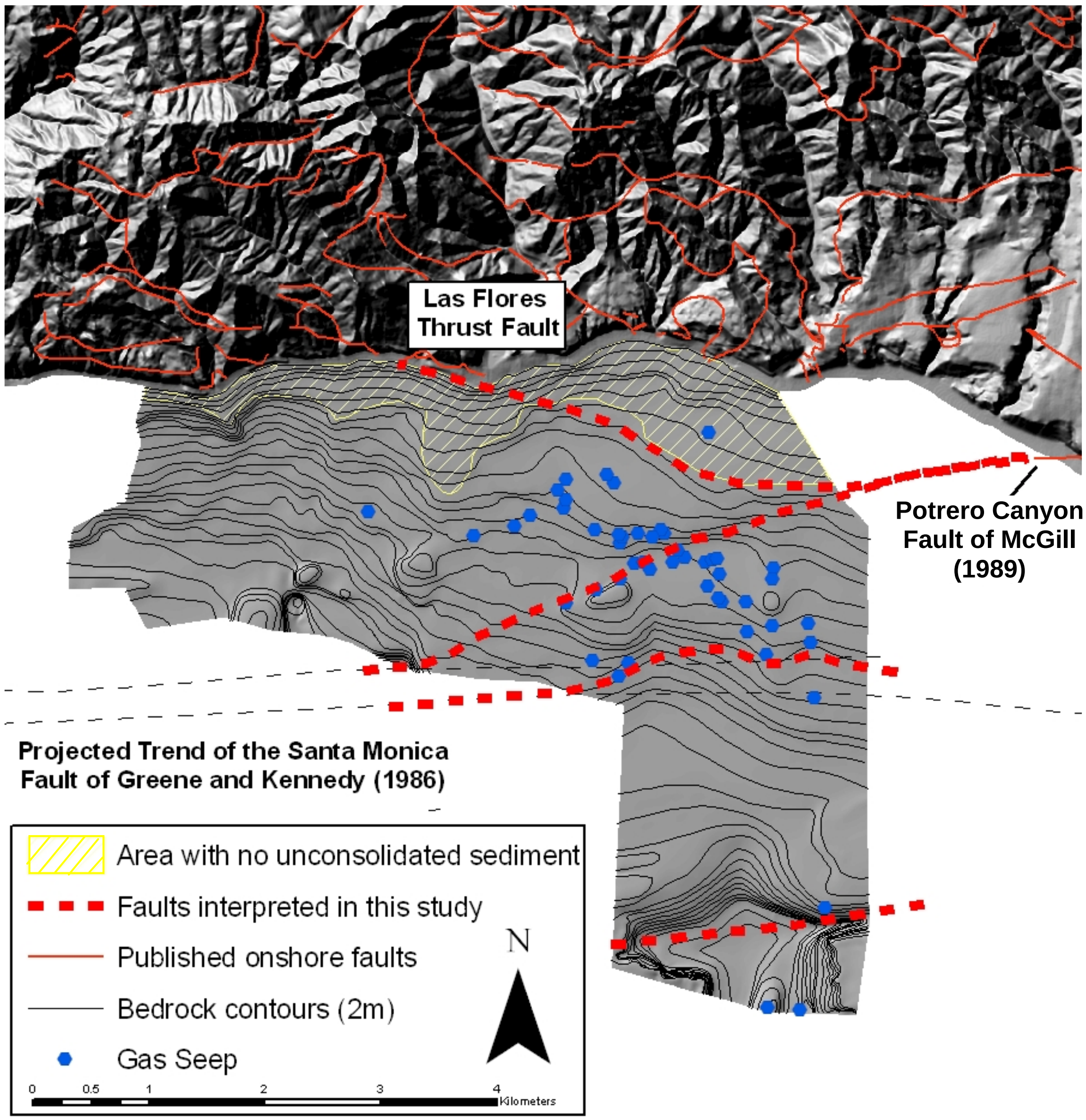

FIGURE 72.—Alternate interpretation of faults in the Santa Monica Bay based on sub-bottom data. In this interpretation, the Potrero Canyon Fault splays towards the west. The southern splay follows a gas lineament and an abrupt ridge evidenced in the seismic records while the northern splay follows the trend of the denuded zone.

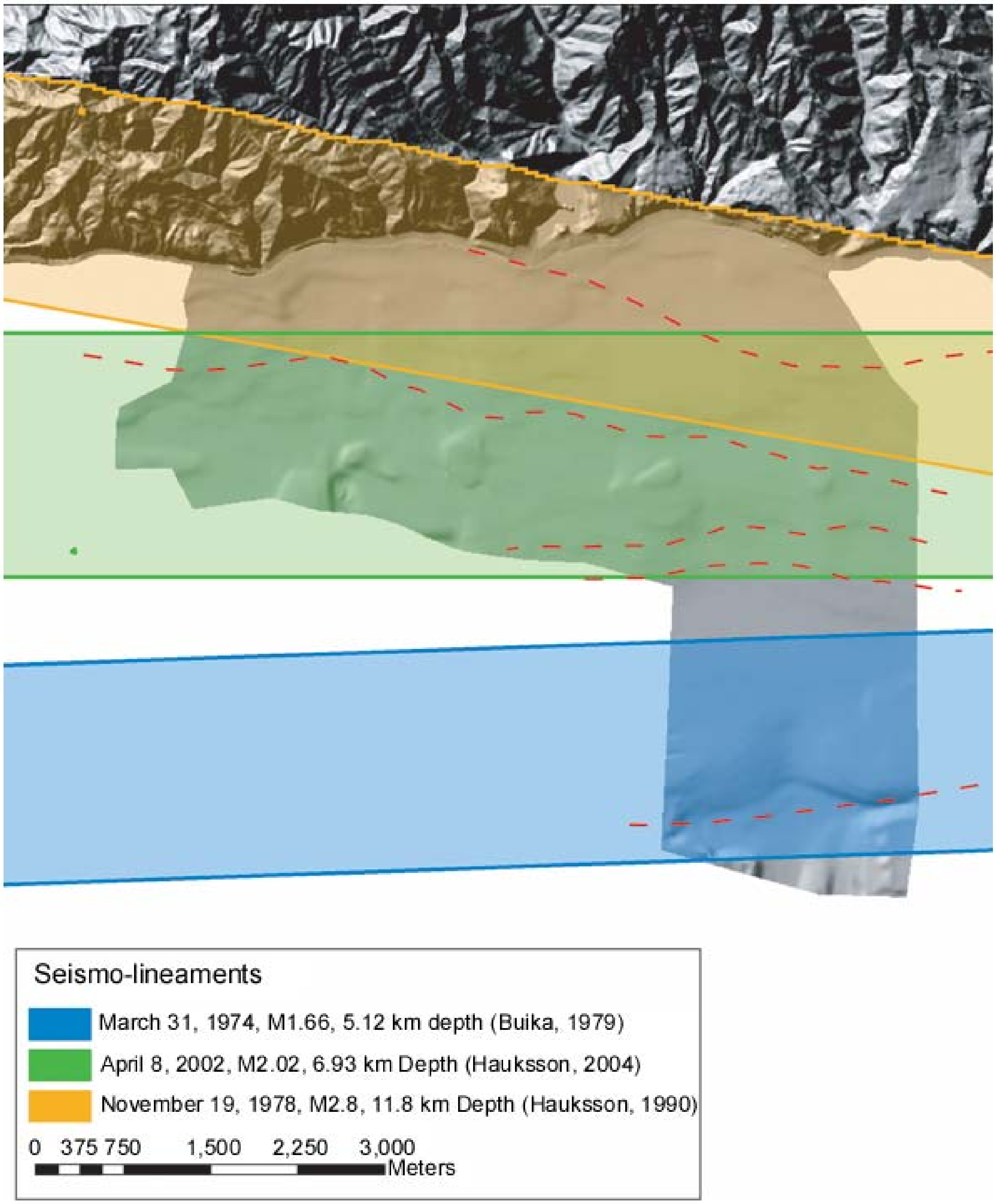

FIGURE 73.—Seismo-lineaments that project into the Santa Monica Bay. Although the seismo-lineaments correlate spatially with the faults, the faults cannot be classified as potentially seismogenic because the fault surface and slip-vector orientation cannot be determined using the sub-bottom acoustic data.

Conclusions and Suggestions for Future Research

Several mapped and previously-unmapped faults have been identified in the field, and determined to be potentially-seismogenic in the Topanga 7.5’ Quadrangle using geomorphic lineament analysis of DEMs coupled with seismo-lineament analysis. Results from the field study suggest that active seismogenic faulting in the Santa Monica Mountains is not restricted to the Malibu Coast Fault Zone as previously hypothesized.

Results from the sub-bottom acoustic survey present evidence for the continuity of the Potrero Canyon and Santa Monica Faults in the near-shore portion of the Santa Monica Bay. Seismo-lineaments projected into the Santa Monica Bay suggest that one or more faults identified in the study may be seismogenic.

It is suggested for future researchers in the Santa Monica Mountains that additional analysis of the newly identified faults be conducted to determine their continuity, and to identify locations where trench studies could be conducted. Also, the focal mechanism solutions used in this study could be recomputed to minimize the error margins associated with the dip and rake. This would strengthen the argument of correlating surface traces of faults with focal mechanism solutions to classify the faults as potentially-seismogenic. Future joint relocation of earthquakes analyzed in this study could minimize location uncertainty, resulting in more confident results. Also, additional sub-bottom acoustic surveys conducted adjacent to the study area, along with more data collection in questionable areas, would lead to more confident results. The preliminary results presented in this study emphasize the necessity of more in-depth investigation of fault activity in the Santa Monica Mountains.

APPENDICES

APPENDIX A

Mathematica Seismo-Lineament Code

```
startTime = AbsoluteTime[];
```

Projecting a fault plane from a focal mechanism solution onto a digital elevation model surface

Written and revised by Vince Cronin for a research project of Vince Cronin, Brian Bayliss, Lauren Seidman, Mark Millard, Bruce Byars, and Lisa Zygo

Begun August 5, 2004; Revised September 6, 2006

Introduction

The purpose of this notebook is to describe how to define the intersection of a DEM surface and a plane of given orientation that passes through a particular point located below the DEM surface. The application of this is in estimating the surface trace of a fault plane defined by an earthquake focal mechanism solution. It is hoped that this technique, in conjunction with structural terrain analysis and field mapping, will assist in the identification of the surface traces of seismogenic faults.

Each fault surface is initially represented by an upward-directed unit vector that is normal to the fault plane and whose origin is at the earthquake focus. Each location vector to a point on the DEM surface grid is evaluated to determine whether it is within a user-defined region around 90° from the vector normal to the fault. If so, that grid location is identified as being along the surface trace of the fault plane, or within the uncertainty region around the fault plane. The result of evaluating every point on the DEM surface grid in this manner is a subset of points that collectively define the surface trace of the fault plane and the associated uncertainty region across the DEM surface.

The output from this application is a set of 3 files, whose names are defined by the user.

- One file is an encapsulated PostScript file (.eps) that contains the graphic showing the DEM shaded by elevation, the topographic contours at ~500 ft increments, curves marking the boundaries of the uncertainty region, and a curve showing the trace of the fault-plane solution intersection with the topography.
- Another file is a data file (.dat) with the same dimensions as the input DEM .dat file, but whose values are either the null value (-9999) or, for points located along the trace of the fault-plane solution intersection with the topography, some other value (typically "1" or the DEM-derived elevation at that node point).
- The other file is a data file (.dat) with the same dimensions as the input DEM .dat file, but whose values are either the null value (-9999) or, for points located along the boundaries of the uncertainty region, some other value (typically "1" or the DEM-derived elevation at that node point).

Explanation of changes to this code that are necessary to evaluate another fault plane solution

The list of changes noted below was created assuming that this code is going to be used to evaluate the DAT file "xport2" that is a digital elevation model (DEM) of part of the Malibu coastline in California. Malibu is in UTM Zone 11, whose central meridian is longitude -117 degrees. If those assumptions are not true, additional items will have to be adjusted.
(1) In the "Description of input data" section, the user must supply values for the following variables: focalLat, focalLong, reportedFocalDepthKm, faultDipTrend, faultDipPlunge, reportedVertError, horizError.
(2) In the "Import the DEM data from a DAT file" subsection of the "Digital elevation model (DEM)" section, the user may need to modify the path information so this notebook can find the input DEM/DAT file.
(3) In the "Export data and image files" section at the end of this code, the user must supply different names for the output files to avoid over-writing the results of previous runs.

Description of input data

▪ Data source for focal mechanism solution used in this run

Egil Hauksson, http://www.data.scec.org/ftp/catalogs/hauksson/Socal_focal

▪ From focal mechanism solution

Epicenter location: latitude (focalLat) and longitude (focalLong) in decimal degrees.

```
focalLat = 34.05617;
```

```
focalLong = -118.82117;
```

Focal depth (focalDepthKm) in kilometers

```
reportedFocalDepthKm = 11.18;
```

The central meridian of UTM Zone 11 is longitude -117°.

```
zoneMeridian = -117;
```

Trend (faultDipTrend) and plunge (faultDipPlunge) of dip vector of the fault plane, in decimal degrees

```
faultDipTrend = 185;
```

```
faultDipPlunge = 75;
```

Reported vertical (reportedVertError) and horizontal (horizError) uncertainties in the location of the earthquake focus, in kilometers.

```
reportedVertError = 28.1;

horizError = 0.2;
```

Some user-defined functions

```
makeVector[plunge_, trend_] := {Cos[plunge Degree] Sin[trend Degree],
   Cos[plunge Degree] Cos[trend Degree], -Sin[plunge Degree]};

vectorNorm[x_] := √x.x ;

unitVector[x_] :=
  {x[[1]] / vectorNorm[x], x[[2]] / vectorNorm[x], x[[3]] / vectorNorm[x]};

vectorAngle[a_, b_] := ArcCos[a.b / (vectorNorm[a] vectorNorm[b])];
```

The lat/long to UTM conversion is after Snyder, 1982.

```
convertToUTM[inLat_, inLong_, centMerid_] :=
  Module[{c1, c2, c3, c4, c5, v1, v2, v3, v4, v5, v6, utmX, utmY}, c1 = 6378206.4;
   c2 = 0.00676866; c3 = 0; c4 = centMerid; c5 = 0.9996; v1 = c2 / (1 - c2);
   v2 = c1 / Sqrt[1 - (c2 * (Sin[inLat Degree]^2))]; v3 = Tan[inLat Degree]^2;
   v4 = v1 * (Cos[inLat Degree]^2); v5 = (Cos[inLat Degree]) * ((inLong - c4) (π/180));
   v6 = (111132.0894 * inLat) - (16216.94 * Sin[2 * (inLat Degree)]) +
     (17.21 * Sin[4 * (inLat Degree)]) - (0.02 * Sin[6 * (inLat Degree)]);
   utmX = (c5 * v2 * (v5 + (((1 - v3 + v4) * v5^3) / 6) +
         ((5 - (18 * v3) + (v3^2) + (72 * v4) - (58 * v1)) * v5^5) / 120)) + 500000;
   utmY = c5 * (v6 - 0 + (v2 * Tan[inLat Degree] * ((v5^2 / 2) +
          (((5 - v3 + (9 * v4) + (4 * (v4^2))) * v5^4) / 24) + (((61 - (58 * v3) +
              (v3^2) + (600 * v4) - (330 * v1)) * v5^6) / 720)))); {utmX, utmY}];

General::spell1 :
 Possible spelling error: new symbol name "utmY" is similar to existing symbol "utmX". More…
```

The following module differentiates between points that are within "width" meters from the fault plane and those that are further away. Given unit vector N that is normal to the fault plane that passes through the origin of the coordinate system, the distance from an arbitrary point (whose position vector is P) to that plane is given by |N·P|.

```
pointEvaluator[xCoord_, yCoord_, zCoord_, width_, fltUNrml_, nulData_] :=
  Module[{locVect, distToFlt, result}, locVect = {xCoord, yCoord, zCoord};
   distToFlt = If[(zCoord < (-1000)), width, Abs[Dot[fltUNrml, locVect]]];
   result = If[(distToFlt ≤ width), zCoord, nulData]; result];
```

Defining the vertical extent of the uncertainty region around the earthquake focus

Defining the vertical extent of the uncertainty region around the earthquake focus is not always a simple matter of modifying the reported focal depth by the reported vertical error above and below the focus. In some cases, the combination of focal depth and stated vertical error yields locations that are above ground level, or below the reasonably expected depth of an earthquake focus in the area. The deepest reported earthquake in the west or central Santa Monica Mountains was a M2.9 event on February 1, 1994, located at longitude -119.17 and latitude 34.15, with a focal depth of 23 km (NEIC). The shallowest reported focal depths are less than 1 km. The highest elevation in the Santa Monica Mountains is Castro Peak, at 2,824 feet (861 meters).
The variable "upperBound" marks either the upper boundary of the crustal seismogenic zone (set at sea level) or the upper part of the uncertainty region for the earthquake focus, whichever is deeper.

```
upperBound = If[(reportedFocalDepthKm - reportedVertError) < 0,
   0., (reportedFocalDepthKm - reportedVertError)];
```

The variable "lowerBound" marks either the lower boundary of the crustal seismogenic zone (set at 23 km for the Malibu study) or the lower part of the uncertainty region for the earthquake focus,whichever is shallower.

```
lowerBound = If[(reportedFocalDepthKm + reportedVertError) > 23,
   23., (reportedFocalDepthKm + reportedVertError)];
```

The variable "meanFocalDepthKm" is the depth half way between the upper bound and the lower bound.

```
meanFocalDepthKm = upperBound + ((lowerBound - upperBound) / 2);
```

In situations where the reported error bars cause us to consider the possibility of an earthquake focus that is in the atmosphere or below the regional norm for the base of the seismogenic zone, we use a "pseudofocus" located between the upper and lower boundaries of the seismogenic zone for the purpose of mapping the uncertainty swath across the DEM.

```
focalDepthKm = If[meanFocalDepthKm ≠ reportedFocalDepthKm,
   meanFocalDepthKm, reportedFocalDepthKm];
```

The "vertError" is half the vertical uncertainty in focus location, expressed in meters. In situations where a "pseudofocus" is used, the vertical error will differ from the reported vertical error, allowing us to map a more reasonable uncertainty swath across the DEM.

```
vertError = If[focalDepthKm ≠ reportedFocalDepthKm,
   (meanFocalDepthKm * 1000), (reportedVertError * 1000)];
```

Find the unit vector normal to the fault surface at the earthquake focus

Convert the fault dip vector from trend and plunge to a unit location vector (dipUnitVector)

```
faultDipUnitVector = unitVector[makeVector[faultDipPlunge, faultDipTrend]];
```

Find the dip azimuth vector (dipAzimuthVector)

```
dipAzimuthVector = {Sin[faultDipTrend Degree], Cos[faultDipTrend Degree], 0};
```

Find the strike vector (strikeVector) defined using the right-hand rule

```
faultStrikeTrend = faultDipTrend - 90;

strikeVector = {Sin[faultStrikeTrend Degree], Cos[faultStrikeTrend Degree], 0};
```

Find the unit vector that is normal to the fault plane and is directed upwards (faultUnitNormal)

```
faultUnitNormal = unitVector[faultDipUnitVector × strikeVector];
```

Digital elevation model (DEM)

The digital elevation model is presented as a set of z data in meters, with x and y coordinates explicit from the position of the z datum in the data file. The data file is derived from the U.S. Geological Survey's DEM data for the Pt. Dume, Malibu Beach and Topanga 7.5 minute quadrangles (30 m resolution).
The DEM was acquired from ____

▪ Import the DEM data from a DAT file

It is assumed that the DEM data is in a file called "xport.2" that is on the desktop,
with the path "C:\\Documents and Settings\\Vince_Cronin\\Desktop\\LaurenSeidmanCode\\xport2.dat"
This information should be adjusted as appropriate when this code is used by other people on other machines.

```
mydata = Import["C:\\Documents and Settings
     \\Mark_Millard\\Desktop\\IHateMyLife\\xport2clip.dat"];
```

▪ Read and interpret the DEM header information

Read the header information.

```
headerData = Table[mydata[[i, j]], {i, 6}, {j, 2}];
```

"ncols" is the number of columns; label in position [[1,1]] and value in [[1,2]]

```
ncols = headerData[[1, 2]];
```

"nrows" is the number of rows; label in position [[2,1]] and value in [[2,2]]

```
nrows = headerData[[2, 2]];
```

"xllcorner" is the UTM zone 11 "x" coordinate, in meters, of the lower left corner of the DEM; label in position [[3,1]] and value in [[3,2]].

```
xllcorner = headerData[[3, 2]];
```

"yllcorner" is the UTM zone 11 "y" coordinate, in meters, of the lower left corner of the DEM; label in position [[4,1]] and value in [[4,2]]

```
yllcorner = headerData[[4, 2]];

General::spell1 : Possible spelling error: new
   symbol name "yllcorner" is similar to existing symbol "xllcorner". More…
```

"gridSpacing" a.k.a. "cellsize" is the distance between grid nodes in the DEM file, in meters; label in position [[5,1]] and value in [[5,2]]
Note that the code below uses the variable name "gridSpacing" rather than "cellsize."

```
gridSpacing = headerData[[5, 2]];
```

"nodata_value" is the value used in the data file to indicate that there is no data in a specific location in the data file; label in position [[6,1]] and value in [[6,2]]

```
nodataValue = headerData[[6, 2]];
```

The seventh row of the data set is the first data row.

The true UTM coordinates of the datum in position [[i,j]] of the data set (from row 7 to the end) are as follows:

x coordinate = xllcorner + (cellsize * (j - 1)) y coordinate = yllcorner + (cellsize * (nrows - i))
z coordinate = the datum in position [[i,j]]

Convert the input coordinates of the earthquake focus to the same coordinate system as the DEM data

```
utmCoordinates = convertToUTM[focalLat, focalLong, zoneMeridian];
```

The "focus" is the (x, y, z) coordinates in meters of the "pseudofocus" located at a depth half way between the upper and lower boundaries of the vertical uncertainty region, in a coordinate system in which the origin is the lower-left (southwest) corner of the DEM at sea level.

```
focus = {(utmCoordinates[[1]] - xllcorner),
   (utmCoordinates[[2]] - yllcorner), (focalDepthKm * (-1000))};
```

The "reptFocus" is the (x, y, z) coordinates in meters of the reported earthquake focus, in a coordinate system in which the origin is the lower-left (southwest) corner of the DEM at sea level.

```
reptFocus = {(utmCoordinates[[1]] - xllcorner),
   (utmCoordinates[[2]] - yllcorner), (reportedFocalDepthKm * (-1000))};
```

Define the threshold for resolving whether a point in the DEM is within the fault swath

The "zoneHalfWidth" is twice the distance between the parallel planes that bound the uncertainty region for this fault-plane solution. The units are meters.

```
zoneHalfWidth = (vertError * Cos[faultDipPlunge Degree]) +
   (horizError * 1000 * Sin[faultDipPlunge Degree]);
```

The "innerZone" is the minimal width of the surface trace of the fault-plane solution, needed to define the trace given the input grid spacing. The units are meters.

```
innerZone = ((0.6 * gridSpacing) * Sin[faultDipPlunge Degree]);
```

▪ Determine which points on the DEM lie along the modeled fault-plane trace, ± the width of the "innerZone," and map their boundary with points that do not lie along the fault-plane trace

The UTM coordinates of each point from the DEM are transformed to a coordinate system whose origin is at the earthquake focus
(focus = {(utmCoordinates[[1]]-xllcorner),(utmCoordinates[[2]]- yllcorner),(focalDepthKm*(-1000))}).

x coordinate=(gridSpacing*(j-1))-focus[[1]]   y coordinate=(gridSpacing*(nrows-i))-focus[[2]]
z coordinate=(the datum in position [[i,j]])-focus[[3]]

```
inFaultTrace = Table[pointEvaluator[((gridSpacing * (j - 1)) - reptFocus[[1]]),
    ((gridSpacing * (nrows - i)) - reptFocus[[2]]),
    (mydata[[i + 6, j]] - reptFocus[[3]]), innerZone,
    faultUnitNormal, nodataValue], {i, nrows}, {j, ncols}];

elev1 = Table[inFaultTrace[[i, j]], {i, nrows, 1, -1}, {j, ncols}];
```

```
traceImageFile1 = ListContourPlot[elev1,
  ContourShading → False, AspectRatio → Automatic, Contours → {0}]
```

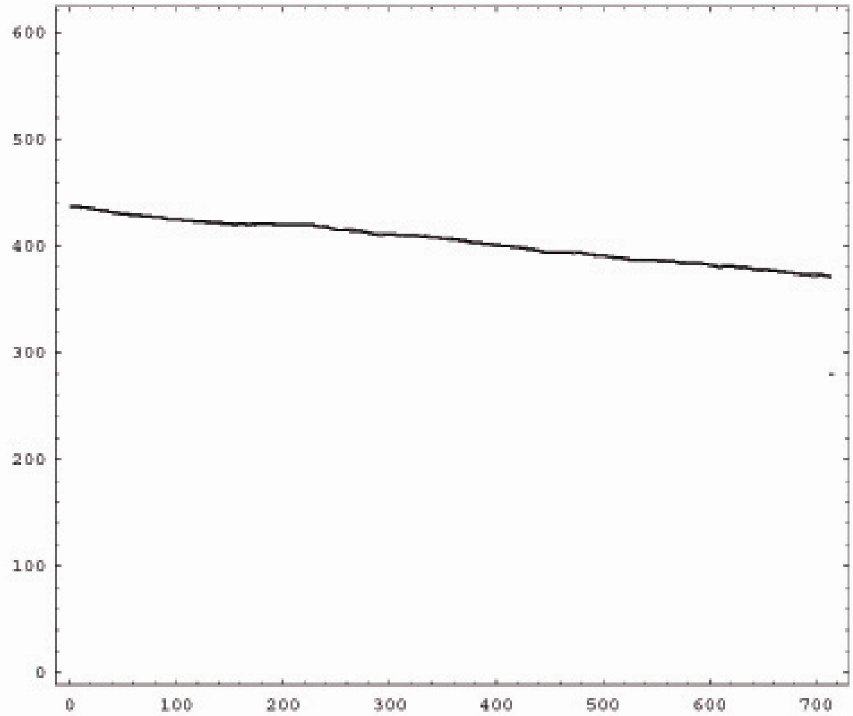

- ContourGraphics -

- **Determine which points on the DEM lie within the uncertainty swath for the fault location, ± the width of the "zoneHalfWidth," and map their boundary with the points that lie outside the swath**

```
uncertSwath = Table[pointEvaluator[((gridSpacing * (j - 1)) - focus[[1]]),
    ((gridSpacing * (nrows - i)) - focus[[2]]), (mydata[[i + 6, j]] - focus[[3]]),
    zoneHalfWidth, faultUnitNormal, nodataValue], {i, nrows}, {j, ncols}];

elev2 = Table[uncertSwath[[i, j]], {i, nrows, 1, -1}, {j, ncols}];
```

```
traceImageFile2 = ListContourPlot[elev2,
  ContourShading → False, AspectRatio → Automatic, Contours → {0}]
```

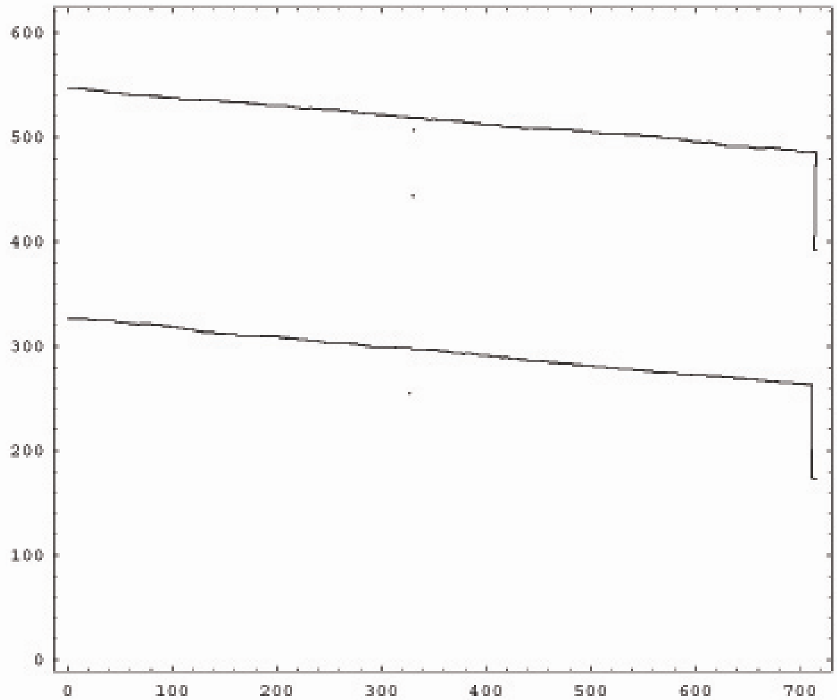

```
- ContourGraphics -
```

■ Combine the fault-trace map with the fault-swath map into a single graphic

```
traceImageFile = Show[%, traceImageFile1];
```

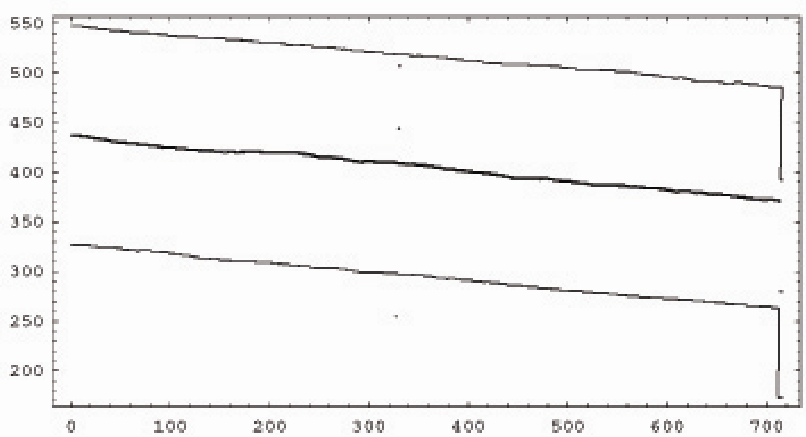

- **Plot a topographic contour map of the DEM, at a contour interval of 500 feet (152.4 meters)**

```
demImageFile = Table[mydata[[i + 6, j]] - focus[[3]], {i, nrows}, {j, ncols}];

aratio = nrows / ncols;
minval = 0;
maxval = Max[demImageFile];
relief = (maxval - minval);

elev3 = Table[demImageFile[[i, j]] + focus[[3]], {i, nrows, 1, -1}, {j, ncols}];

topoMap = ListContourPlot[elev3, ContourShading → False, Frame → False,
   AspectRatio → aratio, Contours → Table[c, {c, -152.3, 1000, 152.4}]];
```

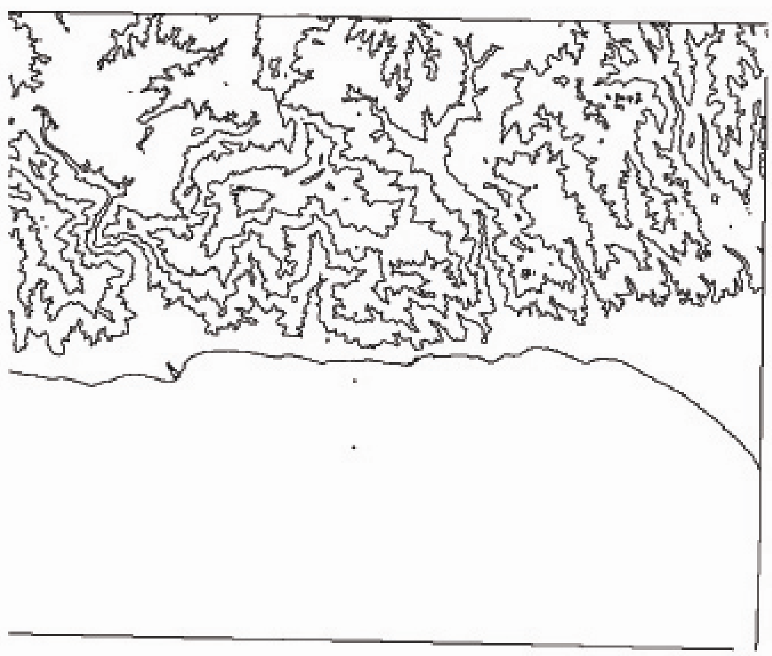

```
ListDensityPlot[elev3, AspectRatio → aratio, Frame → False,
  Mesh → False, ColorFunction → Function[z, GrayLevel[(0.3 + 0.7 z)]]];
```

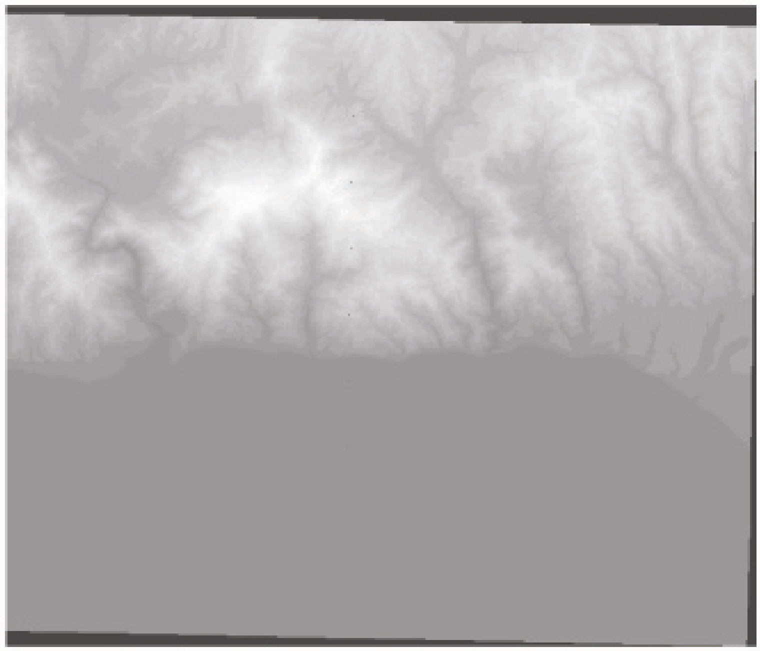

```
shadedTopoMap = Show[%, topoMap];
```

```
finalImage = Show[shadedTopoMap, traceImageFile]
```

```
- Graphics -
```

■ Add the original header data to the output files

```
mergedData = Join[headerData, inFaultTrace];

mergedSwathData = Join[headerData, uncertSwath];
```

■ Export data and image files

The file created in the next line is a data file (.dat) with the same dimensions as the input DEM .dat file, but whose values are either the null value (-9999) or, for points located along the trace of the fault-plane solution intersection with the topography, some other value (typically "1" or the DEM-derived elevation at that node point).

```
Export["C:\\Documents and Settings\\Mark_Millard\\
    Desktop\\IHateMyLife\\20031031010718aseisLina.dat", mergedData];
```

The file created in the next line is a data file (.dat) with the same dimensions as the input DEM .dat file, but whose values are either the null value (-9999) or, for points located along the boundaries of the uncertainty region, some other value (typically "1" or the DEM-derived elevation at that node point).

```
Export["C:\\Documents and Settings\\Mark_Millard\\Desktop
    \\IHateMyLife\\20031031010718bseisLina.dat", mergedSwathData];
```

The file created in the next line is an encapsulated PostScript file (.eps) that contains the graphic showing the DEM shaded by elevation, the topographic contours at ~500 ft increments, curves marking the boundaries of the uncertainty region, and a curve showing the trace of the fault-plane solution intersection with the topography.

```
Export["C:\\Documents and Settings\\Mark_Millard\\Desktop\\
    IHateMyLife\\20031031010718seisLinMapa.eps", finalImage, "EPS"];

ClearAll[mergedData, mergedSwathData, traceImageFile,
  traceImageFile1, traceImageFile2, finalImage, shadedTopoMap,
  mydata, inFaultTrace, uncertSwath, elev1, elev2, elev3];
```

▪ How long did this program take to run, in minutes?

```
minutesForProcessing = (AbsoluteTime[] - startTime) / 60

20.231001610
```

References

Colley, S.J., 2002, Vector calculus [2nd edition]: Upper Saddle River, New Jersey, Prentice-Hall, 558 p., (pp. 43-50), ISBN 0-13-041531-6.

Cronin, V.S., and Sverdrup, K.A., 1998, Preliminary assessment of the seismicity of the Malibu Coast Fault Zone, southern California, and related issues of philosophy and practice, *in* Welby, C.W., and Gowan, M.E. [editors], A Paradox of Power--Voices of Warning and Reason in the Geosciences: Geological Society of America, Reviews in Engineering Geology, p. 123-155.

Cronin, V.S., Byars, B.W., and Gammill, T., 2003, Developing techniques for regional structural interpretation using GIS and DEM-based terrain analysis: Geological Society of America, Abstracts with Programs, v. 34, no. 7, p. 261. http://gsa.confex.com/gsa/2003AM/finalprogram/abstract_61851.htm

Davis, H.F., and Snider, A.D., 1987, Introduction to vector analysis [5th edition]: Boston, Allyn and Bacon, 365 p. (pp. 34-37), ISBN 0-205-10263-8.

Gammill, T., Cronin, V.S., and Byars, B.W., 2004, Combining earthquake focal data and digital map analysis in reconnaissance for active faults, central Santa Monica Mountains and northern Santa Monica Bay, California: Geological Society of America, Abstracts with Programs,v. 36, no. 5, http://gsa.confex.com/gsa/2004-AM/finalprogram/abstract_80352.htm

Haneberg, W.C., 2004, Computational geosciences with *Mathematica*: Berlin, Springer-Verlag, 381 p., CD, ISBN 3-540-40245-4.

Snyder, J.P., 1982, Map projections used by the U.S. Geological Survey: U.S. Geological Survey Bulletin 1532, pp. 63-69 and 233-235.

APPENDIX B

Further Tests of the Seismo-Lineament Method

This appendix contains screenshots from further tests of the seismo-lineament method on earthquakes associated with known surface rupture. In all of the tests displayed, the orientation and slip characteristics of the surface rupture were similar to those of the fault plane solutions associated with the seismic event.

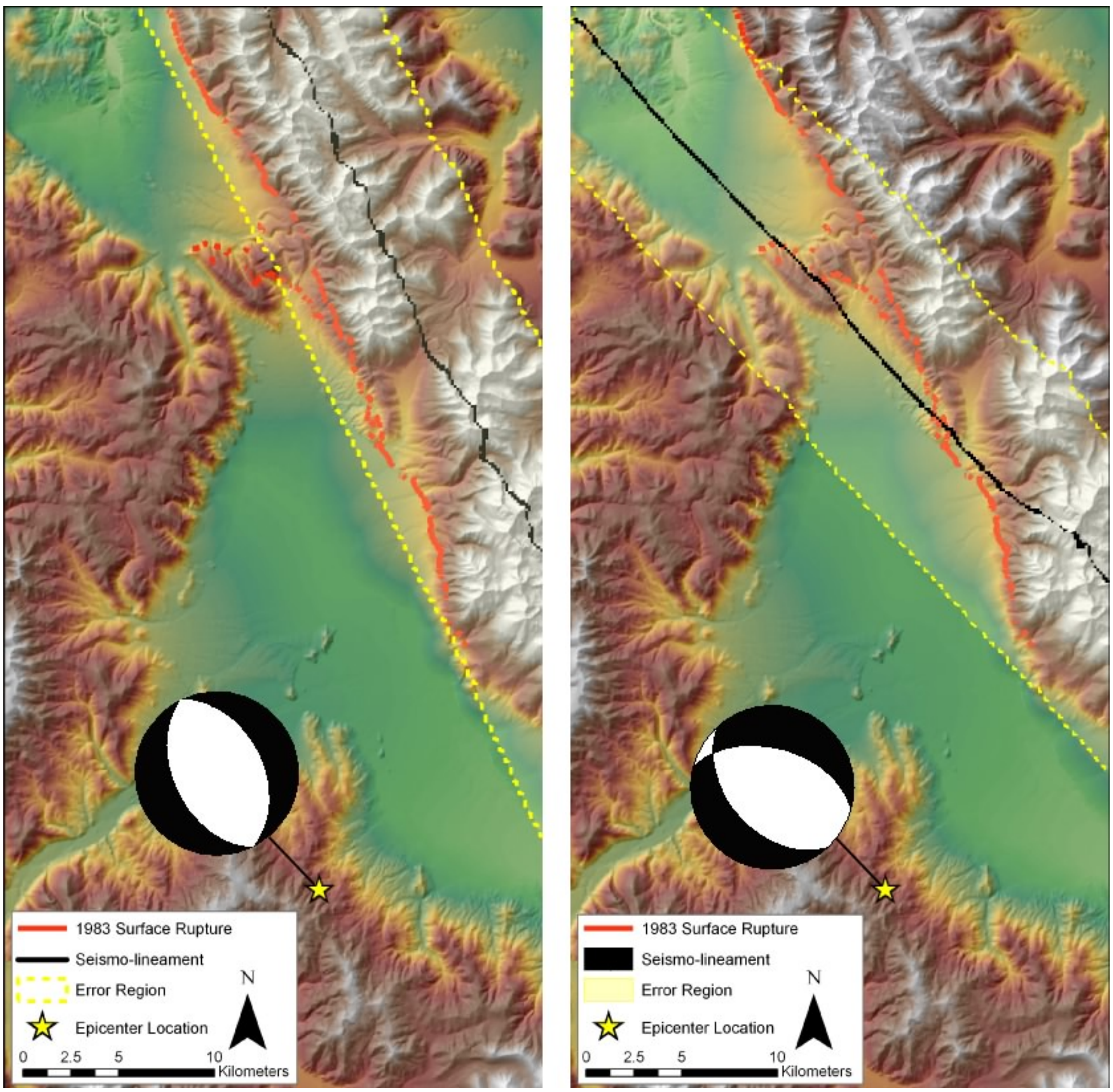

1983, M 7.3 Borah Peak, ID Earthquake. Surface traces mapped by Crone and others (1987). Epicenter determination by Richins and others (1987). Source parameters (left) by Stein and Barrientos (1985), and (right) from Doser and Smith (1985).

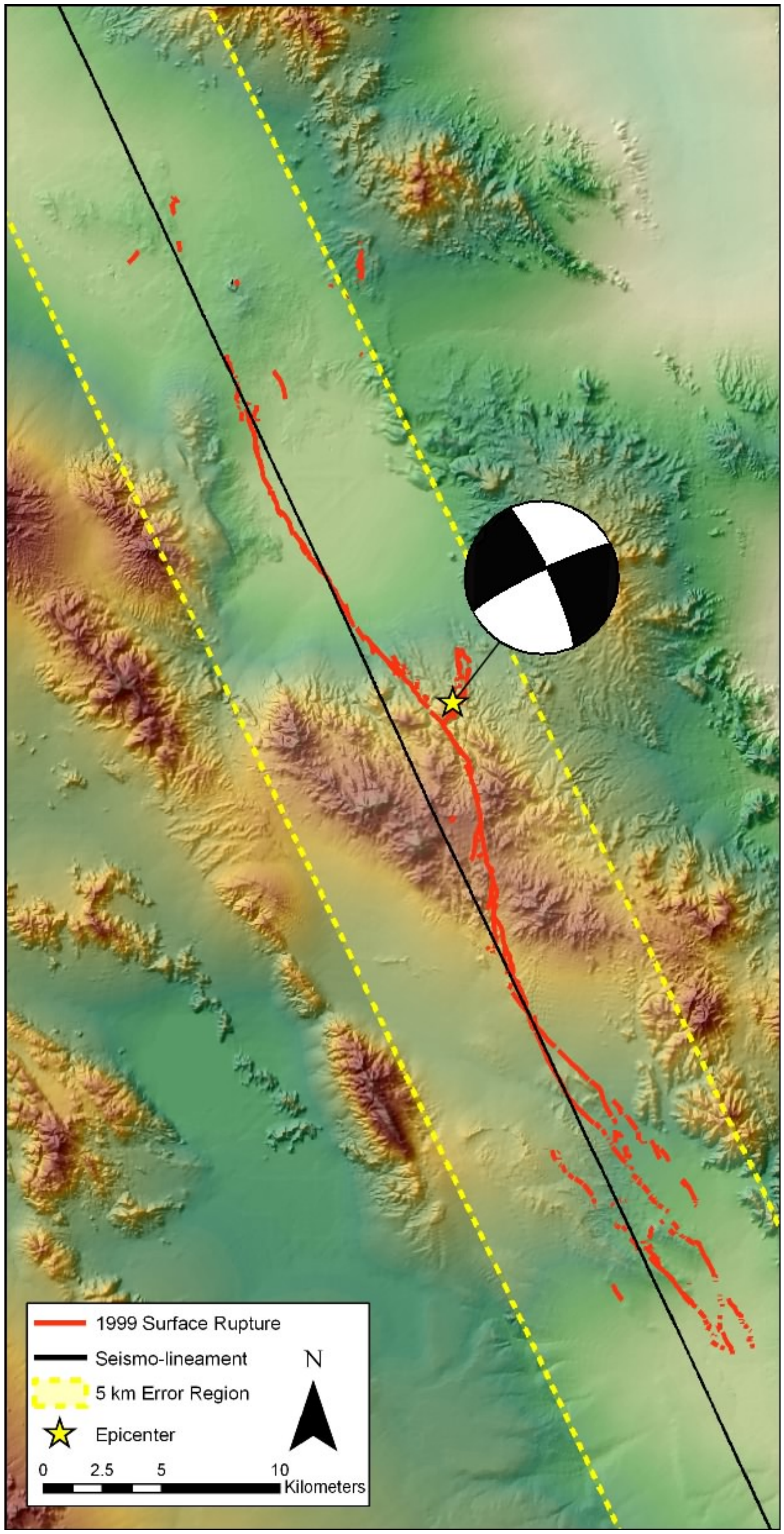

1999, M 7.1 Hector Mine, CA Earthquake. Surface traces mapped by Treiman and others (2002). Source parameters from the NEIC online catalog.

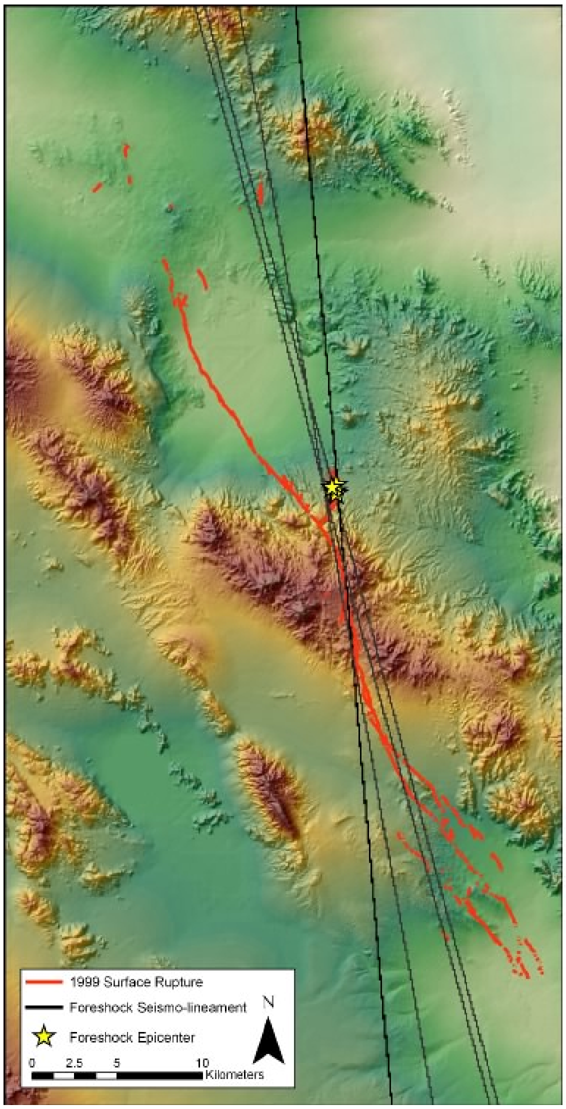

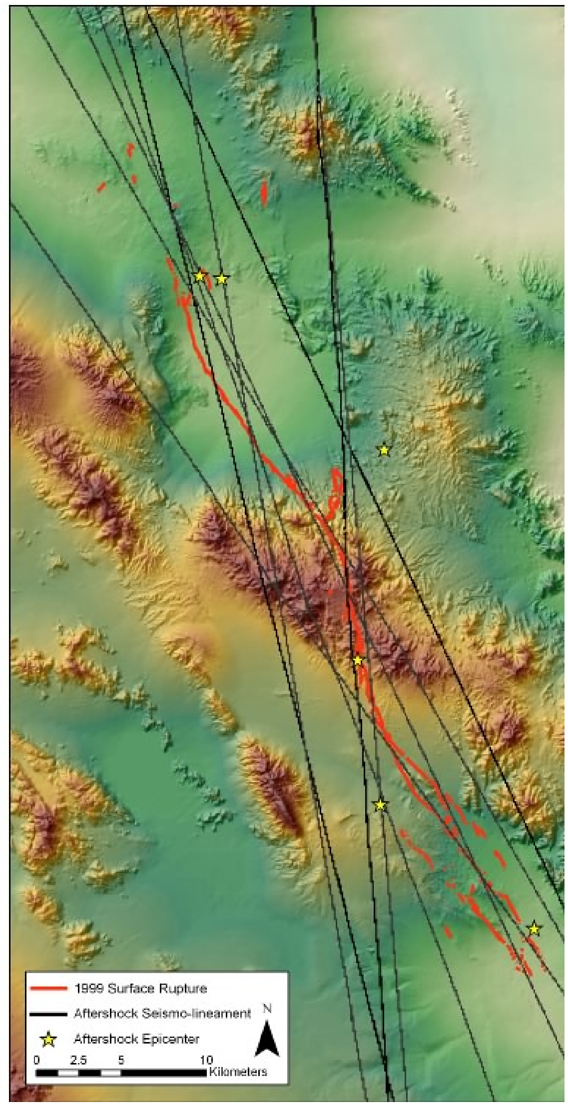

Foreshocks (left) and aftershocks (right) of the 1999, M 7.1 Hector Mine, CA earthquake. Surface traces mapped by Treiman and others (2002). Source parameters by Hauksson and others (2002).

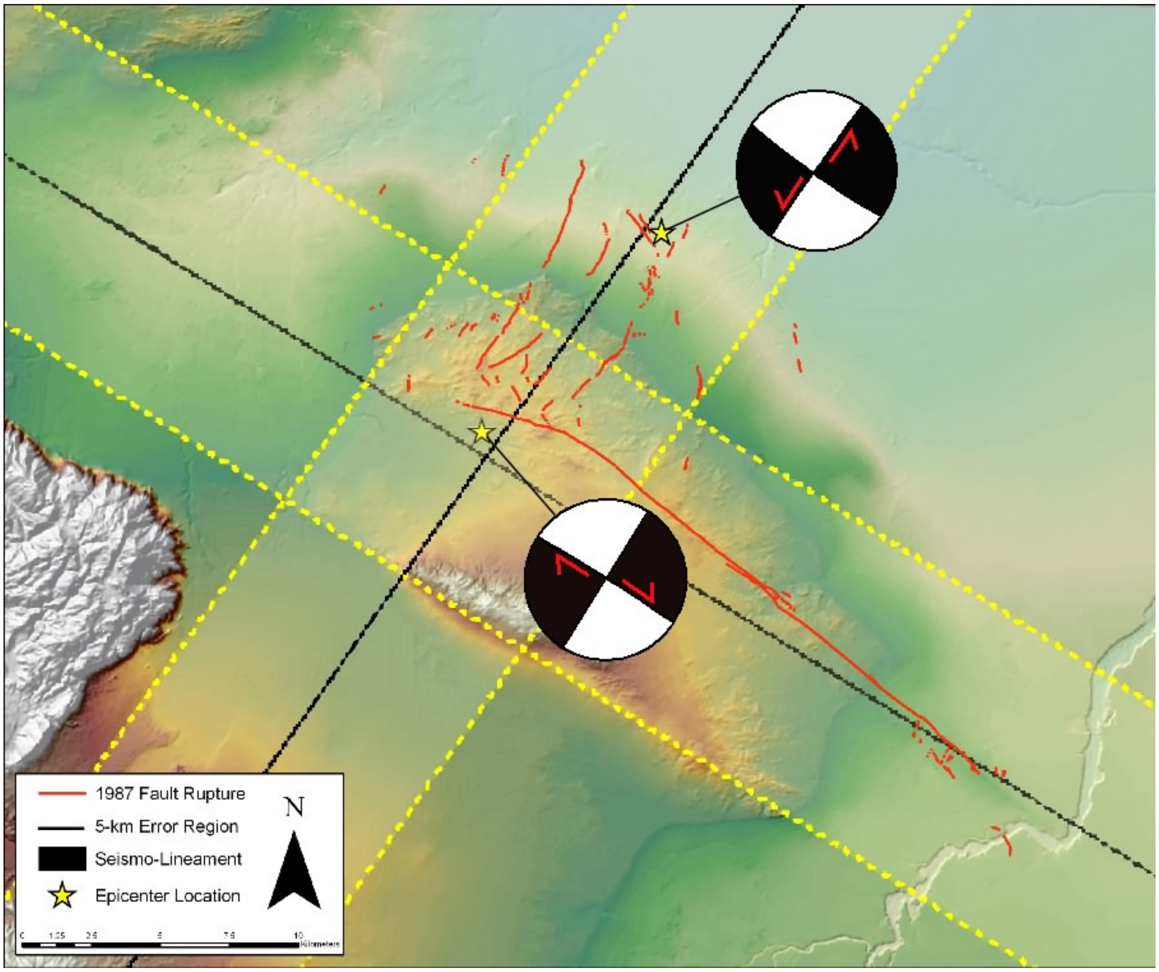

1987, M 6.2 and 6.6 Elmore Ranch and Superstition Hills, CA Earthquakes. Surface traces mapped by Sharp and others (1989). Source parameters from the NEIC online catalog. The Elmore Ranch Earthquake occurred along a previously unmapped (NE-SW trending) fault zone, and initiated movement along the (NW-SE trending) Superstition Hills Fault.

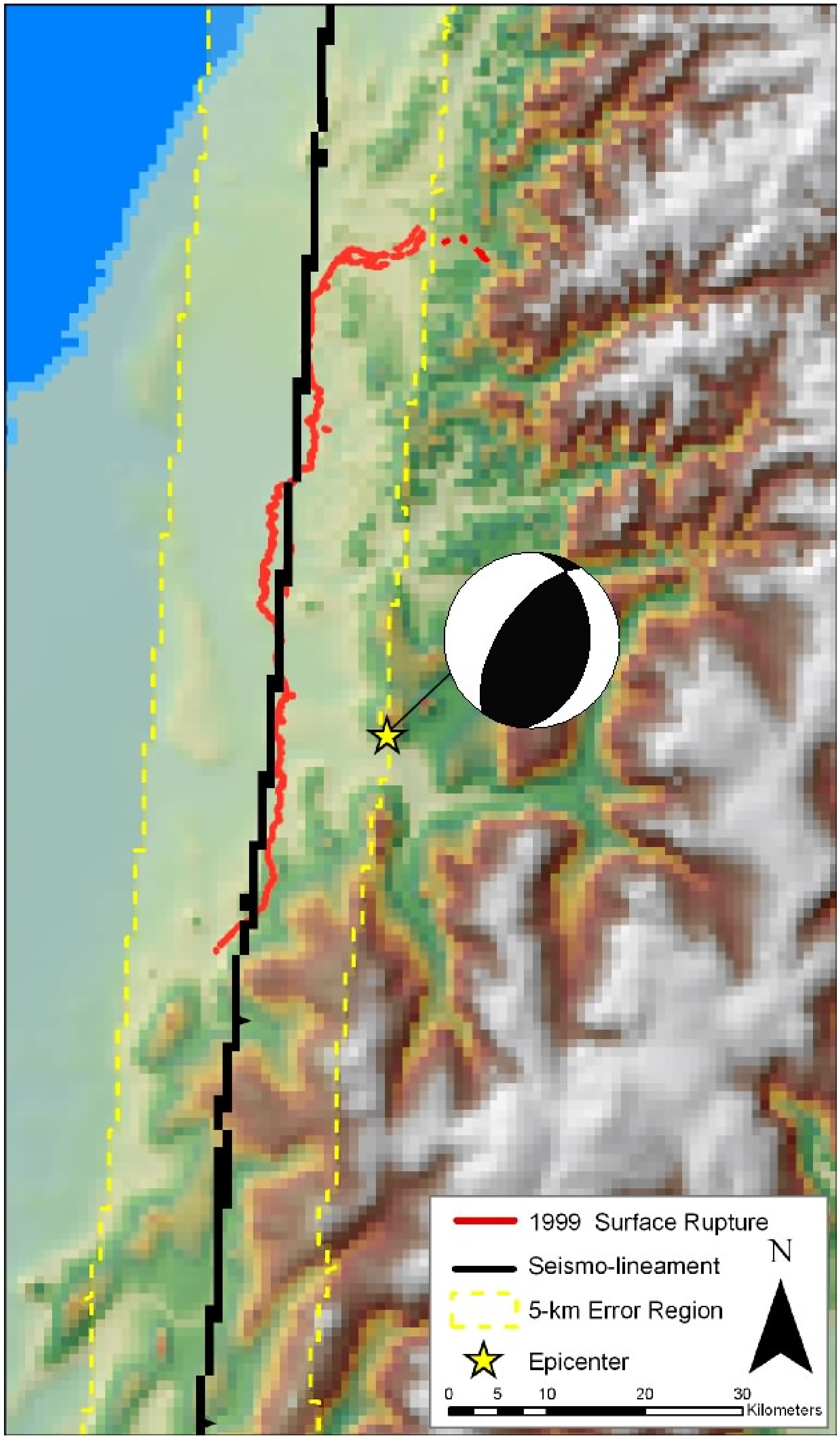

1999, M 7.3 Chi Chi, Taiwan Earthquake. Surface traces from Chen and others (2001). Source parameters for the main event and aftershocks by Chang (2000; 2007).

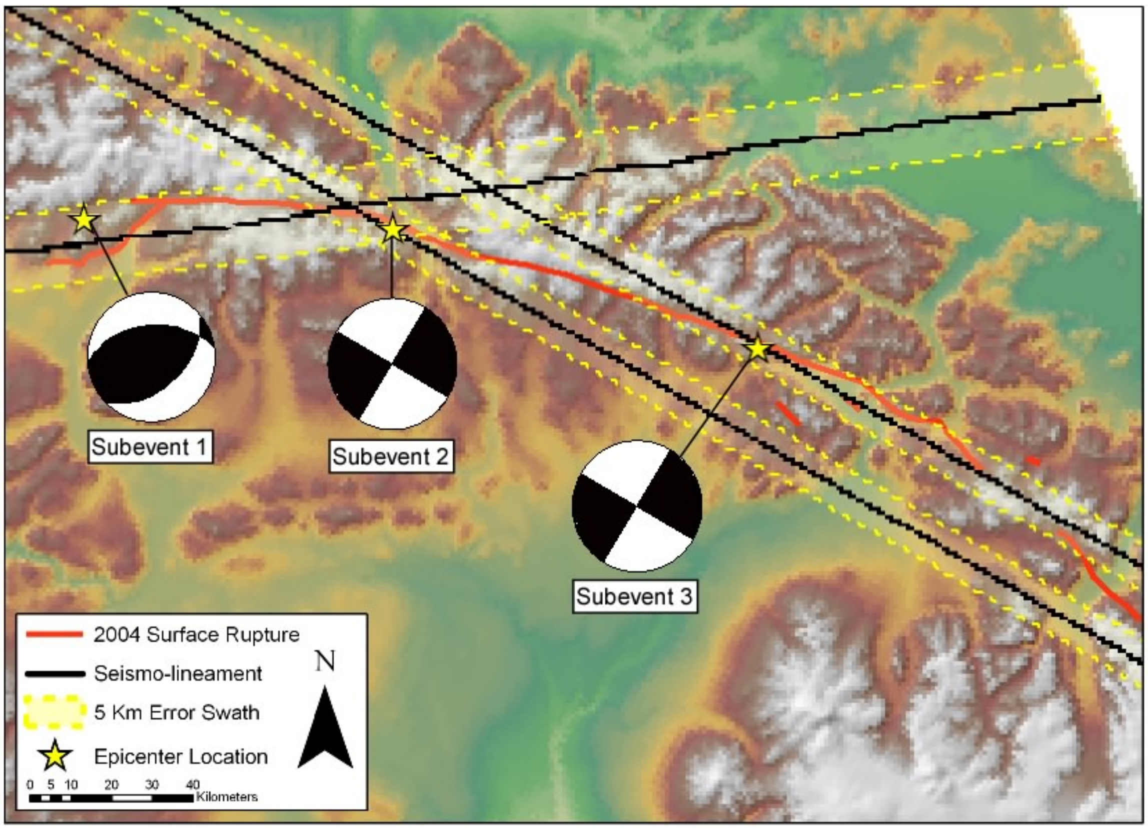

2002, M 7.9 Denali, AK Earthquake. Surface traces mapped by Crone and others (2004), Eberhart-Phillips and others (2003), and Haeussler and others (2004). Source parameters from Eberhart-Phillips and others (2003).

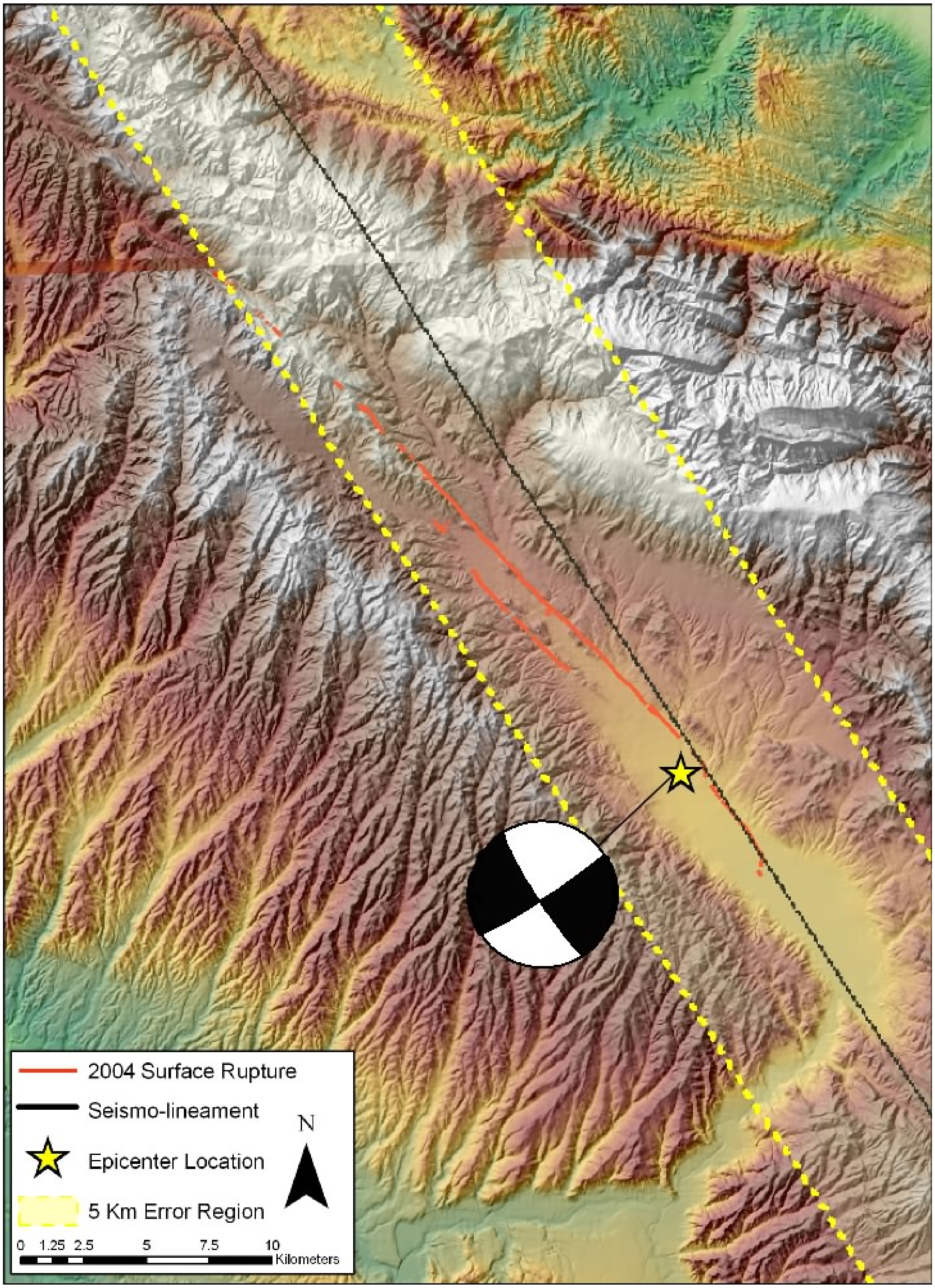

2004, M 6.0 Parkfield, CA Earthquake. Surface traces mapped by Rymer and others (2006). Source parameters the NEIC online catalog.

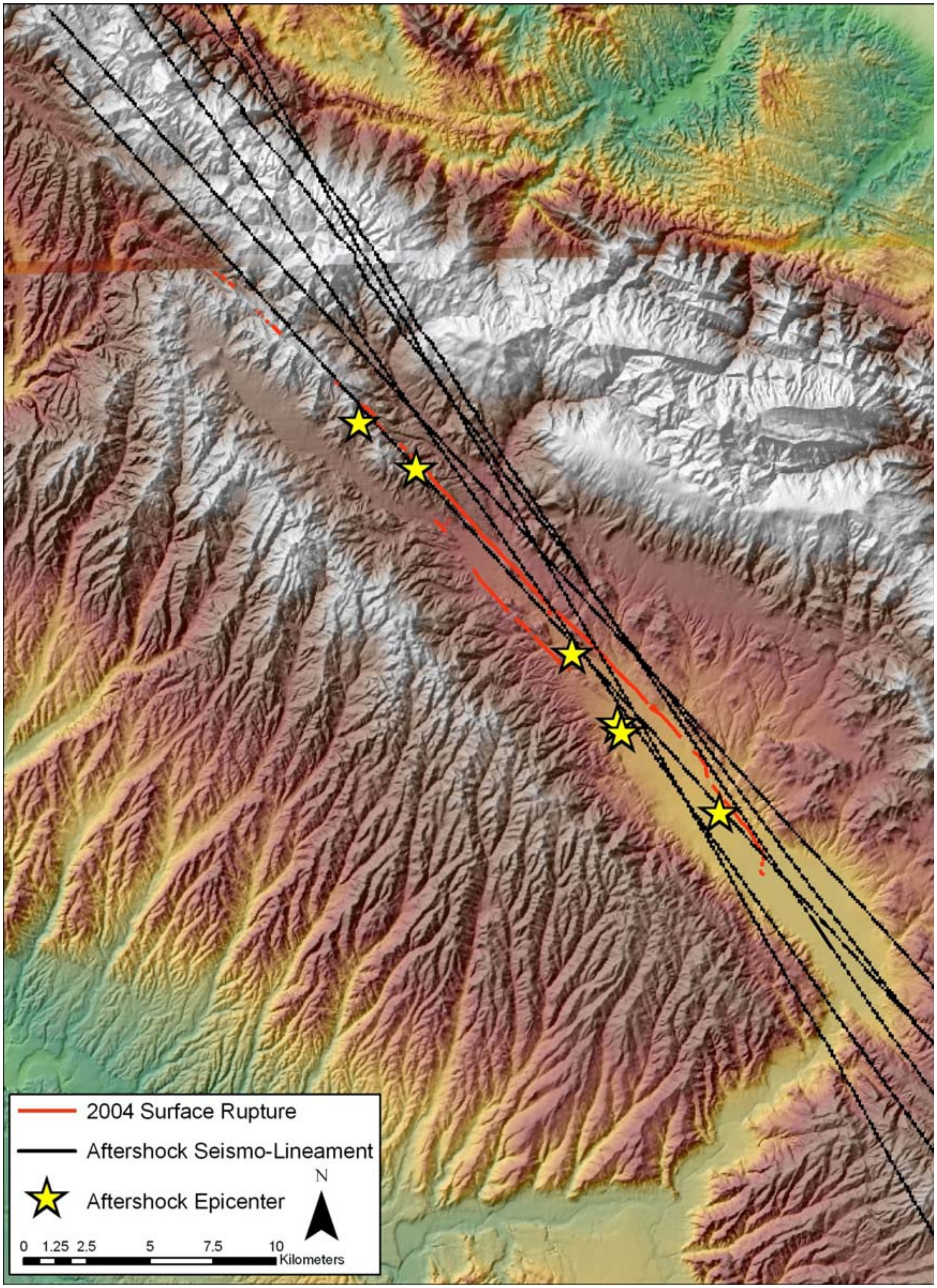

Aftershocks of the 2004, M 6.0 Parkfield, CA Earthquake. Surface traces mapped by Rymer and others (2006). Source parameters from the NEIC online catalog.

REFERENCES

Akman, A. U., Tufekci, K., 2004, Determination and characterization of fault systems and geomorphological features by RS and GIS techniques in the wsw part of Turkey: International Archives of Photogrammetry Remote Sensing and Spatial Information Sciences, v. 35, p. 899-904.

Barrientos, S.E., Ward, S.N., Gonzalez-Ruiz, J.R., and Stein, R.S., 1985, Inversion for moment as a function of depth from geodetic observations and long period body waves of the 1983 Borah Peak Idaho, earthquake *in* Stein, R.S., and Bucknam, R.C., editors., Proceedings of workshop XXVIII on the Borah Peak, Idaho, earthquake: U.S. Geological Survey Open File Report 85-290, p. 485-518.

Bayliss, B., 2006, Test of a method for recognizing previously unmapped seismogenic faults, Baylor University, masters thesis, 115 p.

Bayliss, B., and Cronin, V.S., 2005, Test of a method for recognizing previously unmapped seismogenic faults: Geological Society of America, Abstracts with Programs, v. 37, no. 7, p. 559.

Beaver, D.E., Eliason, J.R., and Thiessen, R.L., 1987, Regional digital major crustal structures in Washington State: *in* Mason, R., editor, Basement Tectonics: Proceedings of the Seventh International Conference, p. 329-340.

Blake, G.H., 1991, Review of Neogene biostratigraphy and stratigraphy of the Los Angeles Basin and implications for basin evolution, *in* Biddle, K.T., editor, Active margin basins: American Association of Petroleum Geologists, Memoir 52, p. 135-184.

Burbank, D.W., and Anderson, R.S., 2001, Tectonic geomorphology: Oxford, Blackwell Science, 274 p.

Campbell, R.H., 1990, Geology and tectonic evolution of the western Transverse Ranges: unpublished report for California Coastal Commission workshop on seismic activity of the Malibu Coast Fault Zone, May 9, 1990, 6 p.

Campbell, R.H., Yerkes, R.F., and Wentworth, C.M., 1966, Detachment faults in the central Santa Monica Mountains, California, *in* Geological Survey Research, 1966: U.S. Geological Survey Professional Paper 550-C, p. C1-C11.

Chang, C. H., 2000, Relocated Chi-Chi, Taiwan earthquake and its characteristics, EOS, Transactions of the American Geophysical Union , v. 81, no. 22, 104.

Chang, C. H., Wu, Y.M., Zhao, L., and Wu, F.T., 2007, Aftershocks of the 1999 Chi-Chi, Taiwan, earthquake: The first hour: Seismological Society of America Bulletin. (In review).

Chen, W.S., Huang, B.S., Chen, Y.G., Lee, Y.H., Yang, C.N., Lo, C.H., Chang. H.C., Sung, Q.C., Huang, N.W., Lin, C.C., Sung, S.H, and Lee K.J., 2001, 1999 Chi-Chi earthquake: A case study on the role of thrust-ramp structures for generating earthquakes: Seismological Society of America Bulletin, v. 91, no. 5, p. 986-994.

Crone, A.J., Machette, M.N., Bonilla, M.G., Lienkaemper, J.J., Pierce, K.L., Scott, W.E., and Bucknam, R.C., 1985, Characteristics of surface faulting accompanying the Borah Peak earthquake, central Idaho, *in* Stein, R.S., and Bucknam, R.C., editors., Proceedings of workshop XXVIII on the Borah Peak, Idaho, earthquake: U.S. Geological Survey Open File Report 85-290, p. 43–58.

Crone, A.J., Personious, S.F., Craw, P.A., Haeussler, P.J., and Staft L.A., 2004, The Susitna Glacier thrust fault—characteristics of surface ruptures on the fault that initiated the 2002 Denali fault earthquake: Seismological Society of America Bulletin, v. 94, no. 6B, p. S5–S22.

Cronin, V.S., 2004, Projecting a fault plane from a focal mechanism solution onto a digital elevation model surface: unpublished *Mathematica* code.

——— 2006, Lineament analysis: unpublished draft manuscript.

——— 2007, Finding the mean and 95% confidence interval of a set of strike-and-dip or lineation data: Environmental and Engineering Geoscience*, in press*.

Cronin, V.S., Byars, B.W., and Gammill, T., 2003, Developing techniques for regional structural interpretation using GIS and DEM-based terrain analysis: Geological Society of America, Abstracts with Programs, v. 34, no. 7, p. 261.

Cronin, V.S., Schurter, G., and Sverdrup, K.A., 1993, Preliminary Landsat lineament analysis of the northern Nanga Parbat–Haramosh Massif, northwest Himalaya: Geological Society of London Special Publication, No. 74, p. 193-206.

Cronin, V.S., and Sverdrup, K.A., 1998, Preliminary assessment of the seismicity of the Malibu Coast Fault Zone, southern California, and related issues of philosophy and practice, in Welby, C.W., and Gowan, M.E., editors, A Paradox of Power--Voices of Warning and Reason in the Geosciences: Geological Society of America, Reviews in Engineering Geology, v. XII, p. 123-155.

Crook, R., Jr., and Proctor, R.J., 1992, The Santa Monica and Hollywood faults and the southern boundary of the Transverse Ranges Province, *in* Pipkin, B., and Proctor, R., eds. Engineering Geology Practice in Southern California: Southern California Section, Association of Engineering Geologists, Special Publication 4, p. 233-246.

Dartnell, P., Gardner, J. V., Mayer, L. A.. Hughes, C., and John, E., 2004, Los Angeles and San Diego Margin High-Resolution Multibeam Bathymetry and Backscatter Data: USGS Open-File Report 2004-1221.

Dibblee, T.W., Jr., 1992, Geologic map of the Topanga and Canoga Park (south 1/2) Quadrangles, Los Angeles County, California: Dibblee Geological Foundation Map DF-35, scale 1:24,000.

Dolan, J. F., and Sieh, K., 1992, Tectonic geomorphology of the northern Los Angeles basin: seismic hazards and kinematics of the young fault movement in Ehlig, P. L., and Steiner, E. A., compilers, Engineering geology field trips – Orange County – Santa Monica Mountains – Malibu: Association of Engineering Geologists, Southern California Section, Guidebook and Volume prepared for the 35th Annual Meeting, October 2-9, 199, p. B20-B26.

Dolan, J.F., Sieh, K., Rockwell, T.K., Yeats, R.S., Shaw, J., Suppe, J., Huftile, G.J., and Gath, E.M., 1995, Prospects for larger or more frequent earthquakes in the Los Angeles metropolitan region: Science, v. 267, p. 199-205.

Doser, D.I., and Smith R.B., 1985, Source parameters of the 28 October 1983 Borah Peak, Idaho earthquake from body wave analysis: Seismological Society of America Bulletin, v. 75, no. 4, p. 1041-1051.

Durham, D. L., and Yerkes, R. F., 1964, Geology and oil resources of the eastern Puente Hills area, southern California: USGS Professional Paper 420-B, 62 p.

Eberhart-Phillips, D., Haeussler, P.J., Freymueller, J.T., Frankel, A.D., Rubin, C.M., Craw, P., Ratchkovski, N.A., Anderson, G., Carver, G.A., Crone, A.J., Dawson, T.E., Fletcher, H., Hansen, R., Harp, E.L., Harris, R.A., Hill, D.P., Hreinsdo´ttir, S., Jibson, R.W., Jones, L.M., Kayen, R., Keefer, D.K., Larsen, C.F., Moran, S.C., Personius, S.F., Plafker, G., Sherrod, B., Sieh, K., Sitar, N., and Wallace W.K., 2003, The 2002 Denali fault earthquake, Alaska—A large magnitude, slip partitioned event: Science, v. 300, no. 5622, p. 1113–1118.

Fisher, M. A., Langenheim, V. E., Sorlein, C. C., Dartnell, P., Sliter, R. W., Cochrane, G. R., and Wong, F. L., 2005, Recent deformation along the offshore Malibu Coast, Dume, and related faults west of Point Dume, southern California: Bulletin of the Seismological Society of America, vol. 95, no. 6, p. 2486-2500.

Fuis, G.S., and 14 others, 2003, Fault systems of the 1971 San Fernando and 1994 Northridge earthquakes, southern California - relocated aftershocks and seismic images from LARSE II: Geology, v. 31, no. 2, p.171-174.

Gammill, T., Cronin, V.S., and Byars, B.W., 2004, Combining earthquake focal data and digital map analysis in reconnaissance for active faults, central Santa Monica

Mountains and northern Santa Monica Bay, California: Geological Society of America, Abstracts with Programs, v. 36, no. 5,, p. 298.

Greene, H.G., and Kennedy, M.P., editors, 1986, Geology of the mid-southern California continental margin: California Department of Conservation, Division of Mines and Geology, California Continental Margin Geologic Map Series, Area 2, 4 sheets, scale 1:250,000.

Hart, E. W., 1994, Fault-rupture hazard zones in California: California Department of Conservation, Division of Mines and Geology, Special Publication 42, Revised 1994, 34 p.

Hardebeck, J.L., 2005, SCEDC web dataset: Southern California Earthquake Data Center, http://www.data.scec.org/research/socal_focal_JLH.html.

Haeussler, P.J., Schwartz, D.P., Dawson, T.E., Stenner, H.D., Lienkaemper, J.J. Sherrod, B., Cinti, F.R., Montone, P., Craw, P., Crone, A.J., and Personius, S., 2004, Surface rupture and slip distribution of the Denali and Totschunda faults in the 3 November 2002 M 7.9 earthquake, Alaska: Seismological Society of America Bulletin, v. 94, no. 6B, p. S23–S52.

Haugerud, R.A., Harding, D.J., Johnson, S.Y., Harless, J.L., Weaver, C.S., and Sherrod, B.L., 2003, High-resolution LIDAR topography of the Puget lowland, Washington – a bonanza for Earth science: GSA Today, v. 13, no. 6, p. 4-10, ftp://rock.geosociety.org/pubs/GSAToday/gt0306.pdf

Hauksson, E., 1990, Earthquakes, faulting and stress in the Los Angeles Basin: Journal of Geophysical Research, v. 95, p. 15365-15391.

———2004, 3-D earthquake focal mechanisms: Southern California Earthquake Data Center, http://www.data.scec.org/research/socal_focal.html

Hauksson, E., Jones, L.M. and Hutton K., 2002, The 1999 Mw 7.1 Hector Mine, California earthquake sequence: complex conjugate strike-slip faulting: Seismological Society of America Bulletin v. 92, no. 4, p. 1154–1170.

Hill, R.L., 1979, Potrero Canyon fault and University High School escarpment, *in* Field guide to selected engineering geologic features, Santa Monica Mountains, Association of Engineering Geologists, Southern California Section, Guidebook to May 19, 1979, field trip: Los Angeles, Calif., p. 83-103.

Hobbs, W.H., 1904, Lineaments of the Atlantic border region: Geological Society of America Bulletin, v. 15, p. 483-506.

Hoots, H.W., 1931, Geology of the eastern part of the Santa Monica Mountains, Los Angeles County, California: U.S. Geological Survey Professional Paper 165, p. 83-134, map scale 1:24,000.

Hornafius, J.S., Luyendyk, B.P., Terres, R.R., and Kamerling, M.J., 1986, Timing and extent of Neogene tectonic rotation in the western Transverse Ranges, California: Geological Society of America Bulletin, v. 97, no. 12, p. 1476-1487.

Johnson, H.R., 1932, Folio of plates to accompany geologic report, Quelinda Estate: Unpublished report.

Jordan, G., and Schott, B., 2004, Application of wavelet analysis to the study of spatial pattern of morphotectonic lineaments in digital terrain models: A case study: Remote Sensing of Environment, vol. 94, p. 31-38.

Jordan, G., Jeijninger, B.M.L., van Hinsbergen, D.J.J., Meulenkamp, J.E., and van Dijk, P.M., 2005, Extraction of morphotectonic features from DEMs: Development and applications for study areas in Hungary and NW Greece: International Journal of Applied Earth Observation and Geoinformation, vol. 7, p. 163-182.

Junger, A., and Wagner, H.C., 1977, Geology of the Santa Monica and San Pedro basins, California continental borderland: U.S. Geological Survey Map, MF-820, 1:250,000.

Kamerling, M. J., and Luyendyk, B. P., 1979, A model for Neogene tectonics of the inner southern California borderland constrained by paleomagnetic data: Geological Society of America Abstracts with Programs, vol. 11, no. 7, p. 453.

Keaton, J., 1979, Field guide to selected engineering geologic features, Santa Monica Mountains: Association of Engineering Geologists, Southern California Section Annual Field Trip, May 19, 1979.

Kew, W.S.W., 1927, Geologic sketch of Santa Rosa Island, Santa Barbara County, California: Geological Society of America Bulletin, v. 38, p. 645-653.

Lajoie, K.R., Kern, J.P., Wehmiller, J.F., Kennedy, G.L., Mathieson, S.A., Sarna-Wojcicki, A.M., Yerkes, R.F., and McCrory, P.F., 1979, Quaternary marine shorelines and crustal deformation, San Diego to Santa Barbara, California, in Abbott, P.L., ed., Geological excursions in the southern California area. Guidebook for field trips, Geological Society of America Annual Meeting, Nov. 1979: Department of Geological Sciences, San Diego State University, San Diego, Calif., p. 3-15.

Lee, W.H.K., Yerkes, R.F., and Simirenko, M., 1979, Recent earthquake activity and focal mechanisms in the western Transverse Ranges, California: U.S. Geological Survey Circular 799-A, 26 p.

Legg, M.R., Kamerling, M.J., and Francis, R.D., 2004, Termination of strike-slip faults at convergence zones within continental transform boundaries -- examples from the California Continental Borderland, in Grocott, J., McCaffrey, K.J.W., Taylor, G., and Tikoff, B., editors, Vertical coupling and decoupling in the lithosphere: Geological Society, London, Special Publication 227, p. 65-82.

Lidmar-Bergström K., Elvhage C., and Ringberg B., 1991, Landforms in Skane, south Sweden: Geografiska Annaler, v. 73A, p. 61–91.

Lillesand, T.M., and Kiefer, R.W., 1987, Remote sensing and image interpretation [2nd edition]: New York, John Wiley & Co., 721 p.

Luyendyk, B.P., 1991, A model for Neogene crustal rotations, transtension and transpression in California: Geological Society of America Bulletin, v.103, p. 1528-1536.

Luyendyk, B.P., Kamerling, M.J, and Terres, R.R., Hornafius, S.J., 1985, Simple shear of southern California during Neogene time suggested by paleomagnetic declinations: Journal of Geophysical Research, v. 90, p. 12454-12466.

Madani, A., 2001, Selection of the optimum Landsat Thematic Mapper bands for automatic lineaments extraction, Wadi Natash area, South Eastern Desert, Egypt: 22nd Asian Conference on Remote Sensing, 5-9 November, 2001.

McCalpin, J., editor, Paleoseismology: San Diego, California, Academic Press, 588 p.

McGill, J.T., 1981, Recent movement on the Potrero Canyon fault, Pacific Palisades area, Los Angeles, in Geological Survey research 1980: U.S. Geological Survey Professional Paper 1175, p. 258-259.

McGill, J.T., 1982, Preliminary geologic map of the Pacific Palisades area, City of Los Angeles, California: U.S. Geological Survey, Open-File Report 82-194, scale 1:4,800, 15 p.

McGill, J.T., 1989, Geologic maps of the Pacific Palisades area, Los Angeles, California: U.S. Geological Survey Map I-1828, 2 sheets, scale 1:4,800.

McGill, J. T., 1980, Recent movement on the Potrero Canyon fault, Pacific Palisades area, Los Angeles, *in* Geological Survey research, 1980L USGS Professional Paper 1175, p. 258-259.

McGill, J.T., Lamar, D.L., Hill, R.L., and Michael, E.D., 1987, Potrero Canyon fault, landslides and oil drilling site, Pacific Palisades, Los Angeles, California: Geological Society of America, Centennial Field Guide Volume 1, p. 213-216.

McMahon, M.J., and North, C.P., 1993. Three-dimensional integration of remotely sensed geological data: A methodology for petroleum exploration: *in* Exploration, environment and engineering: *Proceedings of the Ninth Thematic Conference on Geologic Remote Sensing.* v. 1, p. 221-233.

Miller, V.C., 1961, Photogeology: New York, McGraw-Hill Book Company, 248 p.

Moran, Proctor, Mueser, and Rutledge, 1959, Final report, Pacific Palisades landslide study: California Department of Public Works.

Nabelek, J.,H.Eyidogan, and Toksoz, M.N., 1985, Source parameters of the Borah Peak, Idaho earthquake of October 1983 from body-wave inversion: EOS, Transactions of the American Geophysical Union, v. 66, p. 308.

Onorati G., Poscolieri M., Ventura R., Chiarini V., and Crucilla U., 1992, The digital elevation model of Italy for geomorphology and structural geology: Catena v. 19, p. 147–178.

Ray, R.G., 1960, Aerial photographs in geologic interpretation and mapping: U.S. Geological Survey, Professional Paper 373, 230 p.

Richins, W. D., Smith, R.B., Langer, C.J., Zollweg, J.E., King, J.J., and Pechmann, J.C., 1985, The 1983 Borah Peak, Idaho earthquake – Relationship of aftershocks to the main shock, surface faulting, and regional tectonics, *in* Stein, R.S., and Bucknam, R.C., editors., Proceedings of workshop XXVIII on the Borah Peak, Idaho, earthquake: U.S. Geological Survey Open File Report 85-290, v. A., p. 285-310

Rymer, M.J., Tinsley, J.C., Treiman, J.A., Arrowsmith, J.R., Clahan, K.B., Rosinski, A.M., Bryant, W.A., Snyder, H.A., Fuis, G.S., Toke', N., and Bawden G.W., 2006, Surface fault slip associated with the 2004 Parkfield, California, earthquake: Seismological Society of America Bulletin, v. 96, no. 4B, p. S11–S27.

Sharp, R.V., Budding, K.E., Boatwright, J. Ader, M.J., Bonilla, M.G., Clark, M.M., Fumal, T.E., Harms, K.K., Lienkaemper, J.J., Morton, D.M., O'Neill, B.J., Ostergren, C.L., Ponti D.J., Rymer, M.J., Saxton, J.L., and Sims, J.D., 1989, Surface faulting along the Superstition Hills fault zone and nearby faults associated with the earthquakes of 24 November 1987: Seismological Society of American Bulletin, v. 79, no. 2, p. 254-281.

Stein, R.S. and Barrientos S.E., 1985, Planar high-angle faulting in the Basin and Range: geodetic analysis of the 1983 Borah Peak, Idaho, earthquake: Journal of Geophysical Research v. 90, no. B13, p. 11355-11366.

Schoellhamer, J. E., Woodford, A. O., Vedder, J. G., Yerkes, R. F., and Kinney, D. M., 1981, Geology of the northern Santa Ana Mountains, California:USGS Professional Paper, 420-D, 109 p.

Siedman, L.E., and Cronin, V.S., 2006, Analysis of seismo-lineaments, DEMs, and fieldwork leads to different ideas about active deformation in the Santa Monica Mountains, southern California: Geological Society of America Abstracts with Programs, v. 38, No. 7, p. 309

Slosson, J.A., and Dill, R. F., 1994, Offshore geology indicates the unstable, landslide prone areas north of Santa Monica are long term events not entirely attributable to the acts of man: unpublished article.

Smith, M.J., and Clark, J.D., 2005, Methods for the visualization of digital elevation models for landform mapping: Earth Surface Processes and Landforms v. 30, p. 885–900.

Snyder, J.P., 1982, Map projections used by the U.S. Geological Survey: U.S. Geological Survey Bulletin 1532, 313 p.

Treiman, J.A., 1994, Malibu Coast Fault, Los Angeles County, California: California Department of Conservation, Division of Mines and Geology, Fault Evaluation Report FER-229, 33 p.

Treiman, J.A., compiler, 2000, Fault number 99, Malibu Coast fault, *in* Quaternary fault and fold database of the United States, ver 1.0: U.S. Geological Survey Open-File Report 03-417, http://qfaults.cr.usgs.gov.

Treiman, J.A., Kendrick, K.J, Bryant, W.A, Rockwell, T.K, and McGill S.F., 2002, Primary surface rupture associated with the Mw 7.1 16 October 1999 Hector Mine earthquake, San Bernardino County, California: Seismological Society of American Bulletin, v. 92, no. 4, p. 1171–1191.

Tsutsumi**,** H., Yeats, R.S., and Huftile, G.J., 2001, Late Cenozoic tectonics of the northern Los Angeles fault system, California: Geological Society of America Bulletin, v. 113, no. 4, p. 454–468.

Ward, S.N., and Barrientos, S.E., 1986, An inversion for slip distribution and fault shape from geodetic observations of the 1983, Borah Peak, Idaho, earthquake: Journal of Geophysical Research, v. 91, no. B5, p. 4909-4919.

Wesson, R.L., Helley, E.J., Lajoie, K.R., and Wentworth, C.M., 1975, Faults and future earthquakes, *in* Borcherdt, R.D., editor, Studies for seismic zonation of the San Francisco Bay region: U.S. Geological Survey Professional Paper 941-A, p. 5-30.

Wise D.U., Funiciello R., Parotto M., and Salvini F., 1985, Topographic lineament swarms: clues to their origin from domain analysis of Italy: Geological Society of America Bulletin, v. 96, p. 952–967.

Won-In, K., and Charusiri, P., 2003, Enhancement of thematic mapper satellite images for geological mapping of the Cho Dien area, Northern Vietnam: International Journal of Applied Earth Observation and Geoinformation, v. 4, p. 183-193.

Woodring, W. P., Bramlette, M. N. and Kew, W. S. W., 1946, Geology and Paleontology of Palos Verdes Hills, California: USGS Professional Paper 207, 145 p.

Wright, T.L., 1991, Structural geology and tectonic evolution of the Los Angeles Basin, California, in Biddle, K.T., ed., Active Margin Basins: American Association of Petroleum Geologists Memoir 52, p. 35-134.

Yeats, R.S., 1968, Rifting and rafting in the southern California borderland, in Dickinson, W.R., and Grantz, A., eds., Proceedings of the conference on tectonic problems of the San Andreas fault system: Palo Alto, California, Stanford University Publications, Geological Sciences, v. XI, p. 307-322.

Yerkes, R. F., 1972, Geology and oil resources of the western Puente Hills area, southern California: USGS Professional Paper 420-C, 63 p.

Yerkes, R.F., and Campbell, R.H., 1980, Geologic map of east central Santa Monica Mountains, Los Angeles County, California: U.S. Geological Survey Miscellaneous Investigations Series, Map I-1146, map scale 1:24,000.

Yerkes, R.F., and Lee, W.H.K., 1979, Faults, fault activity, epicenters, focal depths, and focal mechanisms, 1970-75 earthquakes, western Transverse Ranges, California: U.S. Geological Survey Miscellaneous Field Studies Map MF-1032, 2 sheets, scale 1:250,000.

Yerkes, R.F., and Wentworth, C.M., 1965, Structure, Quaternary history, and general geology of the Corral Canyon area, Los Angeles County, California: U.S. Geological Survey Open-File Report 864, 214 p.

Yerkes, R.F., Campbell, R.H., Blackerby, B.A., Wentworth, C.M., Birleland, P.W., and Schoellhamer, J.E., 1971, Preliminary geologic map of the Malibu Beach quadrangle, Los Angeles County, California: U.S. Geological Survey Open-File Map, scale 1:12,000.